

POLITECNICO DI TORINO

Master's Degree in Energy and nuclear engineering



Master's Degree Thesis

Fuel and LBE source term calculations for MYRRHA

Supervisors

Prof. Sandra DULLA

Dr. Luca FIORITO

Dr. Matteo ZANETTI

Candidate

Federico DI CROCE

October 2023

Summary

In the framework of the pre-licensing phase of MYRRHA, the source term assessment is carried out for the MOX fuel and LBE coolant to provide safety-relevant pieces of information.

The buildup of activation and spallation products in the LBE during operation and after shutdown of the reactor is estimated. The attention is focused the sub-critical configuration, in which higher particle fluxes are expected with enhanced production of safety concerning radionuclides.

In the spallation target assembly, where the linear accelerator is located, the worst conditions are expected and the focus is given to the estimation of nuclide inventory in this region. Among safety concerning volatile nuclides ^3H , ^{195}Hg , ^{197}Hg and ^{210}Po convey the largest dose. The latter is also the main contributor to decay heat in the first decay period after shutdown. Most of the nuclides analysed are mainly generated by spallation reactions, whose relevance reduces moving further from the spallation target.

The source term in the fuel is assessed from the nuclide inventory in every fuel assembly present in the core after one irradiation cycle starting from the equilibrium condition. The buildup of volatile nuclides as function of burnup is estimated, showing that the peak concentration of short lived nuclides is reached when the FA is irradiated in the central position, while the long lived fission products reach the maximum concentration when the fuel assembly has the highest burnup and has been reshuffled in all core positions.

From the nuclide inventory, envelope activity and decay heat curves are drawn for a period of 70 y of decay. Comparison of critical and sub-critical configuration is presented for all the observables.

Power levels in the fuel assemblies of the equilibrium core provide the normalization condition for a fuel assembly depletion model. The FA model is built in Serpent2, it mimics the fuel assembly reshuffling in the core and it is suitable for uncertainty analysis. Input parameter such as nuclear data (cross sections

and neutron fission products yields) are perturbed to estimate the impact on the observables of the analysis: volatile fission products, actinides relevant for spent nuclear fuel and decay heat.

Cross sections uncertainties have an impact of plutonium and minor actinides. The only volatile with relevant statistical variation is ^{134}Cs . In contrast, the perturbation of fission yields directly impacts the degree of final uncertainty computed for fission products. The uncertainty on integral parameters, such as decay heat, is determined by the concentration uncertainty of the nuclides contributing to the decay heat rate as function of decay time.

Acknowledgements

I am deeply grateful to my promoter, Prof. Sandra Dulla, for her support and guidance in my master's program. Her contribution, in the form of comments and feedback was precious to the realization of this thesis.

I am grateful to SCK CEN for giving me the opportunity to conduct my research and for all of the resources and support they provided. I would like to especially thank my mentor, Dr. Ing. Luca Fiorito, who gave me the chance to work on this topic under his guidance and he helped me in any stage of the project with his understanding of the physical phenomena and his expertise with the tools employed. I would also like to thank Dr. Ing. Matteo Zanetti for being my co-mentor and providing valuable feedback and suggestions. Their insights and guidance were instrumental in helping me to shape my research and write this thesis.

I am deeply thankful to my friends and family for their love and support during this process. Without their encouragement and motivation, I would not have been able to complete this journey. In particular, I would like to thank the friends that shared with me five years of adventures in Turin and who helped me to overcome the difficult moments. Similarly, I would also like to thank the colleagues and primarily the friends met during my staying in Belgium, for their collaboration during my research and especially for the environment we created together.

Finally, I would like to extend my sincere gratitude to all of the participants in my study. Their willingness to share their experiences and insights has been invaluable to my research and has helped to make this thesis a success. Thank you for your time and contribution. I am grateful to everyone who has supported me throughout this process. Without your help and guidance, this thesis would not have been possible.

Table of Contents

List of Tables	IX
List of Figures	X
Acronyms	XV
1 Introduction	1
1.1 MYRRHA project	2
1.2 Source term assessment	3
1.2.1 Reference accidental conditions and related observables	4
2 Theoretical background	6
2.1 Particle-matter interaction	6
2.1.1 Spallation reactions	6
2.1.2 Neutron-matter interaction	7
2.2 Transport and depletion	8
2.2.1 Particle transport	8
2.2.2 Depletion equations	9
2.2.3 Coupling transport and depletion	10
2.2.4 Derived quantities	10
2.3 Uncertainty quantification	11
2.3.1 Sources of uncertainty	11
2.3.2 Uncertainty propagation and statistical sampling	12
2.4 Codes and data employed	14
2.4.1 Monte Carlo codes for particle transport	14
2.4.2 ALEPH2	15
2.4.3 SANDY	16
2.4.4 NJOY	17
2.4.5 Nuclear data libraries	17

3	MYRRHA reference model	19
3.1	MYRRHA reference model description	19
3.2	Equilibrium cycle definition	22
3.2.1	Initial conditions	22
3.2.2	Equilibrium core modeling	22
3.2.3	Convergence analysis	23
4	LBE depletion model	24
4.1	Modeling assumption	24
4.2	Spallation target assembly sub-division	26
4.3	ALEPH2 update verification	29
5	LBE source term - Spallation target assembly	31
5.1	LBE inventory in the STA	31
5.2	LBE activity in the STA	33
5.3	Decay Heat associated to LBE in the STA	34
5.4	Production mechanisms of relevant nuclides in the STA	34
5.5	LBE activity comparison for the MYRRHA Design Revisions 1.4 and 1.8	38
5.6	Comparison of neutron data libraries	39
6	Fuel source term - Equilibrium core model	42
6.1	Nuclide concentrations	43
6.2	Activity of an irradiated MYRRHA FA	46
6.3	Decay heat of an irradiated MYRRHA FA	49
6.4	Production mechanisms for the nuclides relevant for the source term of the MYRRHA FA	52
7	Model simplification - From a 3D core model to a 2D fuel assembly model	56
7.1	Fuel assembly models description	57
7.2	Fuel assembly model assumptions	59
7.3	Fuel assembly model limitations	60
7.3.1	Spectral differences between core and fuel assembly simulations	60
7.3.2	Power profile discrepancies	61
7.4	Fuel assembly model output	64
7.4.1	2D fuel assembly model output	64
7.4.2	3D fuel assembly models output	66
7.5	Comparison of fuel assembly model with respect to equilibrium core output	68
7.5.1	2D fuel assembly model	68
7.5.2	3D fuel assembly model	69

8	Nuclear data uncertainty	71
8.1	Uncertainty on nuclide vector	71
8.1.1	Cross sections uncertainty propagation	71
8.1.2	Nuclear fission product yields uncertainty propagation . . .	77
8.2	Uncertainty on decay heat	79
9	Conclusions	83
A	Tritium production in the fuel	86
B	Nuclear data uncertainty	88
B.1	Cross sections	88
B.2	Neutron fission product yields	89
B.3	Convergence analysis	89
	Bibliography	93

List of Tables

3.1	Core configuration summary	21
5.1	LBE spallation and activation products concentrations in the STA at the end of life (EoL) after 40 of operation.	32
5.2	Reaction rates of ^{209}Bi (n, γ) reaction in the spallation target assembly.	36
5.3	Major differences in the models employed to evaluate the MYRRHA source term. Discrepancies come from design differences and modelling assumptions. Volumes and neutron fluxes are given for the spallation target assembly.	38
5.4	Activity concentrations of relevant nuclides in the LBE in the spallation target assembly obtained in the past work for the MYRRHA Design Revision 1.4 and in this work for the MYRRHA Design Revision 1.8.	39
6.1	EoI concentration (FA with largest burnup) ratio between sub-critical end critical mode for selected actinides.	44
7.1	Serpent simulation parameters	59
7.2	Reaction rates of fission and neutron capture respectively in ^{239}Pu and ^{240}Pu	61
7.3	k_{inf} in the homogeneous 3D fuel assembly model (without depletion zones) as function of burnup.	66
B.1	Nuclides of which cross sections data are perturbed in JEFF-3.3	91
B.2	Nuclides of which cross sections data are perturbed in ENDF/B-VIII.0	92
B.3	Actinides of which cross section data are perturbed in JENDL-4.0u	92

List of Figures

1.1	MYRRHA reactor glimpse with emphasis to the features analyzed during the work. The picture is taken from [5].	2
2.1	Convergence analysis on the perturbation coefficients of ^{239}Pu fission cross section and ^{245}Cm neutron capture cross section @Energy = 0.1 MeV in top and bottom figure respectively. The perturbation coefficients sample distribution is shown on the right part of the plot for both cross section data.	13
3.1	Schematic cross sectional view of the core in sub-critical (left) and critical configuration (right).	19
3.2	Example of irradiation history in MYRRHA, showing one period made of three irradiation and maintenance cycles.	21
3.3	Convergence analysis of k_{eff} in the critical core model.	23
4.1	Neutron (left) and proton (right) energy-dependent flux in the spallation target at BoC. The neutron flux in the whole spallation target assembly is depicted in blue.	25
4.2	Proton flux distribution in the spallation target assembly. xz view on the left, xy cross section 5 cm below the beam window on the right.	27
4.3	Cumulative proton flux integrated in axial direction.	27
4.4	Variation in nuclide activity in STA due to the modeling assumptions. Impact of zone division is exploited.	28
4.5	Comparison between two ALEPH2 versions of the major contributors activity after 1 irradiation cycle and after 40 years of operation.	29
5.1	Variation of elemental concentrations taking into account or not the separate regions in the STA. The deviations are evaluated at EoI, only the elements with content higher than 10 mg/kg are shown.	33
5.2	Time evolution of the activity of volatile products present in the spallation target assembly during reactor operation and after shutdown.	33

5.3	Time evolution of the decay heat after shut-down. Contribution of each particle on top and nuclides fractions in the bottom figure. . .	35
5.4	Time evolution of the decay heat with/without STA sub-division. The dashed line shows the deviation from the homogeneous case and the corresponding y-scale is on the right.	36
5.5	EoI concentrations of relevant nuclides obtained with different neutron NDL. The outcomes are compared to the reference library: JEFF-3.1.2	40
5.6	^{202}Hg (n, γ) cross section data: absolute values for JEFF-3.1.2 and JEFF-3.3.	41
6.1	Buildup of volatile fission products in sub-critical configuration, divided in two categories depending to their evolution. Normalized on the EoC concentration in critical configuration.	45
6.2	FA activity as a function of discharge burnup and decay time. Critical configuration in the top figure, sub-critical in the bottom.	47
6.3	Evolution of envelope activity in sub-critical configuration.	48
6.4	Fractional evolution of major contributors to the envelope activity. The actinides are drawn with solid line while the fission products with dashed.	48
6.5	Fuel assembly decay heat rate as function of FA burnup and decay time. Critical configuration in the top figure, sub-critical in the bottom.	50
6.6	Evolution of envelope decay heat curve in sub-critical configuration.	50
6.7	Decay heat envelope curve associated to particle emission. The sub-critical configuration is taken into account.	51
6.8	Fractional evolution of major contributors to the envelope decay heat. Actinides are plotted with solid line while fission products with dashed.	51
6.9	Buildup of actinides during irradiation, normalized on the EoI concentration.	55
7.1	Cross sectional view of the MYRRHA fuel assembly	58
7.2	Irradiation history of the FA. The power level is retrieved from the core at equilibrium, taking into account the FA reshuffling the core.	59
7.3	Spectral comparison among core and 2D/3D FA model.	61
7.4	Axial profile of the normalized fission reaction rate. The result of the core model central assembly is compared with the one of FA model. Green and purple curves show the effect of albedo.	62

7.5	Deviation on the EoI nuclide inventory of the 2D FA with partial reflective boundary conditions (albedo=0.959) with respect to perfect reflective boundary conditions.	63
7.6	k_{inf} evolution in 2D fuel assembly with reflective BCs. Statistical uncertainty associated is shown in the zoom.	64
7.7	Neutron spectrum in the fuel assembly at different burnup level . . .	65
7.8	k_{inf} variation with respect to homogeneous 3D FA model introducing axial depletion zones.	67
7.9	Deviation on EoI concentrations evaluated in 3D FA simulations: comparison of axial depletion zones with respect to the homogeneous model.	67
7.10	Comparison of the EoC concentration in a 2D fuel assembly model with full reflective boundaries to the results obtained from a core simulation.	68
7.11	Comparison of the EoC concentration in a 2D fuel assembly model with partial reflective boundary conditions to the results obtained from a core simulation.	69
7.12	Comparison of EoC nuclides concentration in 3D FA model with respect to the results of the 2D fuel assembly model. Bright and dull bars are referred to the model with and without axial depletion respectively.	70
8.1	Actinides concentration uncertainty at EoI coming from cross section uncertainty propagation.	72
8.2	Plutonium isotopes uncertainty evolution as function of the FA burnup.	73
8.3	Fission products concentration uncertainty at EoI coming from cross section uncertainty propagation. Divided in volatiles and decay heat contributors.	75
8.4	Independent fission yields as a function of product mass number for ^{239}Pu in the fast region ($E = 400 \text{ keV}$).	76
8.5	Fission products concentration uncertainty at EoI coming from neutron fission product yields uncertainty propagation. Divided in volatiles and decay heat contributors.	77
8.6	Correlation matrix among nuclides contributing to the uncertainty of ^{134}Cs	78
8.7	Decay heat uncertainty evolution from cross section and fission yield uncertainty propagation. A decay time up to 70 years is considered.	80
8.8	Decay heat uncertainty evolution of a fuel assembly irradiated for 1 and 18 cycles. Brown line shows the correlation between the two cases.	82

A.1	Tritium production in critical/sub-critical configuration. Top: buildup during irradiation normalized to critical discharge concentration. Bottom: tritium production in the first cycle split by major contributors.	87
B.1	Convergence of the mean and standard deviation of the discharge concentration of ^{244}Cm with the number of cross section samples.	90
B.2	Convergence of the mean and standard deviation of the discharge concentration of ^{134}Cs with the number of neutron fission product yields samples.	90

Acronyms

AI

artificial intelligence

MYRRHA

Multi-purpose hYbrid Research Reactor for High-tech Applications

ADS

Accelerator Driven System

linac

Linear Accelerator

SCK CEN

Belgian Nuclear Research Centre

LBE

Lead-Bismuth Eutectic

MOX

Mixed Oxide Uranium fuel

LBECS

Lead Bismuth Eutectic conditioning system

FA

Fuel Assembly

IVFS

In-Vessel Fuel Storage

RF
Radio frequency

ST
Spallation Target

SF
Spallation Fragment

DH
Decay Heat

FP
Fission Products

SNF
Spent Nuclear Fuel

XS
Cross Section

MC
Monte Carlo

RAM
Random Access Memory

CR
Control Rod

SR
Safety Rod

IPS
In-Pile Section

BoL
Beginning of Life

BoC

Beginning of Cycle

EoC

End of Cycle

EoI

End of Irradiation

EoL

End of Life

DBA

Design Basis Accident

STA

Spallation Target Assembly

LWR

Light Water Reactor

BC

Boundary Condition

BU

burnup

PWR

Pressurized Water Reactor

NDL

Nuclear Data Library

NFPY

Neutron Fission Product Yields

IFY

Independent Fission Yields

CFY

Cumulative Fission Yields

GLS

Generalized Least Squares

Chapter 1

Introduction

Electricity accounts for about 20% of the world's total final consumption of energy according to [1] and the demand is increasing up to 150% by 2050. At the end of 2021, the world's total nuclear power capacity was 389.5 gigawatts (electrical) (GW(e)) and it accounts for about 10% of the global electricity production and more than a quarter of the world's low carbon electricity production [2]. The current nuclear reactor fleet is old and replacement is necessary to keep providing the same share of energy production in the near future.

Climate change is one of the driver to maintain and expand the use of nuclear power since it avoids emission of CO_2 in atmosphere which is the main concern regarding to climate change. Most of the technologies to introduce to reach the net zero emission in 2050 are currently under development and it is particularly true for nuclear power reactors: advanced reactors are under investigation with the aim of providing clean energy at an affordable price, focusing on safety aspects and spent fuel management.

In this framework, the R&D on Generation-IV nuclear reactor technologies is particularly important to ensure the highest level of safety and performance. On this respect, liquid metal cooled reactors [3] offer many advantages:

- low pressure operation thanks to the high melting and boiling point;
- better fuel utilization and less high-level waste production thanks to the fast neutron spectra;
- high power density with a low coolant to fuel ratio thanks to more effective coolant than water;
- high coolant density that promotes natural convection cooling and mitigation of thermal transients;

- high retention properties of the coolant for some fission products.

The feasibility of this technology has to be investigated and MYRRHA research reactor will serve the purpose. It will also play a key role in the nuclear waste treatment, that remains the main environmental concern related to nuclear power since the radioactive waste can remain radioactive and dangerous to human health for thousands of years.

1.1 MYRRHA project

MYRRHA is the Multi-purpose hYbrid Research Reactor for High-tech Applications being developed at SCK CEN since 2004 [4]. It is the world's first large scale Accelerator Driven System (ADS) that consists of a sub-critical nuclear reactor driven by a high power linear accelerator. The proposed cut view of the reactor vessel is shown in Fig. 1.1; the picture is taken from [5].

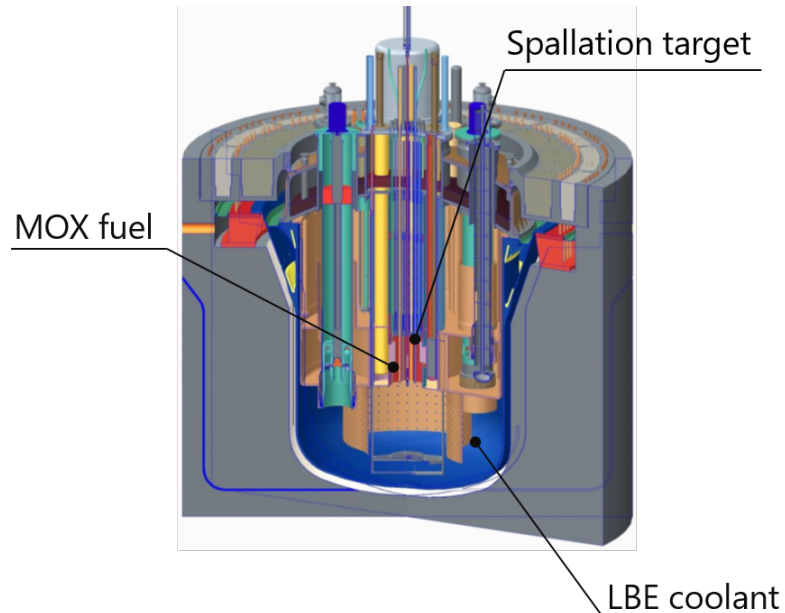


Figure 1.1: MYRRHA reactor glimpse with emphasis to the features analyzed during the work. The picture is taken from [5].

Linear accelerator

The linear accelerator accelerates the protons up to the energy of 600 MeV. At the end of the linac the 4 mA proton beam is injected into the reactor, generating fast neutron fluence by hitting the heavy nuclei in the spallation target of the reactor.

LBE coolant and spallation target

MYRRHA is a pool type reactor and it operates near to the atmospheric pressure. It is cooled by Lead-Bismuth Eutectic (LBE), that also serves as spallation target. LBE has been selected as for several reasons:

- Wide operating temperature range: LBE has a relatively low melting point (125 °C) when compared with its individual components (lead 327 °C, bismuth 271 °C), while it boils only above 1670 °C;
- Excellent heat conductivity: LBE enables the reactor's primary system to operate under normal pressure;
- Radiation shielding: LBE is an excellent radiation shield that blocks gamma radiation.
- Virtually transparent to neutrons: LBE is an ideal medium as spallation source inside the reactor where the linac's proton beam is converted into neutrons required to sustain the fission reaction;
- Fuel mix: LBE allows a wide variety of fuels to be used besides uranium 235 and 238, including mixed oxide fuels. In particular, simulations indicate that linac driven, LBE cooled reactors may contain up to 30% of long-lived minor actinides, such as neptunium, americium and curium;
- LBE based reactors use far less nuclear fuel and produce far less nuclear waste.

MOX fuel

Recycled spent nuclear fuel reprocessed into Mixed Oxide Uranium fuel (MOX) is the target fuel of MYRRHA. MOX pellets with plutonium content of 30% will be loaded in the reactor.

The combination of the three features makes MYRRHA the perfect facility where to perform transmutation of minor actinides since they guarantee fast spectrum and higher fission-to-capture ratio increasing the fuel utilization and creating less by-products by neutron capture. This will have a positive impact on both safety and economics of the final disposal by reducing the waste's total radiotoxicity and the final repository size.

1.2 Source term assessment

The source term refers to the magnitude and mix of the radionuclides released from the different components of the reactor. Determining the source term is a critical component in the licensing process of the reactor since it estimates the amount of

risk associated to a certain accidental condition in term of health and environmental consequences. The source term analyzed in this work comes from MYRRHA fuel and LBE, after being irradiated by particles fluxes. The work carried out for the thesis follows the structure of the source term assessment performed for the previous MYRRHA design versions [6], [7].

Volatile nuclides

Volatile nuclides produced pose the major concern in term of effective dose since they can be released during accidental conditions and spread in the environment outside the reactor envelope. Postulated events bringing to release of volatiles together with the major contributors to the effective dose are already identified and extensively discussed in SCK CEN internal reports. They take as an input the source term produced in previous MYRRHA design versions and new evaluation of the source term is requested to update the safety studies.

Decay heat

The source term is employed to derive the decay heat, i.e. the power generated in a certain component after the shut down of the reactor. It is the energy associated to the decay of the radionuclides composing the source term and it must be equally assessed to establish the cooling requirements of a component after it is unloaded from the reactor. A valuable piece of information is the magnitude of decay heat produced in the fuel assembly when unloaded from the core, used to design and dimension the handling equipment.

1.2.1 Reference accidental conditions and related observables

Accidental conditions

The conditions taken into accounts for the assessment are those in which potentially concerning radionuclides spread in the environment as a consequence of an accidental situation. The accidental conditions are fully analysed in specific SCK CEN internal reports.

- Release of volatile activation/spallation/fission products from the core through the cover gas is assumed in case of large break of the cover barrier or proton beam misalignment causing the beam to burn through the beam tube at cover gas level. The release of fission products happens only if fuel pin crack is assumed [8].
- LBE volatile activation/spallation products also spread in the outer environment in case of failure in the LBE Conditioning System (LBECS failure)

[9].

- FA mechanical failure during unloading procedure in which the failure of all the fuel pins is assumed for conservatism [10].

Radionuclide observables in the accidental conditions

The previous source term assessments provided the results necessary to identify the nuclides responsible to the largest dose in case of accidental release. The present work aims to estimate their production in the new MYRRHA design release and to include other nuclides if relevant.

The exhaustive list of nuclides relevant in each condition is available in the SCK CEN reports carefully describing the accidental sequences.

A reduced list containing the priority nuclides is selected and analysed in this work:

- LBE activation, spallation products: ^{210}Po , that is not only contributing to the dose in case of accident but it is also the driver of LBE decay heat in the short term, ^3H , ^{197}Hg , ^{194}Hg , ^{203}Hg , ^{195}Hg , ^{16}N ;
- volatile fission products produced in the fuel. Noble gases, such as xenon and krypton isotopes, ^{131}I and ^{133}I , ^{134}Cs and ^{137}Cs contributing to the activity after discharge, ^3H , ^{125}Sb and tellurium isotopes such as ^{127m}Te , ^{129m}Te and ^{133}Te .

The activity and decay heat are observables derived directly from the source term. The activity level of fuel and LBE is estimated to assess their radiotoxicity and the major contributors are identified. The same analysis is carried out for the decay heat.

A deeper analysis is performed at fuel assembly level: the activity and decay heat rate of a FA unloaded from the core must be evaluated to establish the safety limits and dimensioning the handling system. Fuel assemblies unloaded from different positions in the core will have different compositions, as a result they will provide different level of activity and decay heat. The unloading of all the FA present in the core at a certain time was simulated to study their decay separately.

The evolution of the decay heat rate is evaluated for a period of 70 years after discharge in analogy with the other outputs, with particular interest to the value after 90 and 420 days of decay, corresponding to the possible moments in which the FA is removed from the IVFS. Moreover the major contributors to decay heat as function of decay time are determined, which contribute the most to decay heat uncertainty.

Chapter 2

Theoretical background

This chapter is devoted to present the theoretical concepts used to carry out the work and to analyze the output obtained.

2.1 Particle-matter interaction

Particle-matter interaction [11] consists of the energy transfer between a projectile particle and a physical target. The nature of interaction depends mainly on the nature of the incoming particle and its energy. For the purpose of the work the discussion is limited to neutrons and protons. The latter are provided by the accelerator and they undergo spallation reactions.

2.1.1 Spallation reactions

A high energy proton beam is employed in MYRRHA as external driver. The beam is produced by a linear particle accelerator, a machine using alternating radio frequency (RF) electromagnetic fields to accelerate charged particles in a straight line [12].

The interactions of high-energy particles with the coolant just below the beam are called spallation reactions. Spallation is a violent reaction in which a target is bombarded by very high energy particles [13]. The impinging particle, proton for example, breaks the target nucleus in several fragments: protons, neutrons, α -particles and other particles are emitted. The general formulation for a spallation reaction is written as

$$p + ST \rightarrow SF_1 + SF_2 + \dots + SF_m + (k)n, \quad (2.1)$$

in which ST is the spallation target and SF are the fragments. The number of neutrons generated k depends on the both the characters involved. The energy

ranges from a few eV to several GeV with the energy of the projectile as upper bound. Spallation targets can be solid or liquid and are usually constituted by high-Z nuclei: an eutectic compound of lead and bismuth is used in MYRRHA.

2.1.2 Neutron-matter interaction

Neutrons are neutral particles and therefore they do not participate in the electromagnetic interaction and do not produce ionization of the atoms. They are generated by several kind of sources: we already discussed about spallation, other phenomena are spontaneous fission and (α, n) reactions.

The main process of neutron interaction [14] with matter is by nuclear forces. Unlike charged particles, neutrons collide rarely with atoms but in these interactions they can lose either all or a large part of their energy, which is caused by the short-range nature of nuclear forces. Since neutrons do not have an electric charge, they freely penetrate through the electron shells of atoms and are not repelled by the Coulomb field of the nucleus.

When considering possible energy transfer among neutrons and other particles it is useful to separate them in several groups depending on the neutron energy. A special group of neutrons are thermal neutrons, those that are in thermal equilibrium and they present a Maxwellian distribution.

The main nuclear reactions the neutrons take part are:

- (n, n) is the elastic or inelastic scattering of neutrons by nuclei;
- (n, γ) is the radiative capture reaction, at which a photon is released from the nucleus;
- (n, α) is the reaction with the emission of an alpha particle;
- (n, p) is the reaction with a proton emission;
- (n, f) is the fission reaction of the nucleus, in which it is split in two (or rarely more) fission fragments

For the sake of simplicity only the most common reactions are listed but other interactions happen with lower probability and they are taken into account during neutronic evaluations.

The interaction probability is defined by the microscopic cross section σ , that represents the impact area of the neutron in the target and for this reason it is measured in barn = $1e - 24$ cm². The microscopic cross section for the interaction i is denoted $\sigma_i(E)$ and it depends on the target nuclide as well as the neutron energy. The probability of absorption is the sum of all the interactions bringing to

the disappearance of the incoming neutron; it is denoted as σ_a and is split amongst capture and fission, eq. (2.2). Neutron scattering changes the neutron position in the phase space, by modifying position, energy and angle. The phenomenon is divided in elastic (σ_{es}) and inelastic (σ_{is}), in which part of the neutron energy is transferred to the target nuclide. The total cross section (σ_t) represents the probability of a neutron to undergo an interaction of any kind.

$$\sigma_a = \sigma_f + \sigma_c \quad \sigma_s = \sigma_{es} + \sigma_{is} \quad \sigma_t = \sigma_a + \sigma_s \quad (2.2)$$

The probability of interaction per unit of path is defined as

$$\Sigma_i(\vec{r}, E) = \sigma_i(E)N_j(\vec{r})$$

and it conveys the exponential reduction of neutron concentration as function of the free flight as shown in eq. (2.3):

$$N(x) = N(0)e^{-\Sigma x}. \quad (2.3)$$

2.2 Transport and depletion

2.2.1 Particle transport

The particle transport describes the evolution of the particles concentration in a certain position in the phase space $(\vec{r}, E, \vec{\Omega})$, by considering all the mechanisms of production, depletion and transport inside the domain [15]. The governing equation for neutron flux is presented in eq. (2.4).

$$\begin{aligned} \frac{1}{v} \frac{\partial \phi(\vec{r}, E, \vec{\Omega}, t)}{\partial t} + \vec{\Omega} \cdot \nabla \phi(\vec{r}, E, \vec{\Omega}, t) + \sigma_t(E)N_j(\vec{r}, t) \phi(\vec{r}, E, \vec{\Omega}, t) = \\ \int d\vec{\Omega}' \int dE' \sigma_s(E)N_j(\vec{r}, t) f_s(\vec{r}, E' \rightarrow E, \vec{\Omega} \cdot \vec{\Omega}') \phi(\vec{r}, E, \vec{\Omega}, t) + Q(\vec{r}, E, \vec{\Omega}, t); \end{aligned} \quad (2.4)$$

The variable that appears in the equation is the neutron angular flux, defined as:

$$\phi(\vec{r}, E, \vec{\Omega}, t) = v N(\vec{r}, E, \vec{\Omega}, t).$$

Three independent variables define the phase space: \vec{r} is the position, E is the energy and $\vec{\Omega}$ is the solid angle $\vec{v} = v \vec{\Omega}$ determining the direction of the motion. The meaning of the microscopic and macroscopic has already been discussed and N_j is the concentration of the background. f_s is the scattering probability density function and it represents the probability that a neutron of direction $\vec{\Omega}'$ and energy E' has to scatter in the direction interval $d\vec{\Omega}$ about $\vec{\Omega}$ with energy in dE about E .

Q represents the source term, that can be of different nature; fixed source providing particles from outside the system and fission processes producing neutrons if fissile nuclides are present in the system. The number of neutrons produced by fission is not constant and it is a function of the target nuclide and of the energy, $\nu(\vec{r}, E')$. The energy of produced neutrons is determined by the probability function $\chi(\vec{r}, E)$ and the process is isotropic so the probability density function for the angular distribution is

$$\int d\vec{\Omega} f(\vec{\Omega}) = 1 \rightarrow f(\vec{\Omega}) = \frac{1}{4\pi}. \quad (2.5)$$

Therefore, the fission term appearing in the transport equation can be written as

$$\int d\vec{\Omega}' \int dE' \frac{\chi(\vec{r}, E)}{4\pi} \nu(\vec{r}, E') \sigma_f(E) N_i(\vec{r}, t) \phi(\vec{r}, E, \vec{\Omega}, t). \quad (2.6)$$

In a critical system the leakages are fully compensated by neutrons produced by fission and the reduced mathematical formulation is the following:

$$\hat{L} \phi(\vec{r}, E, \vec{\Omega}) = \frac{1}{k} \hat{F} \phi(\vec{r}, E, \vec{\Omega}). \quad (2.7)$$

In the formulation of eq. (2.7) the term k , called multiplication factor [16] is introduced; it is the eigenvalue of the equation and associated eigenvector is the solution of the problem ϕ . This mathematical trick allows to make the system critical just adjusting the number of neutrons produced by fission.

Sub-critical system have $k < 1$, the geometrical configuration does not allow criticality and an external source fills the gap. This is the case of an ADS, like MYRRHA, in which the surplus of neutrons is provided by the spallation source.

2.2.2 Depletion equations

Bateman equations [17] describe the evolution of nuclide concentrations in a system undergoing irradiation and radioactive decay. They are a generalization of the exponential decay law and they include every reaction to assess the gross production and depletion of a certain nuclide. The general mathematical formulation, taking into account different particle fluxes and spatial dependence is presented in eq. (2.8).

$$\frac{\partial N_i(\vec{r}, t)}{\partial t} = \sum_j (\lambda_{j \rightarrow i} + \sum_M \int dE \sigma_{j \rightarrow i}^M(E) \phi^M(\vec{r}, E)) N_j(\vec{r}, t) - (\lambda_i + \sum_M \int dE \sigma_{tot,i}^M(E) \phi^M(\vec{r}, E)) N_i(\vec{r}, t) \quad (2.8)$$

The following notation is used:

- i, j are the indices of nuclides;
- $\lambda_{j \rightarrow i}$ is the decay constant in which j is the mother and i the daughter;
- λ_i is the decay constant of i ;
- M stands for the particle fluxes involved;
- $\sigma_{j \rightarrow i}^M$ is the microscopic cross section for the reaction producing i when j interact with the particle M ;
- $\sigma_{tot,i}^M$ is the removal cross section of i when interacting with M ;
- $\phi^M(\vec{r}, E)$ is the flux of particle M .

The closed set of first order integro-differential equations can be written in matrix form and solved by numerical scheme, its solution is the evolution of the nuclide vector in the system ($\vec{N}(t)$).

2.2.3 Coupling transport and depletion

The variables $N_j(\vec{r}, t)$ in 2.4 and $\phi(\vec{r}, E, t)$ in (2.8) establish the coupling between transport and depletion since the spectrum coming from transport simulation is necessary to estimate the reaction rates appearing in the Bateman equations

$$\langle \sigma_{j \rightarrow i} \phi \rangle = \int dE \sigma_{j \rightarrow i}(E) \phi(\vec{r}, E) \quad (2.9)$$

and the updated nuclide vector must be fed to the transport model and it affects the new flux.

The time coupling is therefore often solved by separation of spatial and temporal components of the solution. This approach evaluates both the neutronic evolution and the nuclides concentrations in the system.

2.2.4 Derived quantities

The nuclide vector is employed to estimate other quantities of major importance for the analysis such as activity and decay heat. The activity is defined as the number of decays per unit time so it is proportional to the atomic density, multiplied for the decay constant λ . So the activity evolution of a certain nuclide mimics the concentration evolution. The same applies for the decay heat rate, the other quantity relevant in this work. It consists of the energy released in the decay Q_i

multiplied by the decay rate of a nuclide (that is the activity).
 Mathematical expressions of the two quantities are shown in Eqs. (2.10).

$$\begin{aligned} A(t) &= \sum_i \lambda_i N_i(t) \\ DH(t) &= \sum_i Q_i \lambda_i N_i(t) \end{aligned} \tag{2.10}$$

2.3 Uncertainty quantification

Uncertainty quantification [18] is the science that aims to characterize an experiment or computational model estimating the associated uncertainties. Its purpose is to determine the likelihood of a certain output if some of the aspect of the system are not exactly known. The methodology is widely spread in the nuclear field in general and in neutronic calculations in particular to provide confidence intervals of the relevant quantities evaluated. Uncertainty quantification is needed as it complements the information given by the best estimate coupling it with a reliability analysis; moreover it is relevant from a more technological point of view to verify and properly establish the many safety margins foreseen for the nuclear installations. In a neutronic simulation the uncertainty associated to the output is a combination of different sources that must be investigated separately to assess the global variability of the parameter of interest.

2.3.1 Sources of uncertainty

The sources of uncertainty to take into account in the case study, transport and depletion calculation in MYRRHA, are the possible variabilities of the model with respect to the real reactor design and operation.

The first source of uncertainty is related to the input parameters, since the model is fed by the best-available information on the design but there is still a certain flexibility. For example the compositions of MOX fuel and LBE coolant are not defined accurately yet and the deviation from reference compositions have to be taken into account. Besides, slight variation in operational history can influence the power and the burnup bringing deviations to the nuclide vector of the fuel for example.

Neutronic and depletion calculations strongly rely on nuclear data evaluated through experiments and mathematical models. Specific data for each nuclide are provided as best-estimate evaluation and associated uncertainties in the form of covariance matrices. The impact of nuclear data on criticality parameters and SNF concentrations is well assessed and several methodologies are adopted in the field [19], [20].

2.3.2 Uncertainty propagation and statistical sampling

In this section the methodologies to perform uncertainty propagation are described [21] with particular focus to nuclear data uncertainties and statistical sampling procedure. The first method, based on perturbation theory, makes use of the covariance matrices of nuclear data and sensitivity profiles. Sensitivity profile is defined as the relative change in a response parameter caused by a small variation in a cross section data at a certain energy as shown in 2.11:

$$S_R = \frac{\delta R/R}{\delta \sigma_g/\sigma_g} \quad (2.11)$$

The sensitivity profiles obtained are combined with nuclear data covariance matrix Σ to propagate nuclear data uncertainties using the so-called first-order uncertainty propagation formula (or sandwich rule) [22], as shown in eq. 2.12.

$$Var_R = S_R \Sigma S_R^T \quad (2.12)$$

The upscaling of computational power in the last few years gave the possibility to investigate new methods to propagate uncertainty. One of the most prominent is based on stochastic sampling of nuclear data [23]. Perturbed nuclear data files are generated to be fed in the model. The uncertainty of the output response under investigation is determined as the standard deviation of the output population using the standard definitions reminded in eq. (2.13).

$$\begin{aligned} \mu &= \frac{\sum_i^N (x_i - \bar{x})}{N} \\ Var &= \frac{1}{N-1} \sum_i^N (x_i - \bar{x})^2 \end{aligned} \quad (2.13)$$

The main advantages of statistical sampling procedure are the independence from the model and the possibility to investigate higher order effects thanks to the inherent characteristics of the method. The limit is found in the computational cost since a large sample is required to get statistically significant results.

Samples of nuclear data are generated from a multivariate normal distribution $\mathcal{N}(\mu, \Sigma)$. The procedure to obtain n samples consists of applying Σ to a matrix X $m \times n$ of identically and independent variables distributed according $N(0,1)$. The perturbation coefficients are produced according to eq. (2.14):

$$P = LX + 1 \quad (2.14)$$

where

$$\Sigma = LL^T.$$

The matrix L that fulfills the relation is obtained decomposing the covariance matrix. The use of this specific factorization is possible thanks to the properties of the covariance matrix itself, being symmetric and positive semi-definite. P , the matrix of perturbation coefficients is applied to nuclear data such as cross sections, neutron fission product yields, angular and energy distributions to estimate the uncertainty coming from these parameters. In this analysis the contribution of neutron cross sections and fission yields is assessed.

The procedure is validated for a set of 200 sample (the number used for the analysis), assessing the convergence of the perturbation coefficients standard deviation to the standard deviation given in input. In addition the output distribution of the

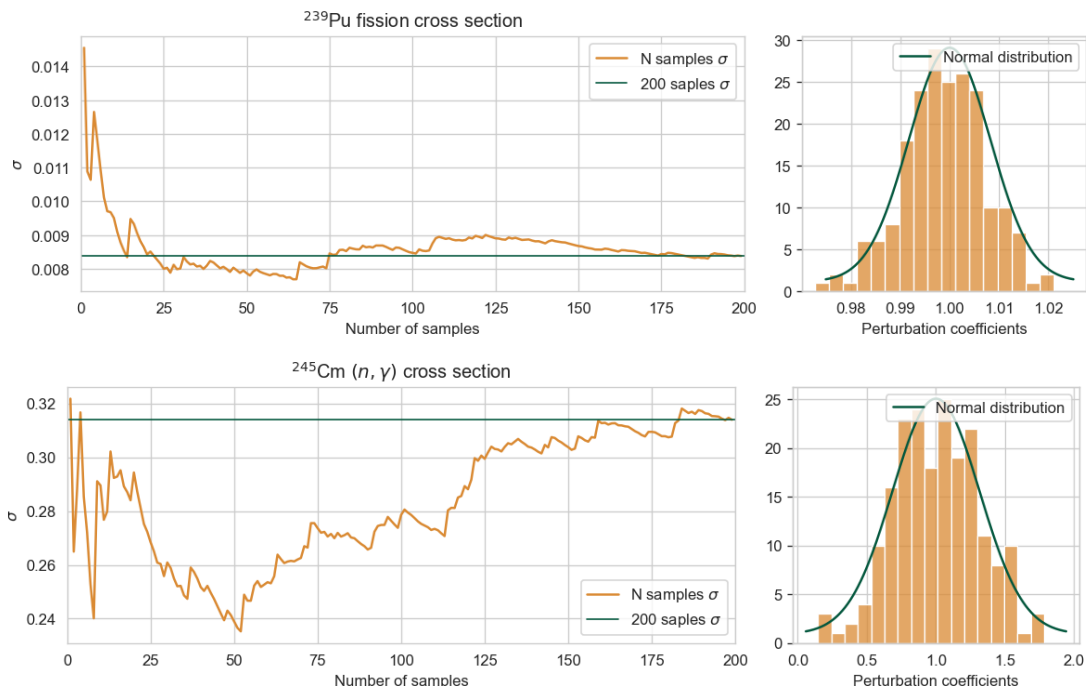


Figure 2.1: Convergence analysis on the perturbation coefficients of ^{239}Pu fission cross section and ^{245}Cm neutron capture cross section @Energy = 0.1 MeV in top and bottom figure respectively. The perturbation coefficients sample distribution is shown on the right part of the plot for both cross section data.

perturbation coefficients is shown, to qualitatively assess the correspondence to the selected sampling distribution. They are presented in Fig. 2.1. The perturbation coefficients chosen come from the fission cross section of ^{239}Pu in the energy range around 0.1 MeV, that is the most relevant for this application. The fission XS has low uncertainty in this range and it is fast to converge. Then the perturbation coefficients of ^{245}Cm capture XS are shown. The reaction is relevant

since it produces ^{246}Cm that is the nuclide with largest uncertainty among those analysed in this work, as presented in Sect. 8.1.1. The convergence of this cross section is much slower compared to the previous one, as shown in the bottom plot of Fig. 2.1.

2.4 Codes and data employed

In the following, the main tools and codes used to obtain the reported results are presented. The list shows the different topics addressed during the project.

2.4.1 Monte Carlo codes for particle transport

Monte Carlo codes are used to mimic the transport of particles inside a system by means of stochastic simulation of the phenomena involved [24]. Their motion inside the system is traced and it allows to determine the average behavior of the particles simulated retrieving their energy and spatial distribution. Monte Carlo simulations provide the result of the general transport equation without directly solving it as opposed to deterministic codes based on the discretization in space, energy and angle, the three phase space parameters.

The main advantages of MC methods are possibility to handle complex geometries, materials and nuclear data, providing very accurate results with the statistical uncertainty associated. The drawback is that the convergence is slow since it is proportional to \sqrt{N} for all statistical method with N equal to the number of histories simulated.

Several Monte Carlo particle transport codes are available and provide different features. The following discussion is limited to the codes employed in this work.

MCNP6

Monte-Carlo N-Particle (MCNP) [25] is one the most prominent codes available. It is commonly adopted for nuclear reactor modeling and it has been extensively validated and constantly maintained during its 40 years history.

The main requirement to fulfill for MYRRHA core modeling is the transport of protons, together with neutrons to mimic the proton source and the neutrons consequently generated from it by means of spallation reactions. MCNP fully complies to this requirement. However, MCNP is not able to perform materials depletion by itself and it has to be coupled by a depletion solver. This task is accomplished by ALEPH2 [26], that will be fully discussed in Sect. 2.4.2.

Serpent-2

Serpent [27] is a multi-purpose continuous-energy neutron and photon transport code, developed since 2004. It is widely used for particle transport applications in particular reactor modeling. Serpent has built-in burnup calculation capability, performing depletion of burnable materials in the simulations. Depletion zone division can be implemented to discretize the fluxes into the same material to estimate spatial dependent depletion; this feature is used in the thesis to investigate the influence of axial burnup.

With respect to ALEPH2, Serpent is much faster but it needs larger hardware requirements since nuclear data are stored in the RAM. The calculation speedup makes is very promising to perform calculations involving uncertainty propagation. The main limit of Serpent, related to this case study is that it is not able to transport protons; this implies only the MYRRHA critical model can be simulated in Serpent.

2.4.2 ALEPH2

The general-purpose burn-up code ALEPH2 wraps around MCNP/X Monte-Carlo radiation transport code and an advanced depletion code to solve the Bateman system of ordinary differential equations. It was developed in SCK CEN and recently upgraded to ALEPH v2.8. With respect to ALEPH1 some modification were introduced coming from user feedbacks and new necessities. The main upgrades involve the depletion code in use since ORIGEN-2.2 [28] was replaced by the advance depletion solver based on RADAU5 implicit Runge-Kutta algorithm. Besides, new features were implemented such as the predictor corrector, heating calculation during irradiation and decay and the calculation of neutron sources during the decay.

The working principle of burn-up codes in general "and ALEPH2 in particular" is to take particles spectra and fluxes from the Monte Carlo simulation to generate the reaction rates to feed the depletion solver. Then, the output of the depletion calculation updates the input of the transport simulation for a new run. Briefly, burn-up codes take care of the coupling between transport and depletion, discussed from the theoretical point of view in the previous section.

The main advantages of ALEPH2 among other codes is the full nuclear data consistency, since the same energy grid is used both in transport and subsequent depletion calculation. Moreover, as already mentioned the code wraps around MCNP and the complexity of utilization is limited to the addition of a number of extra cards to the Monte Carlo transport simulation input. ALEPH2 generates the MCNP input and when the transport simulation is completed it automatically extracts the fluxes in the materials/cells we are interested to burn. After depletion procedure is performed, the materials compositions are updated accordingly. The

possibility to change materials is also implemented to allow considering system configuration variation, like the fuel assembly shuffling in a core simulations or the variation of boron concentration in PWRs coolant.

The main advantages of ALEPH2 for our specific case, being MYRRHA an ADS is that the code takes into account protons matter interactions. Moreover it gives the possibility to perform stand alone calculations, reading particle fluxes from external files and carrying out depletion calculations without the necessity of calling upon MCNP. This specific procedure is implemented for the LBE source term calculation as described in the following and it allows to speedup the calculation assuming the fluxes do not change from one irradiation cycle to the other.

2.4.3 SANDY

SANDY [23] is a tool created to manage nuclear data file in ENDF-6 format. The code is able to read ENDF-6 file [29] and to perform operations with them. It interfaces with NJOY [30], creating input files and reading the outputs to provide processed nuclear data, for example multigroup cross sections and covariance matrices. The main objective of SANDY is to perturb nuclear data starting from the processed data and generate perturbed files readable by Monte Carlo codes to carry out uncertainty propagation by statistical sampling.

The format used by some MC codes is called *ACE* and the processing, also in this case case, is performed through a NJOY module. Perturbation of nuclear data is possible for cross sections, neutron fission product yields and $\bar{\nu}$, but it has being implemented for other class of nuclear data contained in ENDF-6 files. The procedure to obtain perturbed data was briefly described in Sect. 2.3.2, starting from normally distributed random samples, to which the covariance matrix is applied to obtain relative perturbation coefficients.

The choice of the multivariate normal distribution is driven by the Central Limit Theorem [31], it establishes that the mean values of samples taken from a certain population converge to the normal one if a sufficient sample size is achieved. This implies whatever input distribution the output of the model will be normally distributed if the number of sample is large enough. So it seems the easiest choice to take normally distributed inputs. The other available option given by the code is the lognormal distribution that can be used to assess the bias given by the input distribution but it is out of the scope of this thesis.

The production of the samples to carry out uncertainty propagation of the models developed gave the opportunity to understand and to test different features of the sampling procedure implemented in SANDY; the contribution to some updates in the code, to fix bugs encountered during the procedure was part of the thesis work, that has been carried out under the supervision of the main developer of the code Luca Fiorito.

2.4.4 NJOY

NJOY is a comprehensive computer code developed to process nuclear data. It produces pointwise and multigroup nuclear cross section and related quantities from evaluated nuclear data files in ENDF-6 format. It comprises many modules and each of them performs a certain task. As already mentioned SANDY code generates NJOY inputs requested and it reads and converts the outputs in a user friendly format on a python interface. NJOY2016 includes a module called *ACER* to translate ENDF-6 in *ACE* format, the one requested by MCNP and Serpent MC codes.

2.4.5 Nuclear data libraries

Nuclear data are the main input data to feed to a neutronic simulation and it means their availability and accuracy is on main importance to obtain meaningful results. Nuclear data include energy dependant reaction cross sections, the energy and angular distributions of fission neutrons, fission product yields and the atomic and nuclear properties of excited states as well as their radioactive decay data.

Nuclear data are stored in libraries and different source are available coming from different evaluators. For this work some libraries are compared to assess the discrepancies and choose the best one tailored on this specific application, the one more complete in term of the nuclides we are interested in.

The three libraries used in this work are JEFF [32], the joint evaluated fission and fusion nuclear data library, ENDF [33], the U.S.'s Evaluated Nuclear Data File and JENDL [34], the Japanese evaluated nuclear data library. Among the several versions available, those chosen for performing the simulations are :

- JEFF-3.1.2 [35]
- JEFF-3.3
- ENDFB-VIII.0
- JENDL-4.0u

The older release of JEFF is used in the reference neutronic model calculation and the LBE depletion simulations. The comparison with the other libraries listed above is performed to assess the discrepancies in term of nuclide concentrations and to select the evaluated data giving more conservative results. The largest prediction among the libraries is chosen to be conservative since is not possible to affirm a priori which library works better in a certain system and the reason for certain divergences in the outputs.

For fuel assembly simulations the results presented in the following are obtained

using the newer release of JEFF, JEFF-3.3. Deviations in the nuclides concentrations coming from nuclear data variation are shown and uncertainty propagation of neutronic cross section investigates the discrepancy due to the uncertainty of nuclear data themselves. The main focus is on the largest uncertainty for each nuclide giving the upper limit concentration for the nuclide examined. Neutron fission product yield uncertainty analysis is only performed with data coming from JEFF-3.3.

High energy incident neutron data

Most of neutron libraries commonly have cross section data up to an energy of 20 MeV, that is the upper limit for neutrons coming from fission. However, in ADS applications the energies spans to much higher energies and cross sections for high energy reactions must be taken into account. For this purpose a tool from ALEPH2 provides custom libraries comprising cross sections data up to 20 MeV to which other libraries are appended. In case of JEFF-3.1.2 library in the reference calculation the high energy data are provided by two additional sources, in particular TENDL-2013 [36] to cover energy range 20-200 MeV and HEAD-2009 [37] high-energy activation library to add data above 200 MeV.

High energy incident proton data

The proton reference library used for sub-critical configuration is produced in ALEPH2, merging nuclear data coming from several evaluators to provide the most complete information possible. JENDL and JEFF data are combined to TENDL to provide comprehensive data up to 200 MeV. HEAD-2009 is used to cover the higher energy range of the spectrum.

Chapter 3

MYRRHA reference model

3.1 MYRRHA reference model description

The model of MYRRHA design revision 1.8, presented in [38], represents a detailed 3D neutronic model reproducing the latest design of the reactor. In this work it is used as a reference to study the source term in the LBE and the MOX fuel present in the reactor.

Core layout

The core is modeled both in critical and sub-critical configuration. The cross sectional view is shown in Fig. 3.1. The names of the assemblies follows the

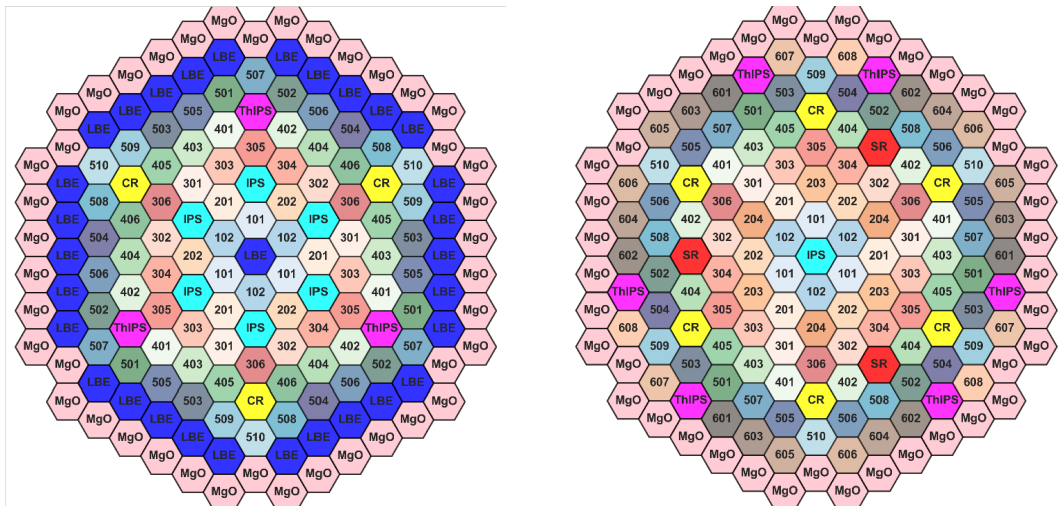


Figure 3.1: Schematic cross sectional view of the core in sub-critical (left) and critical configuration (right).

scheme:

- 101-608: fuel assemblies grouped in batches;
- LBE: dummy assemblies filled with coolant present in sub-critical condition to fill the empty core spaces;
- CR: control rod bundle;
- SR: safety rod bundle;
- IPS/ThIPS: in-pile section where to perform the irradiation experiments of the samples, Th stands for thermal, a softer spectrum is achieved. Used for the production of radioisotopes;
- MgO: external ring of reflector assemblies to reduce the neutron leakage from the radial boundaries.

The plots show the layout of the core at Beginning of Cycle (BoC), i.e. when the equilibrium condition is achieved. The concept of equilibrium is discussed thoroughly in the dedicated section, Sect. 3.2. This is the layout always taken into account for the calculation, when the dynamic steady state is achieved. The same core layout is present at the end of the irradiation cycle, that is called EoI, even if the neutronic conditions vary during the cycle because of fuel depletion.

The core configuration at startup is called Beginning of Life (BoL) and it comprises more LBE dummy assemblies in both configurations. During operation, from cycle to cycle, the empty spaces are filled with fuel assemblies. At BoL all fuel loaded in the core are fresh so less assemblies give the necessary neutronic multiplication.

FA reshuffling procedure

Fuel assemblies are reshuffled in the core following a IN-to-OUT procedure in which two batches of three assemblies are loaded and unloaded every cycle. The core presents 1/3 azimuthal symmetry so each assembly of the batch undergoes the same irradiation history. The assemblies are unloaded after a variable number of cycles depending on the batch and the mode; the discharge burnup is around 50 MWd/kg for the fuel assemblies in normal operation. In normal operations the fuel assembly unloading happens in the core periphery, after the FA is reshuffled in all the available core positions. Early unloading is envisaged in case of off-normal situations.

Operational history

MYRRHA operational period comprises irradiation cycles of 90 days followed by a maintenance period of 30 or 90 days in case of short or long maintenance as depicted in Fig. 3.2. To assess the source term in the fuel the irradiation of a

Table 3.1: Core configuration summary

	BoL	BoC	BoL	BoC
<i>Fuel assemblies</i>	54	78	69	105
<i>Dummy assemblies</i>	54	30	36	-
<i>Reflector assemblies</i>	42	42	42	42
<i>Control rods</i>	3	3	6	6
<i>Safety rods</i>	-	-	3	3
<i>Fast IPSs</i>	6	6	1	1
<i>Thermal IPSs</i>	3	3	6	6
<i>Spallation Target</i>	1	1	-	-
<i>Total</i>	163	163	163	163

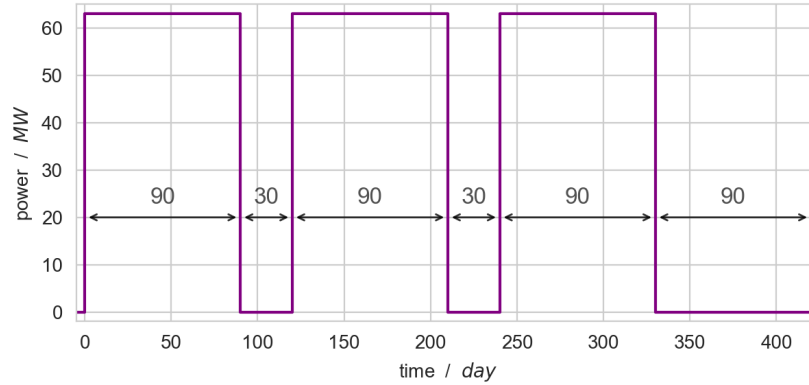


Figure 3.2: Example of irradiation history in MYRRHA, showing one period made of three irradiation and maintenance cycles.

FA being reshuffled in the core was considered, while the irradiation of LBE lasts the whole operational period of the reactor, that is assumed to be 40 years since no coolant replacement is scheduled during the reactor life. The end of the last irradiation cycle before permanent shut-down of the reactor is called End of Life (EoL). The acronyms BoL, BoC, EoI, EoL will be used in the following to define the moment in the operational history.

3.2 Equilibrium cycle definition

The equilibrium condition provides the steady state pattern of fuel assemblies in the core, that stays constant from cycle to cycle performing in-core fuel assemblies reshuffling, loading of fresh FAs in the center and unloading of burnt assemblies from the periphery [39]. The particle flux distributions and spectra vary during the equilibrium cycle as well as the the k_{eff} because of burnup increase associated to fuel depletion, but they come back to the initial condition at the beginning of following cycle since the same fuel assembly pattern is restored. Two separate states are considered for the equilibrium: BoC and End of Cycle (EoC); they are identical in each irradiation cycle.

3.2.1 Initial conditions

The equilibrium condition can be achieved for any core configuration and it is fixed by input and design parameters:

- Configuration at BoL: position of IPS, safety and control rods SR, CR;
- Normalization factor - Core power;
- Number of fuel assemblies in the reactor core;
- (Un)Loading and shuffling scheme: number of assemblies loaded and discharged from the core in each cycle and the pattern they follow along the core (IN-to-OUT reshuffling);

The parameters are defined according to design constraints, to achieve criticality in critical mode and to optimize the fuel utilization. The core layout and the reshuffling procedure were already discussed in the previous section, as regard the core power in critical mode it is 63 MW thermal power, while it is 55 MW for the sub-critical configuration.

3.2.2 Equilibrium core modeling

The core fuel assemblies pattern that characterizes equilibrium is attained performing a number of consecutive burnup cycles. Fresh fuel assemblies are present throughout the core at the beginning of the first cycle, then the specified fuel reshuffling, loading and unloading procedure is carried out for a certain number of cycles. A steady state condition is reached when the fuel assemblies pattern does not change anymore from cycle to cycle the FAs with a certain burnup level have always the same location in the core.

3.2.3 Convergence analysis

The achievement of the equilibrium cycle is practically assessed tracking the evolution of the relevant neutronic parameters during successive irradiation cycles to verify their convergence to an equilibrium value. The study is carried out for the multiplication factor, the most important parameter for a critical reactor. Fig. 3.3

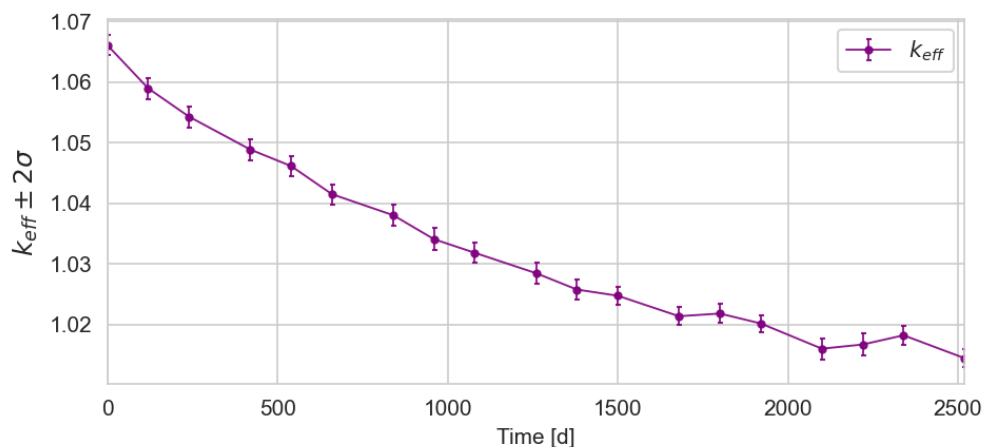


Figure 3.3: Convergence analysis of k_{eff} in the critical core model.

shows k_{eff} value stabilizes after 36 irradiation cycles and this core configuration is taken as the reference for the condition at BoC.

The outputs of equilibrium cycle provide valuable pieces of information employed both as input and output of the simplified depletion models, developed to avoid to perform the depletion calculations directly on a full core model that would require larger computational cost. The behaviour at BoC, the fluxes profiles and particle spectra are fed to the LBE irradiation model as described in the following chapter. The FAs nuclide concentration at EoC is investigated and the power profiles are employed as input of FA models aiming at determining fuel source term and associated uncertainty.

Chapter 4

LBE depletion model

This chapter gives details of the methodology and the assumptions made to develop a depletion model suitable to estimate the concentration evolution of the radionuclides produced in the LBE. The studies in this work are based on the source term data and analyses for the MYRRHA design revisions 1.4 and 1.6. In addition, the impact of the modeling assumptions is investigated.

4.1 Modeling assumption

The LBE depletion is calculated for the MYRRHA sub-critical configuration assuming a equilibrium core. What emerges from previous source term studies [6], [7] is that the sub-critical mode of operation generates the largest LBE activity. Besides, most of the radioactive nuclides responsible for the LBE activity are produced directly/indirectly by proton-induced spallation reactions, i.e., a mechanism not present in a critical reactor.

LBE static simulation

The LBE is considered stagnant, that is, the coolant forced circulation in the reactor and the mixing phenomena are not modelled. Recycling effects not taken into account can have an impact on the production/depletion of certain nuclides.

No replacement of filtering of the LBE during the reactor lifetime

All radionuclides produced from LBE activation during reactor operation are retained in the LBE for the entire lifetime of the reactor, i.e., 40 years. This assumption neglects the migration of volatile activation products to the cover gas [40] (as postulated in one of the DBAs), and results in a conservative estimation of the source term where the concentration of volatile radionuclides in LBE is overestimated.

Transport/depletion decoupling

Proton and neutron fluxes and spectra are calculated only once at BoC, and then they are adopted for the LBE depletion throughout the entire reactor lifetime. This assumption follows the definition of equilibrium cycle discussed in Sect. 3.2. Also, the in-cycle spectral variations are neglected. The neutron and proton spectra calculated in the STA are displayed in Fig. 4.1.

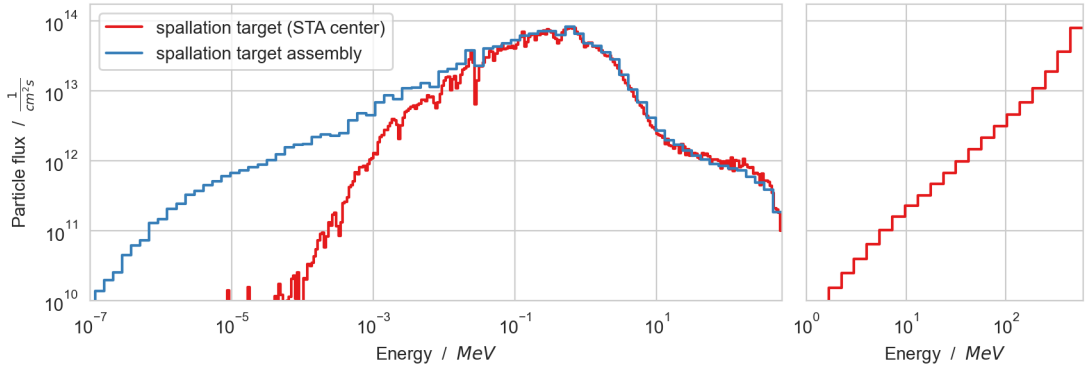


Figure 4.1: Neutron (left) and proton (right) energy-dependent flux in the spallation target at BoC. The neutron flux in the whole spallation target assembly is depicted in blue.

LBE discrete regions depending on irradiation conditions

The depletion of the LBE coolant was simulated independently for three volumetric regions of the reactor characterized by different irradiation conditions, e.g., particle fluxes and spectra:

- Spallation target assembly (STA);
- Reactor core (without the STA);
- Reactor pool.

For each region, volume-average particle fluxes were used for the LBE depletion calculation. This approach is in line with the previous analysis carried out for the LBE source term assessment of the MYRRHA Design Revision 1.4. For the MYRRHA Design Revision 1.6 only one volumetric region was adopted, for which volume-average particle fluxes were used. The region included the STA, the reactor core and the reactor pool. In this work the two approaches are compared for the LBE source term of the MYRRHA Design Revision 1.8.

The *spallation target assembly* is characterized by a 600 MeV-proton beam impinging on the LBE spallation target and inducing spallation reactions that yield high energy neutrons into the system. The LBE source term in this region is dominated by spallation products and high energy neutron activation products.

Because of the proton short stopping range in LBE and because of the direction of the proton beam, only a negligible proton flux is available in the *reactor core*. Compared to the *spallation target assembly* the neutron spectrum in the reactor core is softer as it mostly generates from neutron-induced fission in the driver MOX fuel. Still, a high-energy tail of spallation neutrons is still present. In the *reactor core* region most of the source terms radionuclides produced in LBE are produced via neutron activation.

In the *reactor pool* the neutron fluxes and spectra, respectively, have a lower intensity and are softer (because of the multiple neutron-scattering reactions in LBE) with respect to those in the core. The main production mechanism for the source terms radionuclides in LBE is neutron activation.

4.2 Spallation target assembly sub-division

The most critical region in term of LBE activation is the Spallation Target Assembly (STA) [41] since most of the spallation products are produced there. In the STA the production rate of neutron activation products is also maximized because of the very high neutron fluxes. For this reason the rest of the LBE source term assessment concentrates on the analysis for this region, giving conservative results in term of activity and decay heat produced in the LBE. The LBE source term study for the STA starts from a deeper analysis of the proton and neutron fluxes in the considered region.

Fig. 4.2 depicts a 2D map (XZ-view on the left, XY-view on the right) of the proton fluxes in the STA. Protons are relevant for the LBE activation only within their stopping range, i.e., in the region right below the beam window. The plot also shows that proton flux radial spread is limited to the STA wrapper. The left plot in Fig. 4.2 shows a strong proton flux axial gradient (with a significant axial zone without protons). This is an indication that using assembly-averaged proton fluxes in depletion analysis might not produce correct source term estimates. A refinement of the depletion model with a sub-division of the STA into three axial regions is proposed as a correction.

The axial distribution of the proton flux is presented in the form of cumulative distribution in Fig. 4.3. It suggests to divide the assembly into three regions:

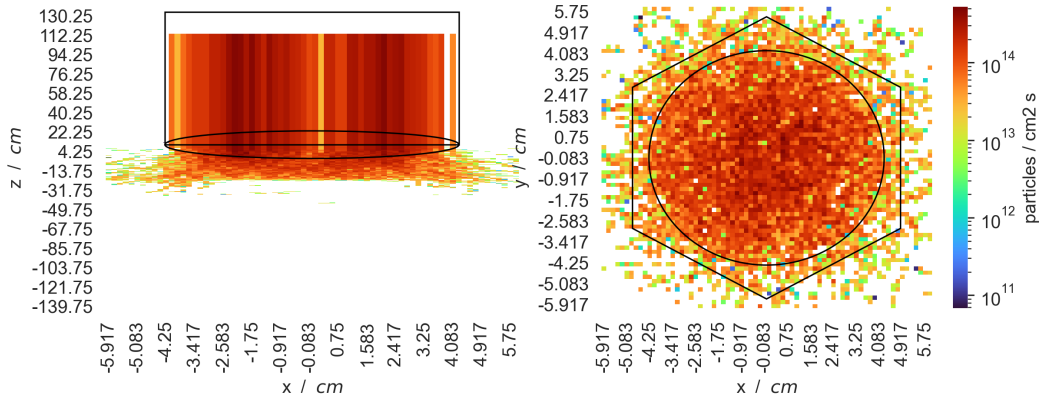


Figure 4.2: Proton flux distribution in the spallation target assembly. xz view on the left, xy cross section 5 cm below the beam window on the right.

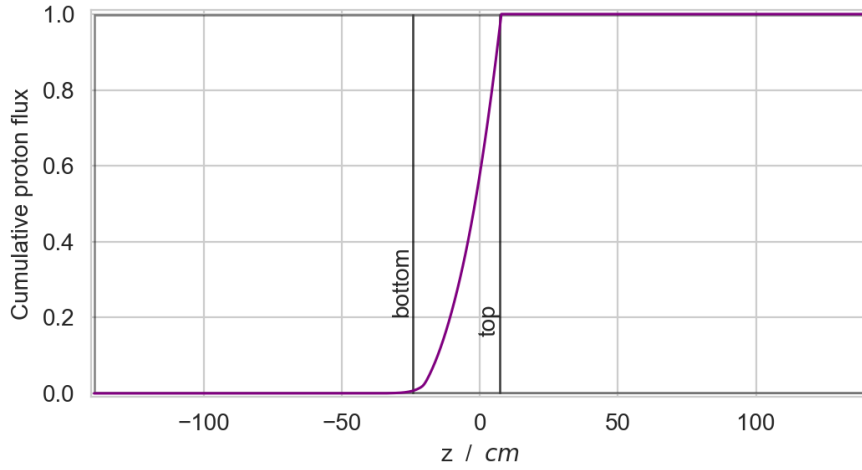


Figure 4.3: Cumulative proton flux integrated in axial direction.

- the (axially)-central region consisting in the actual spallation target as it covers the entire proton stopping range in LBE. The LBE source term in this region is generated by nuclide interactions with protons and high energy neutrons;
- the upper region where the neutron fluxes are still high but the presence of the protons is negligible;
- the lower region, with neutron and proton flux characteristics similar to the upper region, but including a lower LBE volume.

The neutron and proton fluxes in the STA were already reported in Fig. 4.1,

above.

In this work, the main objective for the analysis of the LBE source term in the spallation target assembly is to assess the deviations arising from a zone division approach, as well as to evaluate the actual inventory of safety relevant nuclides during irradiation and after shutdown.

LBE depletion simulations are carried out for each of the three STA axial regions previously identified. The spectral shape and the intensity of the neutron and proton fluxes were calculated for the entire STA volume and for the central axial region. The latter were used for the LBE depletion of the STA central region. The neutron flux (not the proton flux, which was assumed negligible) calculated in the entire STA volume was used for the depletion of the STA lower and upper regions, after correctly re-scaling the flux intensity to account for the different LBE volumes.

The volume-weighted sum of the nuclide inventories calculated in the three regions was compared to the nuclide inventory predicted for the entire STA using a single depletion calculations with volume-average fluxes. The latter will be later referred to as the *homogeneous approach*. The discrepancy between the two approaches is assessed and the outcome for the relevant nuclides, discussed in Sect. 1.2.1, is presented in Fig. 4.4. The impact of a zone division approach

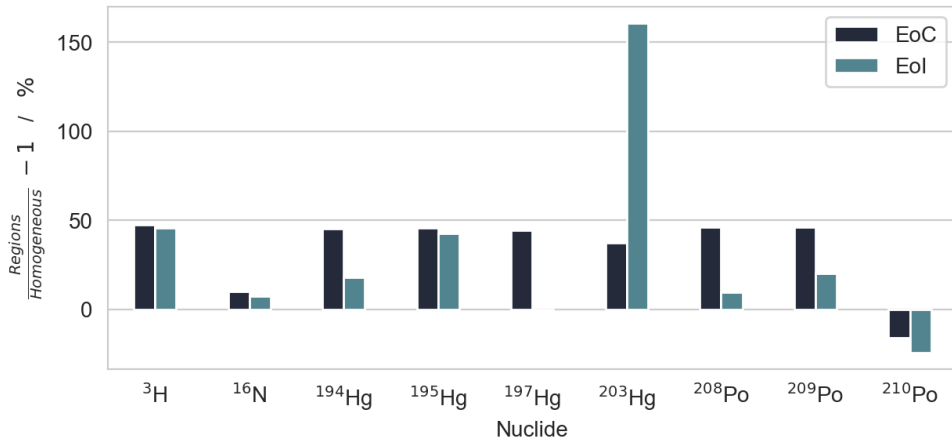


Figure 4.4: Variation in nuclide activity in STA due to the modeling assumptions. Impact of zone division is exploited.

at the STA level is not negligible. All the spallation products and ^{208}Po , ^{209}Po are underestimated by the homogeneous approach because of their non-linear dependence on the proton flux intensity. ^{210}Po is mainly produced by neutron

interactions ((n,γ) in ^{210}Bi) and it is slightly overestimated by the homogeneous approach. This information is valuable since ^{210}Po is the most safety concerning nuclides and one of the main "showstopper" for the design of MYRRHA and analogous facilities because of its radiotoxicity.

The production of spallation products in the spallation target assembly is underestimated by a homogeneous depletion of the entire LBE volume in the STA. On the contrary ^{210}Po is overestimated by this approach.

4.3 ALEPH2 update verification

ALEPH2 has been updated from version 2.5, which was used for calculations of the LBE source term for the MYRRHA design revision 1.6, to the latest version 2.8. The verification of the latest ALEPH2 release for the LBE source term calculations was carried out as a part of this work and it consists of comparing the old outputs with a simulation using the new ALEPH2 version. Neutron and proton spectra were both taken from neutronic simulations of the the MYRRHA sub-critical core for the Design Revision 1.6, to not introduce a bias due to the reactor core updates. The major contributors to the activity are compared and their deviations are shown

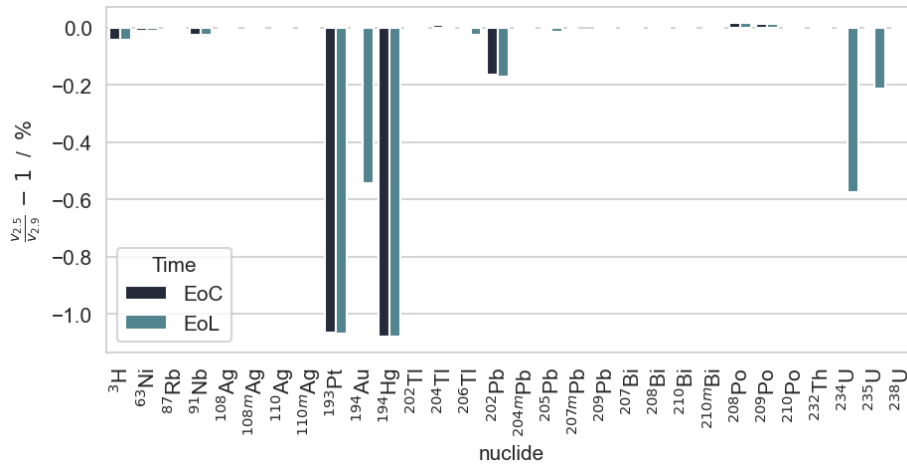


Figure 4.5: Comparison between two ALEPH2 versions of the major contributors activity after 1 irradiation cycle and after 40 years of operation.

in Fig. 4.5. The variations are lower than 1% for the nuclides taken into account so we can conclude that the updates in the code do not affect the results for this specific case study.

The ALEPH2 code update from version 2.5 to version 2.8 affects the LBE nuclide inventory predictions by less than 1%.

Chapter 5

LBE source term - Spallation target assembly

This chapter summarizes the results of the LBE depletion simulations in the spallation target assembly. The outcomes of the homogeneous approach are presented and compared with the evaluations obtained with the zone-division approach.

5.1 LBE inventory in the STA

The elemental composition of the irradiated LBE is reported in Tab. 5.1. It is normalized on the mass of LBE present in the STA before irradiation. The results refers to the EoL concentrations after 40 years of irradiation in the reactor. The elemental composition is globally influenced by the initial impurities present in the LBE and locally from the fluxes in each region.

The table clearly shows that most of the activation and spallation products are generated in the central region. The elemental content in the whole spallation target assembly calculated with the homogeneous approach differs from the the volume-weighted sum of the concentrations in each region, as reported in Fig. 5.1. This confirms that discrepancies arise if the depletion is performed averaging the condition in the STA instead of considering separate regions. The same conclusion was drawn from Fig. 4.4, shown in the previous chapter.

Table 5.1: LBE spallation and activation products concentrations in the STA at the end of life (EoL) after 40 of operation.

Element	Initial concentration (mg/kg)	Bottom region (mg/kg)	Central region (mg/kg)	Top region (mg/kg)	Whole LBE in STA (mg/kg)
H	0.00	13.53	2859.43	23.58	347.42
He	0.00	21.80	1179.17	36.83	172.82
Kr	0.00	0.97	1072.97	1.68	124.40
Sr	0.20	1.17	1056.43	1.87	125.70
Zr	0.23	1.25	1357.23	1.97	176.92
Mo	0.12	1.15	1554.85	1.90	201.03
Ru	0.03	1.05	1468.16	1.80	190.40
Pd	0.34	1.42	1492.65	2.17	188.14
Cd	0.23	11.46	1133.41	15.39	172.63
Sn	1.33	2.18	876.59	2.83	117.72
Er	0.02	0.14	778.04	0.22	37.45
Yb	0.00	1.15	2444.79	2.01	182.68
Lu	0.18	0.78	826.41	1.12	72.68
Hf	0.00	5.55	5995.54	9.48	591.98
Ta	0.00	2.79	1883.80	4.16	182.05
W	0.00	10.99	6919.96	19.48	810.23
Re	0.00	3.75	1206.73	4.74	118.66
Os	0.05	68.32	19658.87	118.84	2499.83
Ir	0.00	21.23	2979.66	25.40	333.20
Pt	0.14	185.25	33060.42	331.37	4381.94
Au	0.53	61.61	5702.84	83.39	615.91
Hg	1.73	983.64	58458.96	1700.19	9411.62
Tl	0.00	616.04	17942.85	1056.28	3078.49
Pb	444908.35	446378.18	384549.00	447401.66	439867.17
Bi	554910.38	551217.54	408631.32	548610.20	531518.27
Po	0.00	14.12	699.31	24.03	121.34

The deviations range from 5% for polonium up to over 100% for Er and Yb. They come from the different spatial discretization of the fluxes and they witness how the actual spectra are relevant to determine the production of certain nuclide species.

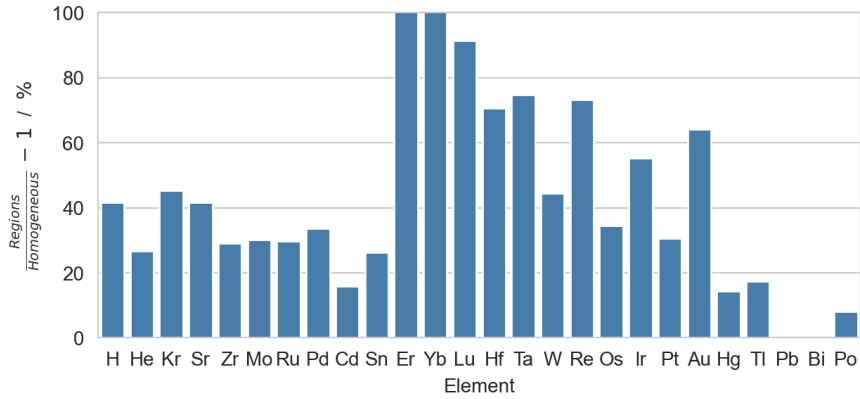


Figure 5.1: Variation of elemental concentrations taking into account or not the separate regions in the STA. The deviations are evaluated at EoI, only the elements with content higher than 10 mg/kg are shown.

5.2 LBE activity in the STA

The LBE activity evolution throughout the reactor lifetime and beyond is presented in Fig. 5.2. The focus is given to the volatile radionuclides, since the activity associated to them is directly proportional to the dose in case of release. For this reason it is particularly important to draw the evolution of the target nuclides both during operation and after the reactor shutdown.

The extensive list of the analyzed nuclides is available in Sect. 1.2. The plot shows

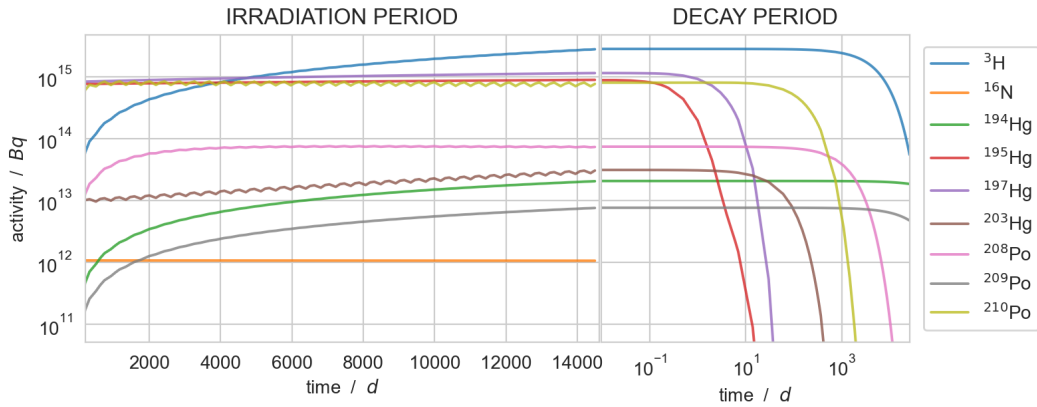


Figure 5.2: Time evolution of the activity of volatile products present in the spallation target assembly during reactor operation and after shutdown.

the outputs of the homogeneous approach. The activity in the LBE is dominated

by ^3H , a volatile nuclide largely generated by spallation reactions. ^3H builds up during operation because of its relatively long half life of about 12 years. During operation the main contributors to the activity are ^{195}Hg , ^{197}Hg and ^{210}Po , each of them providing an activity of around $1e15$ Bq. Their concentration (and activity) is approximately constant during operation. The mercurium isotopes are short lived so they completely decay during the maintenance periods and the same amount is produced in each irradiation cycle.

As regard ^{210}Po , it has a half life of about 140 days that is comparable to a reactor irradiation cycle, therefore the build-up during the cycle is the net balance between production and depletion, being its decay not negligible. The oscillations in its activity are due to the reactor long maintenance periods (90 days), where the concentration decreases more. The other relevant nuclides have an associated activity that is at least one order of magnitude lower than what the previously mentioned nuclides.

5.3 Decay Heat associated to LBE in the STA

The total decay heat is conveyed through α , β and γ radiation. The specific contribution (per unit mass) of each radiation to the decay heat after shut-down is displayed in the top plot of Fig. 5.3. The fractional contribution of the nuclides producing more than 5% of the decay heat is presented in the bottom part of the figure.

The plots show the results of the homogenized approach. With respect to the decay heat produced by the zone-division approach a decay heat underestimation up to 15% is observed in the time scale analysed as shown in Fig. 5.4. The discrepancy reduces from around 12% down to slightly below 0 from the short to the intermediate decay time, when most of the decay heat is provided by ^{210}Po , which is under-produced with the sub-division approach. The deviation increases again in the longer decay time, when most of the decay heat is associated to ^{207}Bi . It has a longer half-life of about 30 years and is present in large amount from the activation of natural bismuth through $(n,2n)$ and $(n,3n)$ reactions in ^{208}Bi and ^{209}Bi , respectively. Investigating the production mechanism and the uncertainty of ^{210}Po is fundamental for safety calculation since it contributes up to 60% of the total decay heat in the LBE.

5.4 Production mechanisms of relevant nuclides in the STA

The investigation of the production mechanisms of relevant nuclides is carried out in this section. The analysis of the reaction rates explains which are the main

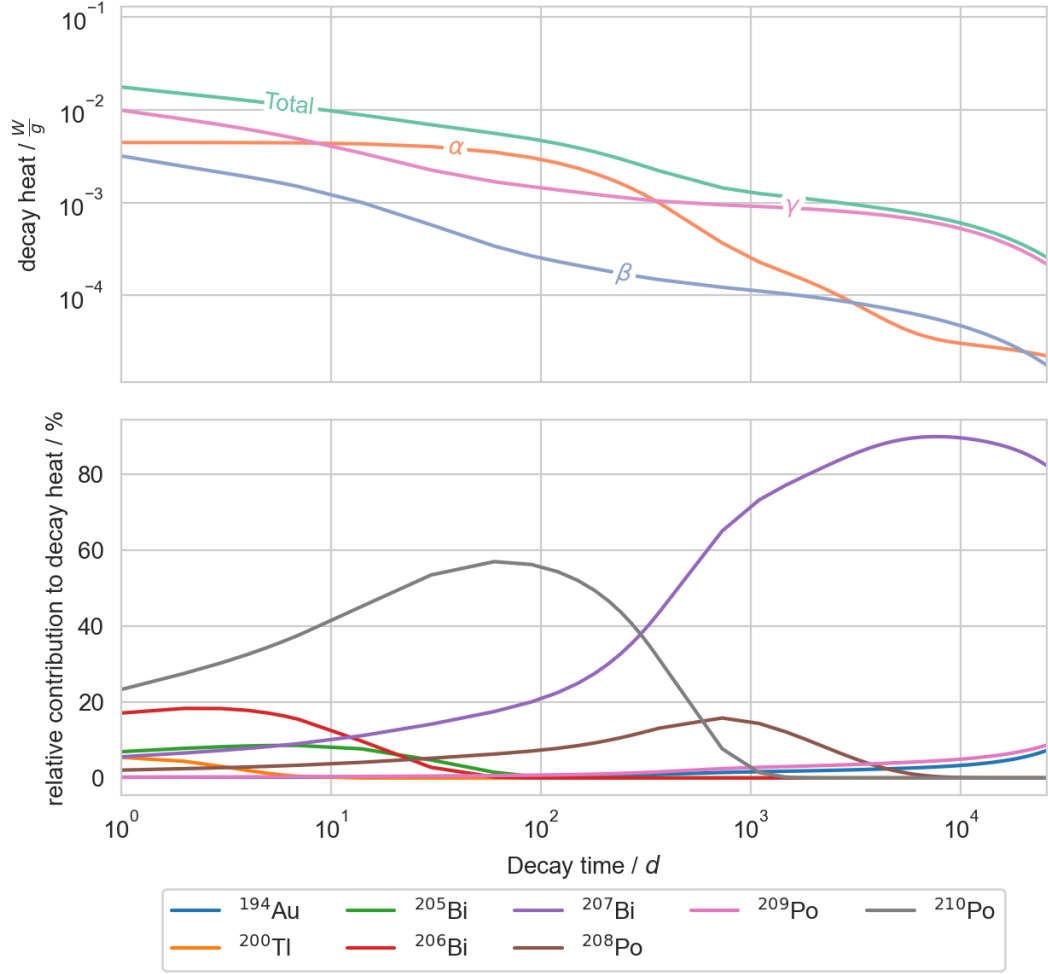


Figure 5.3: Time evolution of the decay heat after shut-down. Contribution of each particle on top and nuclides fractions in the bottom figure.

reaction chains for the production and disappearance of the nuclides of interest. The reaction rate multiplied by the concentration parent nuclide concentration at every instant constitutes the amount produced by that channel, mathematically expressed by eq. (5.1).

$$N_{P \rightarrow D}(t) = \langle \sigma \phi \rangle_{P \rightarrow D} \int_{t_0}^t N_P(t') dt'. \quad (5.1)$$

In the equation above $N_{P \rightarrow D}(t)$ is the amount of the nuclide D (daughter) produced by a certain nuclide P (parent), $\langle \sigma \phi \rangle_{P \rightarrow D}$ is the corresponding reaction rate (assumed time-independent) and N_P is the time-dependent concentration of P . The concentration of the nuclide D at a certain time t is given by the sum of

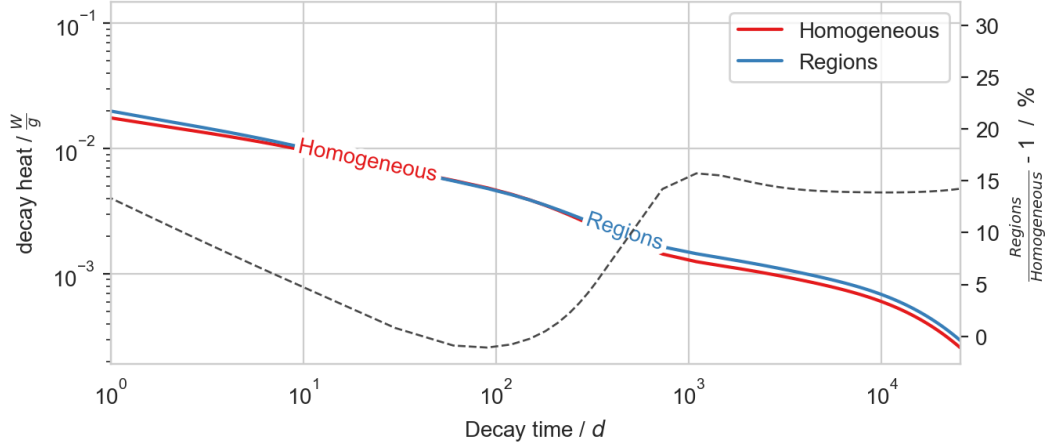


Figure 5.4: Time evolution of the decay heat with/without STA sub-division. The dashed line shows the deviation from the homogeneous case and the corresponding y-scale is on the right.

all contributions from its parent nuclides, to which a disappearance term must be subtracted because of the radioactive decay or the nuclear reactions of D .

Production of ^{210}Po

^{210}Po poses the greatest concern both in terms of LBE activity and decay heat. Its production in the spallation target assembly is mainly driven by the radioactive β -decay of ^{210}Bi ($t_{1/2} = 5$ days). The latter is produced by neutron capture in ^{209}Bi . The second production path is the neutron capture in ^{209}Po and it accounts for the 5% of the total production. This implies that the concentration of ^{210}Po is mainly affected by neutron flux and by the capture cross section of ^{209}Bi . The capture cross section increases in the resonance region below 1 MeV and consequently the production is enhanced if the spectrum is softer. This explains the

Table 5.2: Reaction rates of ^{209}Bi (n, γ) reaction in the spallation target assembly.

		Reaction rate (s^{-1})
$^{209}\text{Bi} \xrightarrow{n, \gamma} ^{210}\text{Bi}$	Homogeneous STA	4.13e-12
	Bottom	1.21e-12
	Center (ST)	1.53e-12
	Top	7.35e-13

overestimation of ^{210}Po in the homogeneous approach where the reaction rate is higher because of an overestimation of the epithermal neutron flux.

The reaction rates of ^{210}Bi production in the regions are reported in Tab. 5.2. The difference in the reaction rate in the homogeneous approach with respect to the sum in the three regions confirms what seen in the plot 5.2, i.e., conservative results are obtained with the homogeneous approach for the production of ^{210}Po .

Production of other polonium isotopes

Compared to the ^{210}Po behaviour the other polonium isotopes show an opposite trend, since they are mainly generated by proton reactions. The relevance of the proton flux is emphasized when treating the spallation region as a separate zone. More than 99% of ^{208}Po and ^{209}Po come from ^{209}Bi that undergoes respectively (p, n) and (p, γ) reactions.

Production of tritium

^3H , that provides largest activity in the STA during operation and after shut down is produced by spallation reactions in lead and bismuth. It decays in ^3He that in turns undergoes (n, p) reactions during reactor operation and it produces other tritium. When ^3H starts to build-up its main production path is self-production by the daughter ^3He .

Production of ^{16}N

^{16}N is almost completely produced by (n, α) reactions in ^{19}F , that is a stable nuclide found as impurity in the fresh LBE. The reaction has a threshold at around 1 MeV so the production would be negligible in case of softer spectrum.

Production of mercury isotopes

Mercury isotopes present in the activated LBE are of major concern in case of release in the environment. They are mainly produced via spallation reactions. They are produced by direct spallation reactions in lead and bismuth, β^+ -decay of thallium isotopes and spallation reactions in other nuclides produced during irradiation. Other production mechanisms are neutron- and proton-induced reactions such as:

- ^{194}Hg produced by $(n, 3n)$ reaction in ^{196}Hg ,
- ^{195}Hg produced by $(n, 2n)$ reaction in ^{196}Hg ,
- ^{197}Hg produced by (n, γ) reaction in ^{196}Hg and $(n, 2n)$ reaction in ^{198}Hg ,
- ^{203}Hg by (n, γ) reaction in ^{202}Hg .

Production of ^{207}Bi

^{207}Bi is important for the LBE decay heat in the long term from 500 d to 70 years of decay. It is mainly produced by neutron-induced reactions and it is depleted by neutron capture and β^+ -decay in the stable ^{207}Pb . The major production paths

are ($n,2n$) reaction in ^{208}Bi and ($n,3n$) reaction in ^{209}Bi . The second mechanism is more relevant at the beginning of irradiation because of the bismuth natural isotopic composition (100% ^{209}Bi) but when ^{208}Bi builds up the two mechanisms have the same relevance.

5.5 LBE activity comparison for the MYRRHA Design Revisions 1.4 and 1.8

In the LBE source term assessment carried out for the MYRRHA Design Revision 1.4 [42] the LBE depletion analysis for the spallation target assembly was performed. This makes it possible to compare the results of this work for the MYRRHA Design Revision 1.8 with the the source term estimates produced in the past.

The differences in the reactor design and in the modelling assumptions are established based on the SCK CEN internal reports [43], [44]. Updates in the core layout were made to fulfill new requirements given in term of target performances. Other differences involve the codes and data employed: the ALEPH version 2.8 was already verified with respect to the version 2.5 in Sect. 4.3. ALEPH2.5 was used to carry out the LBE source term assessment for the MYRRHA Design Revision 1.6 [7], but the work for the MYRRHA Design Revision 1.4 was performed with an older version of the code. Moreover, older releases of both neutron and proton data libraries were used in that work, giving different yields for some of the reactions relevant for the LBE depletion.

Among the core parameters, the most relevant for the comparison are listed in Tab. 5.3. The analysis of the deviations is limited to the nuclides already

Table 5.3: Major differences in the models employed to evaluate the MYRRHA source term. Discrepancies come from design differences and modelling assumptions. Volumes and neutron fluxes are given for the spallation target assembly.

	LBE volume (cm ³)	Neutron flux (n/(cm ² s))	Proton beam current (mA)
v1.8 (this work)	1.648e+04	1.1054e+15	4.00
v1.4 (past calculation)	1.479e+04	1.6025e+15	2.45

under investigation and the relative deviations are summarized in Tab. 5.4. The increase in the proton flux due to larger proton current can explain the increase in the production of spallation products like the mercury isotopes. Tritium shows an opposite trend, even if it is a spallation product it is underestimated in the new evaluation. This can be due to updates in nuclear data libraries. The

Table 5.4: Activity concentrations of relevant nuclides in the LBE in the spallation target assembly obtained in the past work for the MYRRHA Design Revision 1.4 and in this work for the MYRRHA Design Revision 1.8.

	New model	v1.4 calculation	Δ %
^3H	1.71e+11	1.99e+11	-16.9
^{194}Hg	1.26e+09	7.62e+08	39.3
^{197}Hg	6.97e+10	3.52e+10	49.4
^{207}Bi	3.80e+10	3.17e+10	16.7
^{210}Bi	6.43e+10	5.46e+10	15.1
^{208}Po	4.51e+09	2.62e+09	41.9
^{209}Po	4.65e+08	5.01e+08	-7.79
^{210}Po	4.86e+10	4.39e+10	9.79

reference neutron data library remains JEFF-3.1.2 but an improved algorithm was implemented to construct smooth reaction rates from the XS from different NDL such as JEFF-3.1.3 up to 20 MeV, TENDL-2013 to cover energy range 20-200 MeV and data above 200 MeV from HEAD-2009 high-energy activation library. In addition the latest release of TENDL library [7], replacing the older one was used in the new evaluation. The production of ^{210}Po increases of about 10% with respect to the past calculations. The increase is due to an increase of captures in ^{209}Bi .

5.6 Comparison of neutron data libraries

This section investigates the differences emerging when changing the neutron data libraries. All other parameters of the depletion model are kept identical, including the high-energy neutron data above 20 MeV (taken from TENDL), the proton data and the proton spallation model. The libraries used are those introduced in Sect. 2.4.5. The outcomes are shown in term of deviation with respect to the concentrations obtained with the reference library, that is, JEFF-3.1.2. The relative deviations are reported in Fig. 5.5.

Excellent agreement is shown for ^{208}Po and ^{209}Po . This behaviour was expected since most of the production in the spallation target assembly comes from proton reactions.

^{16}N is produced by (n, α) reaction in ^{19}F . The corresponding cross section has a higher threshold and it is slightly lower in the range 10-20 MeV in JENDL-4.0u. This partially explains the 5% underestimation.

^3H is produced both from neutron and proton induced reactions in lead and

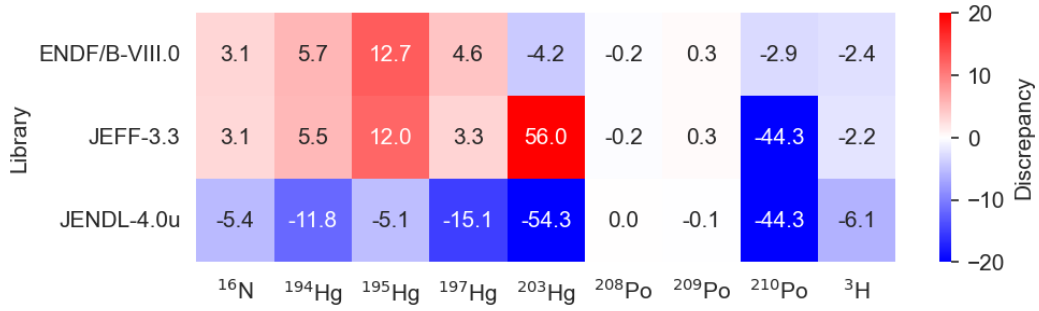


Figure 5.5: EoI concentrations of relevant nuclides obtained with different neutron NDL. The outcomes are compared to the reference library: JEFF-3.1.2

bismuth. Compared to JEFF-3.1.2, all other nuclear data libraries result in a lower prediction by maximum 6%.

The mercury isotopes show a common trend. The production of ^{194}Hg , ^{195}Hg and ^{197}Hg is overestimated by JEFF-3.3 and ENDF/B-VIII.0 and underestimated by JENDL-4.0u, with respect to JEFF-3.1.2. Part of their production comes from ^{196}Hg and a different buildup of this nuclide can be the reason of the discrepancies. The deviation of ^{203}Hg is the largest among the mercury isotopes. Completely different estimations are produced when using JEFF-3.3 and JENDL-4.0u, respectively overestimating and underestimating by 55% the concentration of the nuclide. The underestimation by JENDL-4.0u is common to all Hg nuclides and it is emphasized in this case. The overestimation by JEFF-3.3 can be partially explained looking at the different evaluation of ^{202}Hg (n, γ) cross section with respect to the previous version, presented in Fig. 5.6. A resonance region appears below 0.1 MeV and a high energy tail between 5 and 20 MeV is added. The underestimation observed in JENDL-4.0u is not related of the capture cross section of ^{202}Hg , that shows the same evaluation in JEFF-3.1.2 and JENDL-4.0u. The discrepancy between the concentrations obtained with the two library partly comes from a different estimation of the concentration of ^{202}Hg , whose reason was not investigated. The deviation in the concentration of ^{203}Hg is not fully understood and therefore a deeper analysis must be performed.

The different estimation of ^{210}Po is due to two different evaluations. JEFF-3.1.2 is in agreement with ENDF/B-VIII.0 while JEFF-3.3 shows the same deviation of JENDL, providing an underestimation of about 44%. The problem lies in the evaluated cross sections of ^{209}Bi and it is fully discussed in [45].

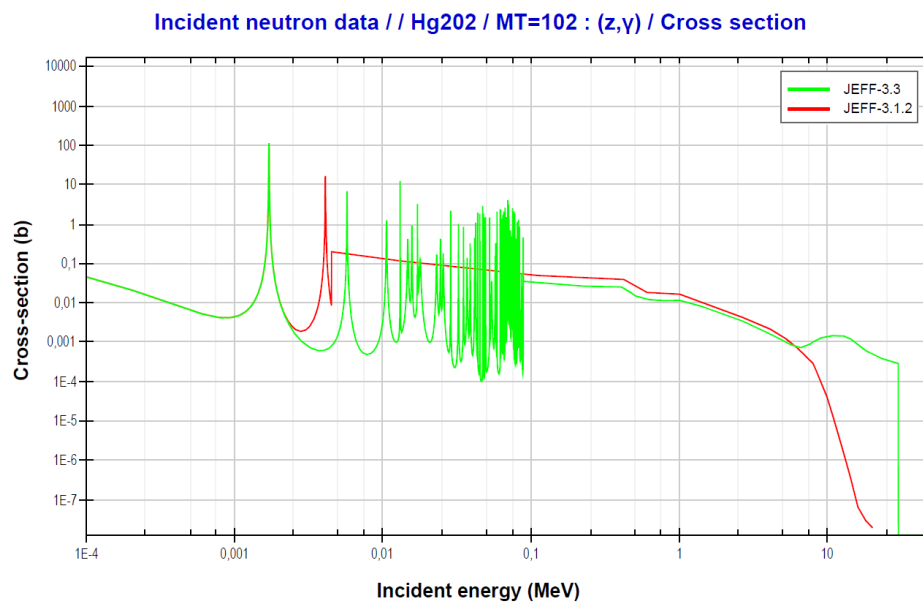


Figure 5.6: ^{202}Hg (n, γ) cross section data: absolute values for JEFF-3.1.2 and JEFF-3.3.

Chapter 6

Fuel source term - Equilibrium core model

The output of the equilibrium model, briefly discussed in Sect. 3.2, is the nuclide inventory of the irradiated nuclear fuel contained in every FA (or FA batch) loaded in the core. The nuclide concentrations are homogenized over the fuel volume of each FA batch, as shown in eq. (6.1) and no spatial gradient internal to the FA is considered.

$$N_{i,batch}(t) = \frac{1}{V} \int_V d\vec{r} N_{i,batch}(\vec{r}, t) \quad (6.1)$$

The nuclide concentration in a FA of the equilibrium core is fed to a radioactive decay model to simulate the time evolution of the radionuclide inventory once the FA is unloaded from the core.

According to the normal operation strategy, FAs are discharged from the core after a fixed number of irradiation cycles that depends on the considered reactor operation mode (critical or sub-critical) and that corresponds to a fixed pre-calculated burnup level as discussed in [46]. The burnup level at discharge is around 55.1 and 47.0 MWd/kg in the critical and sub-critical configuration, respectively. The burnup lever in the critical mode is higher because of the larger number of irradiation cycles, 18 with respect to 13 in sub-critical. Discharged FAs are temporarily stored in the In-Vessel Fuel Storage (IVFS) in the reactor pool for further cooling before being extracted from the reactor. Predictions of the residual decay heat load and activity of a discharged FA act as a boundary condition to optimize the FA extraction process.

In this work we investigate the possibility that partly-irradiated FAs — i.e., FAs with an average burnup that is lower than the pre-calculated average discharge burnup — located in the IVFS are extracted from the reactor. Because of the MYRRHA IN-to-OUT in-core FA shuffling strategy, FAs with a lower burnup level generally experience higher neutron fluxes in the irradiation cycles prior to being

moved to the IVFS. This condition is generally associated to a larger amount of short-lived fission products and actinides that significantly affect the FA decay heat and activity in the short term.

Given that the characterization of the FA source term — activity and decay heat — for any possible burnup level and irradiation option is unrealistic, in this work we computed the source term derived quantities for each FA in the equilibrium core at EoC, as if they were immediately unloaded into the IVFS and later on extracted from the reactor. The analyzed decay period extends to 70 years after discharge.

The governing depletion equation of this study is the exponential radioactive decay law since no irradiation is involved (the irradiation was simulated to derive the equilibrium core). The system is described by the Bateman equations and it is shown in eq. (6.2):

$$\frac{dN_i(t)}{dt} = -\lambda_i N_i(t) + \sum_j \lambda_{j \rightarrow i} N_j(t) \quad (6.2)$$

where N_i is the concentration of the nuclide i , depleted because of its own radioactive decay governed by the decay constant λ_i and produced by decay of the other atomic species whose concentration is N_j and decay constant $\lambda_{j \rightarrow i}$. An example of relevant nuclides in the case study involves ^{241}Pu ($t_{\frac{1}{2}} = 14.33$ y) and ^{241}Am ($t_{\frac{1}{2}} = 432.81$ y). The latter comes from the β^- decay of plutonium 241, that is not produced during decay unless in negligible amount by decay of ^{245}Cm ($t_{\frac{1}{2}} = 8.25 \times 10^3$ y). This is important because ^{241}Am is the greatest contributor to the decay heat of a FA at 70 years of cooling. The equations governing the ^{241}Pu - ^{241}Am evolution are reported in eq. (6.3).

$$\begin{aligned} N_{Pu1}(t) &= N_{Pu1}(0)e^{-\lambda_{Pu1}t} \\ N_{Am1}(t) &= N_{Pu1}(0) \frac{\lambda_{Pu1}}{\lambda_{Am1} - \lambda_{Pu1}} e^{-\lambda_{Pu1}t} \end{aligned} \quad (6.3)$$

N_{Pu1} and N_{Am1} are the concentrations of ^{241}Pu and ^{241}Am while λ_{Pu1} and λ_{Am1} are the corresponding decay constants. Rather than to nuclide concentrations, the main focus of this chapter moves to the decay heat and to the activity of the FAs after the unloading. Knowing the nuclide inventory, both quantities can be by eqs. (2.10).

6.1 Nuclide concentrations

The time-evolution of the nuclide inventory of irradiated fuel is modeled taking the EoC concentrations of each FA, in both the critical and sub-critical configurations, as initial conditions of the Bateman equations. The nuclides buildup is reported as a function of the burnup level of a FA. Analysing the buildup of the various atomic

species certain common patterns emerge. In the following the investigated nuclides are grouped as actinides and fission products.

Actinides buildup

Generally, the actinides have a similar buildup in the critical and sub-critical configurations. The buildup of some nuclides is maximized in the sub-critical case: for instance ^{242}Cm ($t_{\frac{1}{2}} = 162.93$ y) and ^{243}Cm ($t_{\frac{1}{2}} = 28.90$ y) have a final concentration 135% larger than in the critical case.

The plutonium isotopes show different trends. The production of ^{238}Pu ($t_{\frac{1}{2}} = 87.70$ y) is maximized in the sub-critical configuration as a result of overproduction of its parent nuclide ^{242}Cm . Conversely the concentration of ^{239}Pu ($t_{\frac{1}{2}} = 24129.50$ y) is lower in the sub-critical core, indicating a higher burn rate in this configuration due to the larger neutron flux.

The larger production of ^{241}Am and ^{242m}Am ($t_{\frac{1}{2}} = 141.00$ y) in the sub-critical mode is not explained by the ^{241}Pu buildup, since the latter is under-produced in the sub-critical configuration. Concerning ^{242m}Am , its neutron capture is lower in the harder spectrum of the sub-critical core, which results in a larger ^{242m}Am buildup and a lower production of ^{243}Am ($t_{\frac{1}{2}} = 7364.98$ y).

Tab. 6.1 compares the actinide concentrations of the most irradiated FA (that with the largest burnup) for the End of Cycle (EoC) configurations of the critical and sub-critical cores. The comparison is carried out on FAs that reached the discharge burnup, higher in the critical configuration. Under the equilibrium assumption, the irradiation condition of a fuel assembly with largest burnup level, placed in the core periphery corresponds to the condition of a FA loaded in the core after it has undergone the whole in-core reshuffling procedure. Therefore the composition in the fuel assembly with highest burnup level is equal to the composition of a FA at End of Irradiation (EoI), before being unloaded from the core.

Table 6.1: EoI concentration (FA with largest burnup) ratio between sub-critical end critical mode for selected actinides.

Nuclide	^{238}Pu	^{239}Pu	^{240}Pu	^{241}Pu	^{241}Am	^{242m}Am	^{242}Cm	^{244}Cm	^{246}Cm
Buildup	1.03	0.96	1	0.94	1.08	1.15	1.36	0.88	0.82

Fission products buildup

The fission products considered in this chapter are those reported in Sect. 1.2.1 and they are split into two categories depending on how their concentration builds up, as shown in Fig. 6.1 for the sub-critical configuration. For the sake of comparison, the nuclide concentration buildup curves are normalized to the corresponding nuclide concentration at EoC for the critical core.

The first category of fission products includes all the considered nuclides with

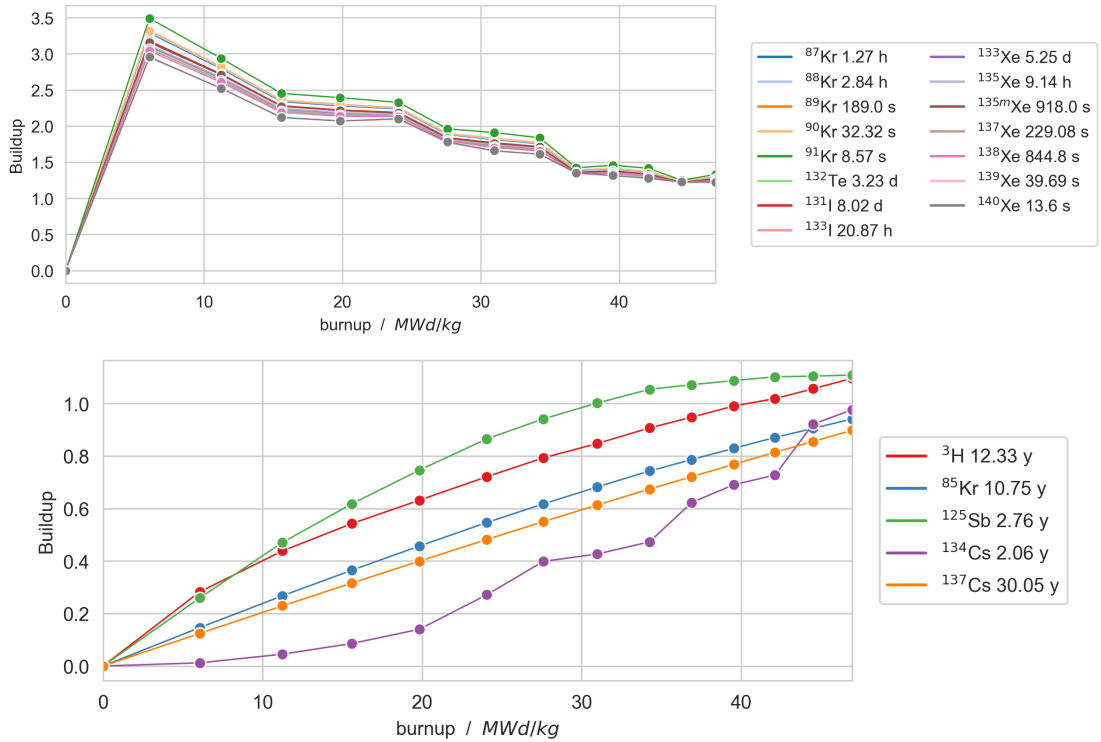


Figure 6.1: Buildup of volatile fission products in sub-critical configuration, divided in two categories depending to their evolution. Normalized on the EoC concentration in critical configuration.

relatively short half-life. The buildup of these nuclides is driven by the cycle power, and it reaches its maximum in the first irradiation cycle — e.g., when the FA is in the core center. Because of the IN-to-OUT in-core FA shuffling scheme, the concentrations of these nuclides decrease as the FA moves away from the core center and the FA power decreases. The sub-critical configuration yields higher peak concentrations for these nuclides because of the larger power generate in the central FAs compared to the critical core.

The second category of fission products includes the relatively long-lived nuclides. The concentration buildup of these nuclides is proportional to the FA burnup and it attains its maximum at EoI. These nuclides show different behaviour and evolution depending on the specific production path.

Because of its long half-life and its negligible capture cross section, ^{137}Cs ($t_{1/2} = 30.05$ y) has a linear dependence on burnup. Because of this, it builds up more in the critical configuration where higher discharge burnup are achieved at EoI.

^3H ($t_{\frac{1}{2}} = 12.34$ y) and ^{85}Kr ($t_{\frac{1}{2}} = 10.76$ y) show a similar evolution but the slope tends to decrease since they slightly decay while building up. This behaviour is emphasized in ^{125}Sb ($t_{\frac{1}{2}} = 2.76$ y). ^3H production in sub-critical mode is enhanced. During the irradiation cycle in the core central position its production is greater in sub-critical configuration. The threshold reactions above 20 MeV become important, in particular ^3H is largely produced from the oxygen contained in the MOX fuel. The mechanism is not relevant when the FA is irradiated further for the center since the high energy tail of the spectrum is negligible. Further discussion on this is presented in appendix A.1.

The non-linear evolution of ^{134}Cs ($t_{\frac{1}{2}} = 2.07$ y) is explained by the fact that it is not a direct fission product but it is produced by neutron capture in ^{133}Cs (stable nuclide), the end product of A=133 isobaric β^- decay chain.

^{127m}Te ($t_{\frac{1}{2}} = 106.1$ d) is the only one among the identified volatile nuclides that is not shown in the plots. It mostly comes from fission and β_- decay of ^{127}Sb ($t_{\frac{1}{2}} = 3.85$ d) and it reaches the peak buildup during the third irradiation cycle.

The indication on the maximum buildup of each radionuclide can be employed in a safety evaluation to obtain conservative results when evaluating the concentration and the associated dose in case of release during accidental sequences.

The volatile nuclides generated in irradiated MOX fuel and that are considered relevant for a safety assessment can be divided into two categories depending on their half-life. Short-lived nuclides reach their peak concentration in the first irradiation cycle, when the FA generates a larger power. For the same reason we observed that they are produced in larger quantities in the sub-critical mode rather than in the critical one. Long-lived nuclides build up during irradiation and they reach their peak concentration at EoI. Their concentration is proportional to the FA burnup. At discharge, the FA burnup is higher in the critical configuration.

6.2 Activity of an irradiated MYRRHA FA

The activity of a FA as a function of the decay time is evaluated from its source term as described in eq. (2.10).

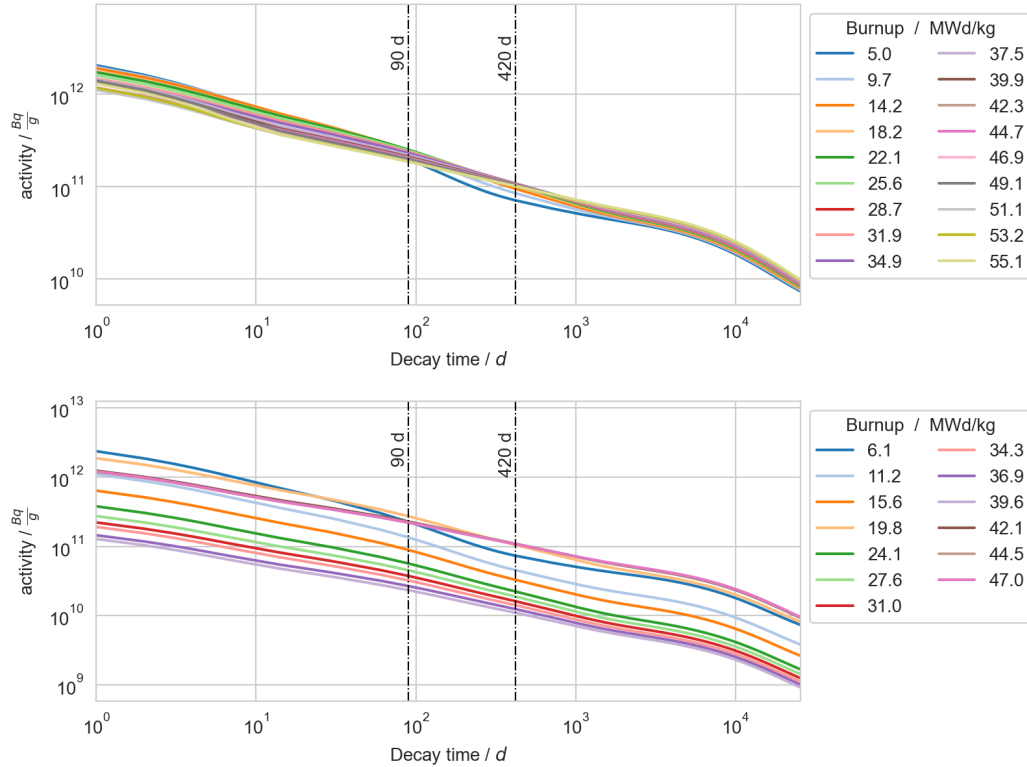


Figure 6.2: FA activity as a function of discharge burnup and decay time. Critical configuration in the top figure, sub-critical in the bottom.

As already discussed, this work has the objective to investigate all the possible discharge situations of an irradiated FA. The evolution of the FA activity for 70 years of decay in critical and sub-critical configuration is drawn in Fig. 6.2.

Envelope activity

The envelope activity is determined considering the FA conveying the largest activity in every step of the decay. Fig. 6.3 shows the evolution of the envelope curve and the associated FA burnup. The curve describes the sub-critical configuration — i.e., the operation mode that gives the larger activity. The FA activity for the critical case is omitted since the same considerations can be drawn. In the first period of decay the activity is dominated by the assembly with lower burnup, that underwent only one irradiation cycle but at the highest power in the central core position. On the contrary the most irradiated assemblies (largest burnup) contribute the most in the long term.

Contributors to envelope activity

The activity in the short period is dominated by short-lived fission products, while

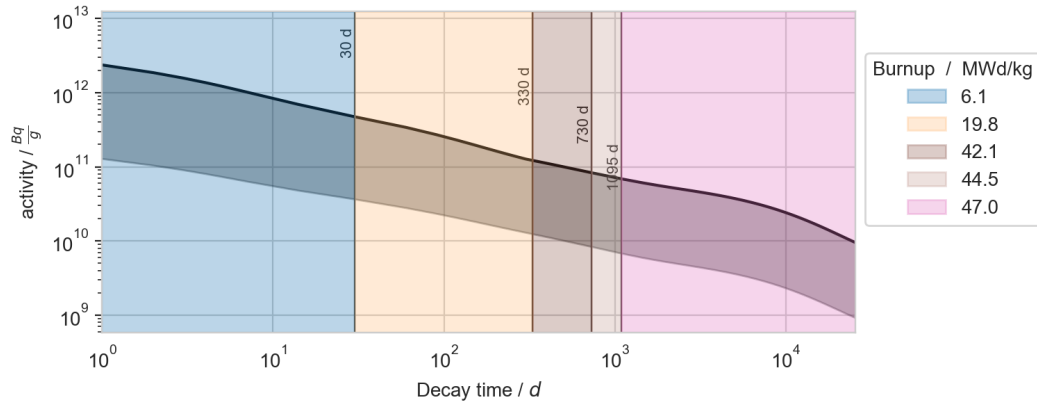


Figure 6.3: Evolution of envelope activity in sub-critical configuration.

at longer decay times it is dominated by ^{241}Pu . The longer the cooling time the more the effects of burnup are important. The FA with the largest burnup is responsible for the envelope curve for decay times greater than three years, when the most of the activity is produced by the actinides. This behaviour is underlined in Fig. 6.4, showing the contribution of fission products and actinides to the FA envelope activity curve.

The figure shows the nuclides contributing for more than 5% to the envelope

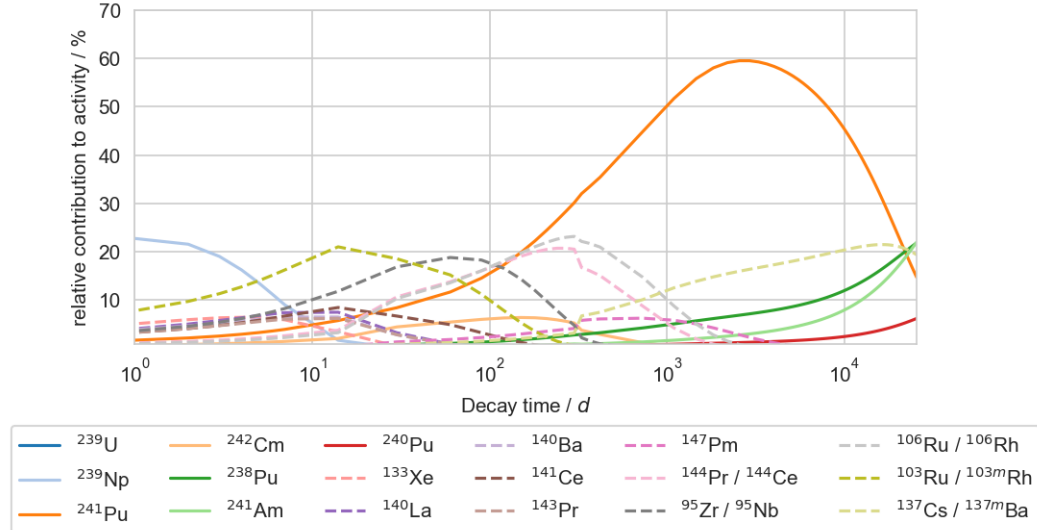


Figure 6.4: Fractional evolution of major contributors to the envelope activity. The actinides are drawn with solid line while the fission products with dashed.

activity in the period ranging from 1 to 70 days of decay. Some fission products

are in a secular equilibrium [47], that is, one parent nuclide with a relatively long half-life decays in a very short-lived daughter nuclide. In this case such nuclides are considered together as a source of activity (and decay heat). The decay chain ^{95}Zr ($t_{\frac{1}{2}} = 64.03$ d) / ^{95}Nb ($t_{\frac{1}{2}} = 34.99$ d) gives the largest activity contribution at 90 days of decay. At more than 100 d the dominant contribution comes from ^{241}Pu . It decays in ^{241}Am than takes over after 70 years of decay. For longer time periods most of the activity is associated to americium and plutonium isotopes. The same approach employed to present the activity of a MYRRHA FA is also adopted in the next section to show the decay heat results.

The time evolution of the activity of a MYRRHA FA was parametrically quantified as a function of the FA burnup to produce an envelope activity curve. In the short term the FAs with low burnup provide the largest activity because of the abundance of short-lived fission products. For longer time scales the FAs with high burnup produce the largest activity because of ^{241}Pu . FAs with intermediate burnup values make up the envelope activity curve in the decay range 30-1000 days.

6.3 Decay heat of an irradiated MYRRHA FA

The time evolution of the decay heat in a MYRRHA FA for the critical and sub-critical reactor operation is displayed in Fig. 6.5.

Envelope decay heat

The main focus both from the safety point of view and the dimensioning of components is to draw an envelope decay heat curve that provides the largest value of decay heat as function of decay time. The envelope decay heat curve in the sub-critical case is shown in Fig. 6.6, following the considerations in Sect. 6.2. For short decay times, FAs with low burnup — irradiated at high power — release the largest decay heat because of great amount of short-lived nuclides. In the mid-term, from 14 days to 2 years, FAs with a intermediate burnup levels provide the largest decay heat. At longer time scales the FAs with the largest burnup and minor actinide concentrations produce the largest decay heat.

Decay heat associated to particle emission

The decay heat is produced by α , β and γ -particles emitted as a part of the decay process of the nuclides that form the radioactive inventory of a FA. The envelope FA decay heat curve was sub-divided according to the responsible decay process and it is presented in Fig. 6.7. The majority of the fission products β -decays and generates unstable nuclei that stabilize by the emitting gamma radiation.

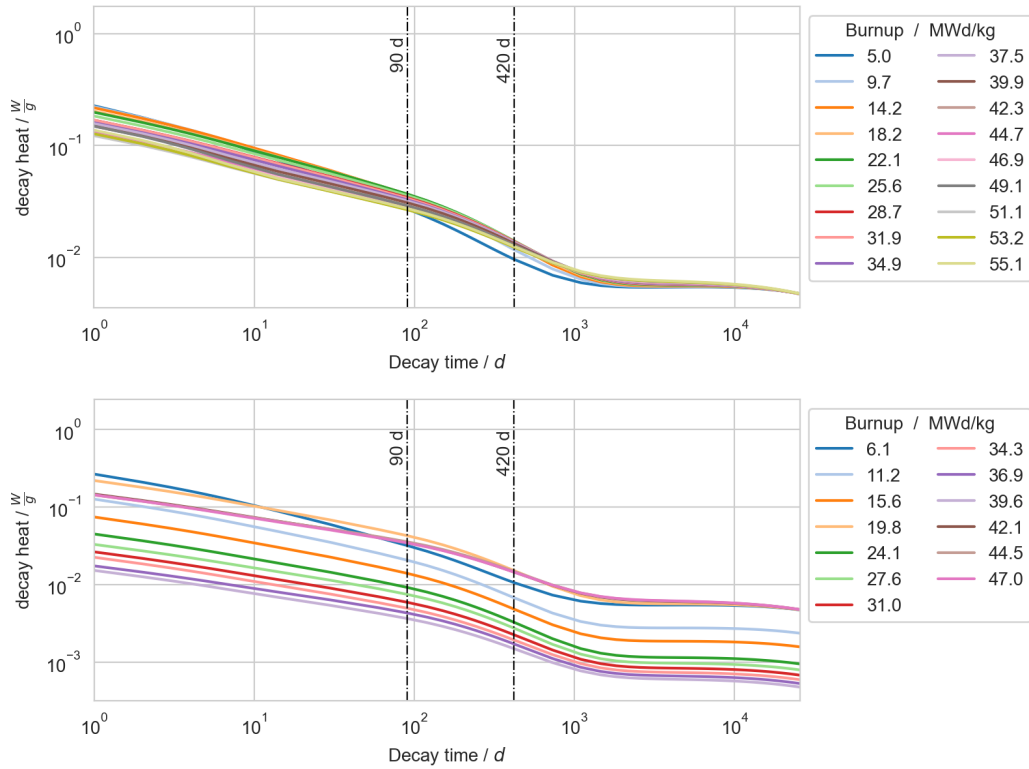


Figure 6.5: Fuel assembly decay heat rate as function of FA burnup and decay time. Critical configuration in the top figure, sub-critical in the bottom.

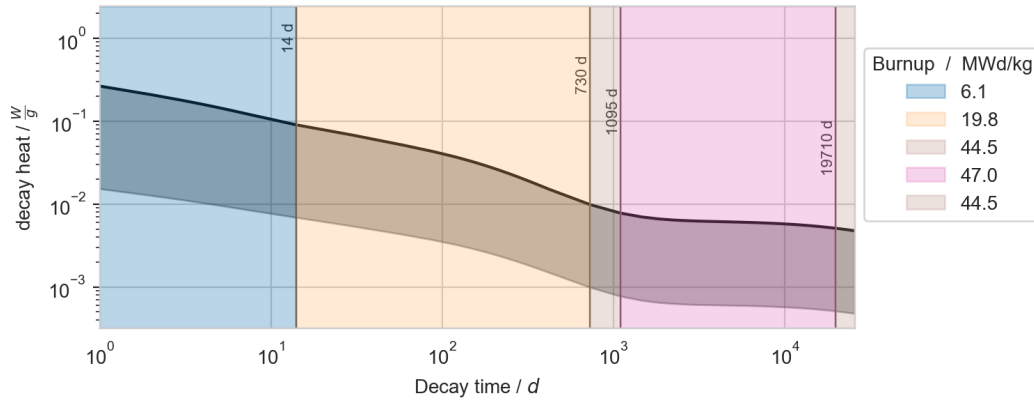


Figure 6.6: Evolution of envelope decay heat curve in sub-critical configuration.

This decay path is the most relevant in the first several days of decay, with an even apportioning of the decay heat between β and γ radiation. The decay chain

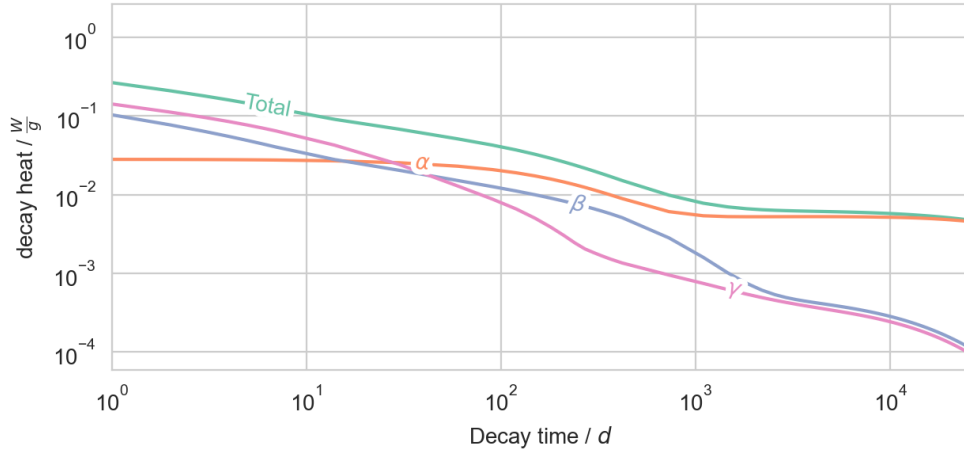


Figure 6.7: Decay heat envelope curve associated to particle emission. The sub-critical configuration is taken into account.

$^{137}\text{Cs}/^{137m}\text{Ba}$ is an example, where the β^- decay of ^{137}Cs is rapidly followed by the emission of a γ -ray from ^{137m}Ba ($t_{1/2} = 2.55$ min). α -particles dominate the decay heat at longer decay time because of the major α -emitters ^{238}Pu and ^{241}Am .

Decay heat contributors

All the nuclides that contribute for at least 5% to the FA decay heat at any decay time are reported in Fig. 6.8.

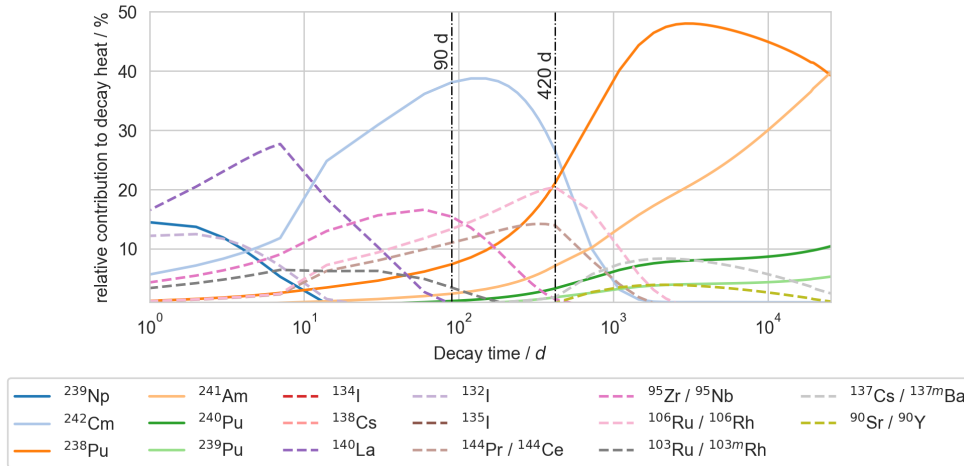


Figure 6.8: Fractional evolution of major contributors to the envelope decay heat. Actinides are plotted with solid line while fission products with dashed.

The dashed and solid lines are used to distinguish fission products and actinides. In the short term the FA decay heat is dominated by short-lived fission products and by ^{239}Np ($t_{\frac{1}{2}} = 2.356$ d). The major contributor between 1 and 10 days of decay is ^{140}La ($t_{\frac{1}{2}} = 1.678$ d). ^{132}I ($t_{\frac{1}{2}} = 2.295$ hr), ^{242}Cm , ^{95}Zr and its daughter ^{95}Nb also contribute more than 10% in this interval of time.

^{242}Cm and the decay chain $^{95}\text{Zr}/^{95}\text{Nb}$ gain importance at intermediate decay times and they are the major contributors to decay heat at 90 days of decay. Also, a non negligible contribution comes from the decay chain $^{106}\text{Rh}/^{106}\text{Ru}$ ($t_{\frac{1}{2}} = 2.2$ hr, $t_{\frac{1}{2}} = 1.017$ years) and by ^{135}I ($t_{\frac{1}{2}} = 6.58$ hr). At 90 days decay heat coming from actinides has the same magnitude of that generated by FPs and its relevance increases going further.

After 420 days of decay the relative decay heat contribution of ^{242}Cm reduces from 40 to 25% even if it still conveys the largest decay heat. At this point the α -decay of ^{238}Pu starts to be relevant. Together with ^{241}Am , ^{238}Pu is the largest contributor up to at least 70 years of decay. The fission products decay heat is less relevant in the longer decay period. A contribution between 5 and 10% comes from the decay chains ^{90}Sr ($t_{\frac{1}{2}} = 28.80$ y) / ^{90}Y ($t_{\frac{1}{2}} = 2.67$ d) and in particular $^{137}\text{Cs}/^{137m}\text{Ba}$. The four main contributors to the MYRRHA FA decay heat at 70 years of decay are α -emitters: $^{238,239,240}\text{Pu}$ and ^{241}Am .

The time evolution of the decay heat of a MYRRHA FA was parametrically quantified as a function of the FA burnup to produce an envelope decay heat curve. In the short term the FAs with low burnup provide the largest decay heat because of the abundance of the β, γ -decay of short-lived fission products. For longer time scales the FAs with high burnup produce the largest decay heat mostly because α -emitters ^{238}Pu and ^{241}Am . FAs with intermediate burnup values make up the envelope activity curve in the decay range 30-1000 days.

The investigation of nuclear data uncertainty to the total decay heat is one of the objectives of this work. Fig. 6.8 shows the nuclides that play a role and of which concentrations it is important to quantify the uncertainty. This exercise is described in detail in 8.

6.4 Production mechanisms for the nuclides relevant for the source term of the MYRRHA FA

In this sections the production paths of the nuclides relevant for the analysis of the source term of a MYRRHA FA are described. The nuclides taken into account

belong to three categories:

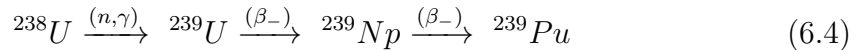
- volatile fission products important in case of accidental release;
- nuclides contributing to the decay heat in the FA after;
- plutonium isotopes and minor actinides relevant for the spent fuel management.

The production mechanisms are investigated by a thorough analysis of the the reaction rates involved in the depletion process. A limit of this study is that only the critical operation mode is analysed, and that all the nuclear reactions for neutrons with energies above 20 MeV are not taken into account. This assumption is deemed to be acceptable for the analysis of the fuel source term. An insight of the difference in the production mechanisms present in the critical and sub-critical mode of operation is presented in appendix A.1 for specific nuclides (3H).

The considered volatile nuclides are produced mainly by fission either as direct fission products or as indirect fission products following the isobaric decay process. 3H is produced by ternary fission. Their production via neutron capture is generally negligible.

The outlier of this category is ^{134}Cs , which results from neutron capture in ^{133}Cs . The same conclusion can be drawn for the fission products relevant for decay heat, with their production being mainly linked to the fission of plutonium isotopes.

Minor actinides appear from the neutron-induced transmutation of the uranium and plutonium isotopes contained in the fresh MOX. The MOX fuel considered for MYRRHA is made by 30% of plutonium, which drives the nuclear fission chain with isotopes ^{239}Pu and ^{241}Pu . In parallel, plutonium is bred and depleted through neutron capture reactions. The buildup of plutonium isotopes is shown in the first plot of Fig. 6.9. The most depleted isotope of plutonium is ^{241}Pu since its participates to fissions and its production mechanism is less effective than for ^{239}Pu since more neutron captures are necessary. ^{238}U is the most abundant nuclide in the fresh fuel and a continuous source of ^{239}Pu via neutron capture. The reaction chain is shown in eq. 6.4.



Minor actinides are concerning for SNF management. ^{241}Am is the main contributor to decay heat at 70 years of cooling because of its half-life. It is produced by ^{241}Pu β_- decay both during irradiation and after discharge of the fuel assembly. Additional neutron captures in ^{241}Am lead to the production of other minor actinides such as ^{242}Cm , as shown in eq. (6.5).



^{242}Cm ($t_{\frac{1}{2}} = 163$ d) is important for the FA decay heat following the considerations in Sect. refcoreDH. It is produced by the radioactive decay of ^{242m}Am and, because of its half-life, it reaches its peak concentration at intermediate burnup levels, i.e., before the FA discharge. Its irregular buildup curve is to be associated by its decay constant.

^{243}Cm is produced by neutron capture in ^{242}Cm , while only a small amount of ^{244}Cm ($t_{\frac{1}{2}} = 18.00$ y) follows this chain. The ^{244}Cm dominant production path is from the β -decay of ^{244}Am ($t_{\frac{1}{2}} = 10.1$ hr), generated by successive captures in ^{242m}Am . Heavier curium isotopes are produced through neutron capture in ^{244}Cm with a strong non-linear dependence on burnup.

^{243}Cm and ^{245}Cm ($t_{\frac{1}{2}} = 8255.49$ y) have larger (non-threshold) fission cross sections compared to other curium isotopes, and they can also fission spontaneously. However, because of their tiny concentration in the nuclear fuel their major depletion mechanism is α decay.

The nuclides relevant for the source term of the MYRRHA FA were divided into three categories. Volatile fission products, as well as fission products important for the decay heat are directly produced by fission.

The minor actinides that pose a burden for the spent fuel management are generated from the nuclear transmutation of the plutonium driver fuel.

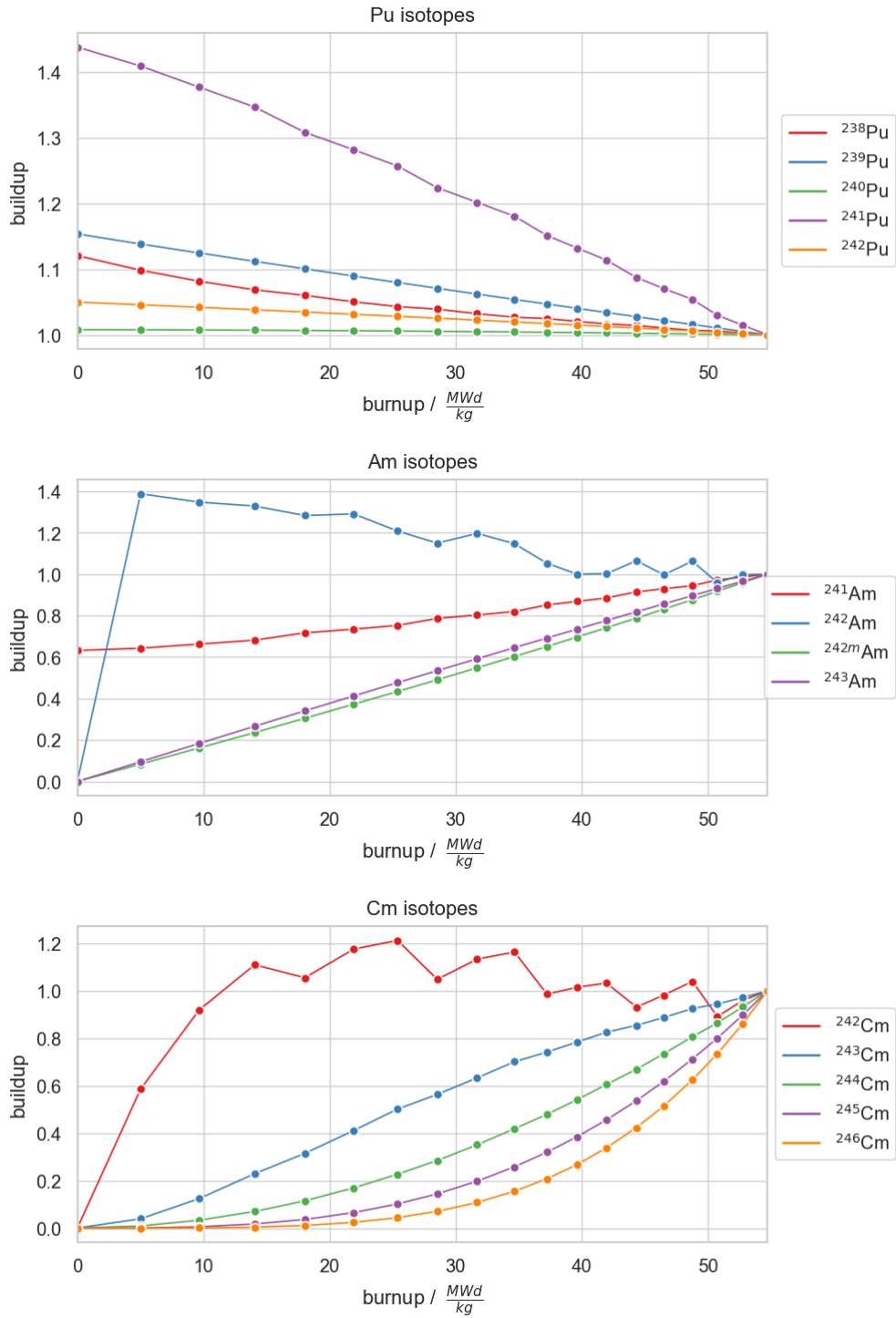


Figure 6.9: Buildup of actinides during irradiation, normalized on the EoI concentration.

Chapter 7

Model simplification - From a 3D core model to a 2D fuel assembly model

In this chapter the concept of a Fuel Assembly (FA) model is introduced. The development of such a simplified model to simulate the depletion of the MYRRHA fuel comes from the necessity to perform a number of analyses that would demand too many resources for a full core simulation. The main purpose of this work was to produce a model that:

- has a low computational cost;
- it is flexible;
- it mimics as much as possible the behaviour of the 3D core model for what concerns the FA source term.

Even without providing highly accurate best-estimate results, this low-fidelity surrogate model shall be suitable to perform the uncertainty quantification studies that are deemed unfeasible for a full core model. The same approach was used in [48] for an uncertainty analysis in a depletion model of the MYRRHA Design Revision 1.6. This methodology is also widely used for the characterization of spent nuclear fuel (SNF) of traditional LWR reactors [49].

Given the selected approach to propagate uncertainties on input parameters — i.e., statistical sampling — the nuclide vector uncertainty quantification would be too time consuming using a full core model. The propagated uncertainties come from the nuclear data and they are used to provide confidence intervals for safety related parameters and to drive design choices.

A second analysis is carried out to estimate the impact of some of the model assumptions that led to the FA model. In particular, the focus was on assessing how the axial power and burnup profiles in the FA affect neutronic parameters and the depleted nuclide inventory. For this purpose both 2D and 3D FA models were developed.

The inputs of the FA models were taken from the results of the full core depletion simulation in critical mode. The sub-critical configuration was not investigated for the evident difficulties in representing the external proton source. This must be considered drawing the conclusions since, as already shown by the results in the previous chapter, the sub-critical configuration provides the worst scenario both for the FA activity and decay heat.

In total, four depletion models were developed in this work to study the MYRRHA fuel source term:

- the 3D full core models (at equilibrium) for the critical and sub-critical reaction operation: they were used to determine the buildup of volatile nuclides during irradiation and the FA activity and decay heat envelope curves.
- a 2D FA model: it was used to propagate the uncertainty of nuclear data.
- a 3D FA model: it was used as a reference to investigate the impact on the nuclide vector of considering an axial flux, power and burnup profile.
- a 3D FA model with axial depletion zones: it was used as a reference to investigate the impact on the nuclide vector of considering an axial flux, power and burnup profile. All the FA models are developed in Serpent [27].

7.1 Fuel assembly models description

The model of the fuel assembly consists of the hexagonal lattice of fuel pins encased in the steel wrapper and cooled by LBE. Each fuel pin contains the MOX fuel and the steel cladding and the gap of neutron gas. A schematic view of the simulated FA is shown in Fig. 7.1.

2D FA model

The 2D FA model makes use of reflective boundary conditions in all directions assuming to model the FA as an infinite system. In the radial direction the assumption implies that the fuel assembly is completely surrounded by other FAs and therefore there is no neutron leakage since the neutrons crossing the boundary re-enter the system.

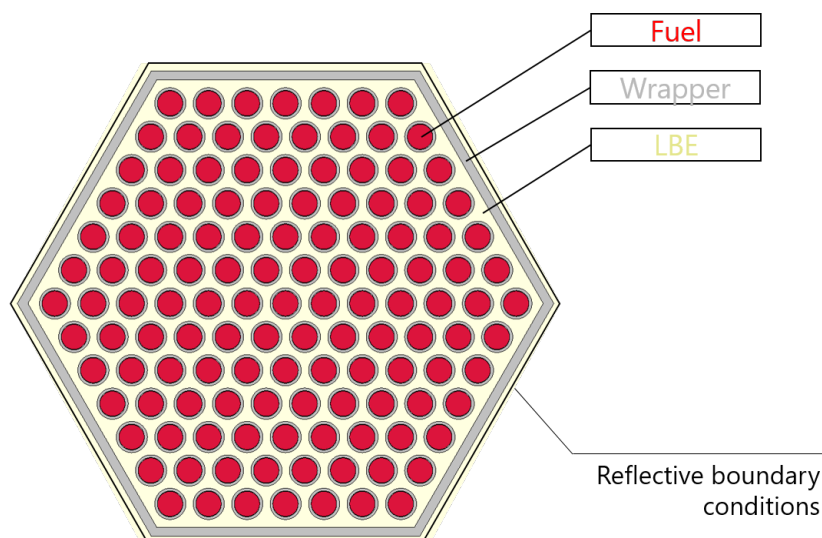


Figure 7.1: Cross sectional view of the MYRRHA fuel assembly

Homogeneous 3D FA model

The 3D FA model considers a realistic fuel assembly design in which each fuel pin as a stack of fuel pellets, reflectors, a steel structure and plugs. The top and bottom grids and the supporting structures made of stainless steel are also modelled. Such a model of the fuel assembly includes the neutron leakage from the axial boundaries, the neutron slowing down and the neutron reflection from above and below the FA active region. In the homogeneous model fuel is considered as a whole for depletion calculation and the flux to estimate the reaction rates is averaged on the total fuel region.

3D FA model with depletion zones

To take into account a impact of axial dependant depletion the fuel material is divided in sub-zones where the respective reaction rates are evaluated taking the flux averaged on the specific regions.

Simulation setup

The simulation setup of the Serpent FA models is summarized in Tab. 7.1. For the accurate 2D FA model one of the available predictor-corrector schemes provided by Serpent is employed. CE-LI method, constant-extrapolation linear-interpolation is based on the calculation of flux and cross section at the beginning of the step and then the same calculation at the end of the step after the material is depleted. The final burnup calculation is performed linearly interpolating the values of flux and cross sections from the beginning to the end of the step.

Table 7.1: Serpent simulation parameters

<i>Model</i>	Number of particles simulated	Number active generations	Predictor corrector	Simulation running time
2D accurate	1e5	250	CE-LI	87 min
2D simplified	1e4	250	No	17 min
3D homogeneous	1e5	250	No	83 min
3D axial depletion (40 zones)	1e5	250	No	490 min

7.2 Fuel assembly model assumptions

The objective of a FA model is to simulate the irradiation history of a FA loaded in the MYRRHA core, including the change of power associated to the in-core FA reshuffling described in Sec. 3.1.

Normalization parameter

The power generated by a FA as it is shuffled through the core is retrieved from the 3D full core simulation at equilibrium and it is used as a normalization parameter for the FA simulation. The power level of the FA is varied in each irradiation step according to the position the FA would have if it followed the actual in-core reshuffling scheme. A scheme of the irradiation history is provided in Fig. 7.2.

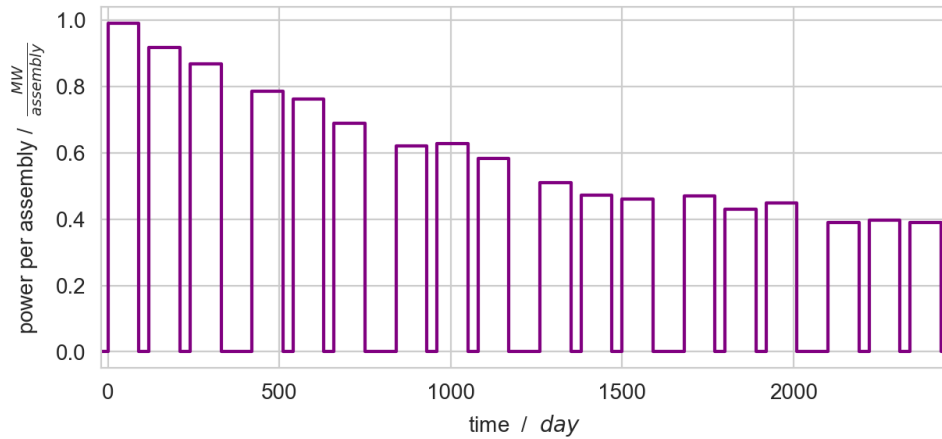


Figure 7.2: Irradiation history of the FA. The power level is retrieved from the core at equilibrium, taking into account the FA reshuffling the core.

Boundary conditions

The fuel assembly models, both 2D and 3D have radial reflective boundary conditions that keep the neutrons back in the system when they cross the boundaries.

This modeling assumption is not fully representative of what happens in the core where there is a net neutron current going in/out from the fuel assembly. Moreover, if reflective BCs are applied, the model is less suitable to reproduce the behaviour of a fuel assembly which is found in specific position such as near to a CR/SR or in the outer region of the core near to the reflector, when it is not surrounded by other FAs.

Fuel composition

The fuel burned is MOX 30% enriched in plutonium. The initial composition is the fresh fuel one, not subjected to decay.

7.3 Fuel assembly model limitations

The main limitation of FA models is introduced by the boundary conditions and it implies the neutron flux in the core is not reproduced by the FA model. In radial direction the neutron flux is almost flat while the actual shape in the core has peak in the core center and it slopes down toward the external region. It implies the differential depletion in radial direction cannot be caught by any FA model. This phenomenon, noticed in the full core model, is counterbalanced by the radial dependant depletion itself, since the fuel will be more depleted where neutron flux is originally higher leading to a reduction of fissions when burnup is higher. Moreover, the 2D FA model is not able to simulate the neutron leakage through the axial boundary, bringing to a flat neutron flux profile in axial direction. This issue is overcome by 3D models, that are investigated to assess the impact of axial burnup.

7.3.1 Spectral differences between core and fuel assembly simulations

Spectral differences between the core and FA simulation induced by modeling assumptions are explored in this section. The neutron spectrum of the fuel assembly irradiated in the core central position (101) is compared with the spectrum obtained in a FA simulation. The neutron spectra are depicted in Fig. 7.3.

Spectra are similar in the high energy region while differences emerge in the lower energy tail that is not present in the 2D FA model. However this region of the spectrum is nearly negligible, being two orders of magnitude lower. On the contrary, the small spectral differences in the fast region induce largest effect on the reaction rates. The integrated reaction rates for two relevant reactions are shown in Tab. 7.2 to emphasize the impact of spectral shift in the nuclide vector. The two reactions depicted are the fission of ^{239}Pu and the neutron capture in ^{240}Pu . A

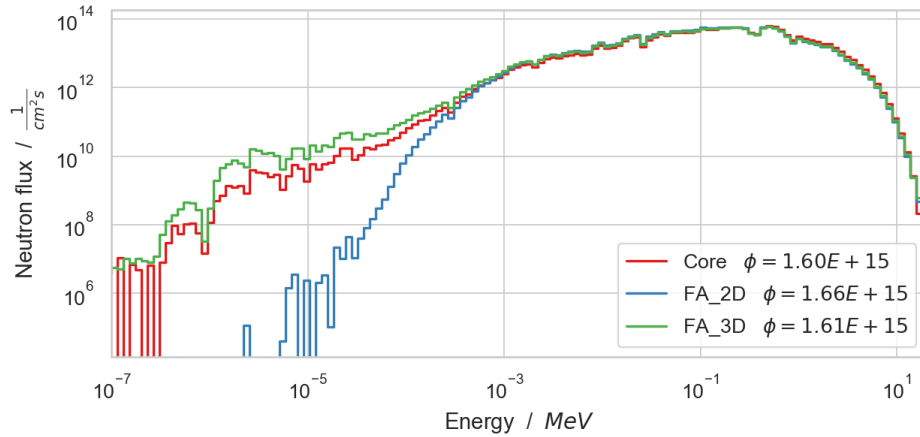


Figure 7.3: Spectral comparison among core and 2D/3D FA model.

Table 7.2: Reaction rates of fission and neutron capture respectively in ^{239}Pu and ^{240}Pu

Reaction Rate	(n, f) ^{239}Pu	(n, γ) ^{240}Pu
<i>3D core model</i>	2.79e15	7.14e14
<i>2D fuel assembly model</i>	2.88e15	7.82e14
<i>3D fuel assembly model</i>	2.86e15	7.94e14

good agreement is seen between the two FA models on the total numbers of fissions. In the core ^{239}Pu fission reaction rate is slightly lower, but it is compensated by more fissions in ^{238}U and ^{240}Pu , that is an indication of a harder spectrum. The neutron capture in ^{240}Pu is the first capture step bringing to the production of all minor actinides. 3D FA simulation provides the largest reaction rate, 1.5% higher than 2D and 12% higher than in the core simulation. From this analysis an increase in the production of minor actinides in the FA models is expected.

The spectral variations are marked between FA and core model as they are less relevant among 2D and 3D. They are only one aspect of the differences between the core and FA models. Another one to be investigated is the discrepancy in the power profile.

7.3.2 Power profile discrepancies

A large discrepancy in the 3D fuel assembly model with respect to the core simulation was noticed in the axial power profile. The first shows tails in the top and

bottom regions, that are present in the core simulation only in minor entity in assemblies in specific position, near control/safety rods or in the external position. This non-physical behaviour is related to the assumption of perfect reflectivity in the FA models and it is connected to the discussion on the spectral shift. In the FA models the neutron spectrum is softer, neutrons re-enter in the system with lower energy and they produce fissions; this phenomenon is more visible in the edge regions since in that part of the system the neutron flux is lower. The consequence is a local peak of power generated and, in turn a higher burnup in the edges. The effect on the power is therefore produced by combination of spatial and spectral effects.

Partial reflectivity impact on power profile

A method to take into account one aspect of the phenomenon is to set a fixed value of particles leakage through the boundaries.

It tackles part of the issue connected to the number of neutrons in the system but it does not consider the spatial and spectral effects.

A parametric study has been carried out to investigate the influence of neutron leakage parameter (albedo) on the power profile, that is the quantity more effected by the modeling assumption. The results of the analysis are summarized in Fig. 7.4. The fission reaction rate, being the count of the number of fissions in the

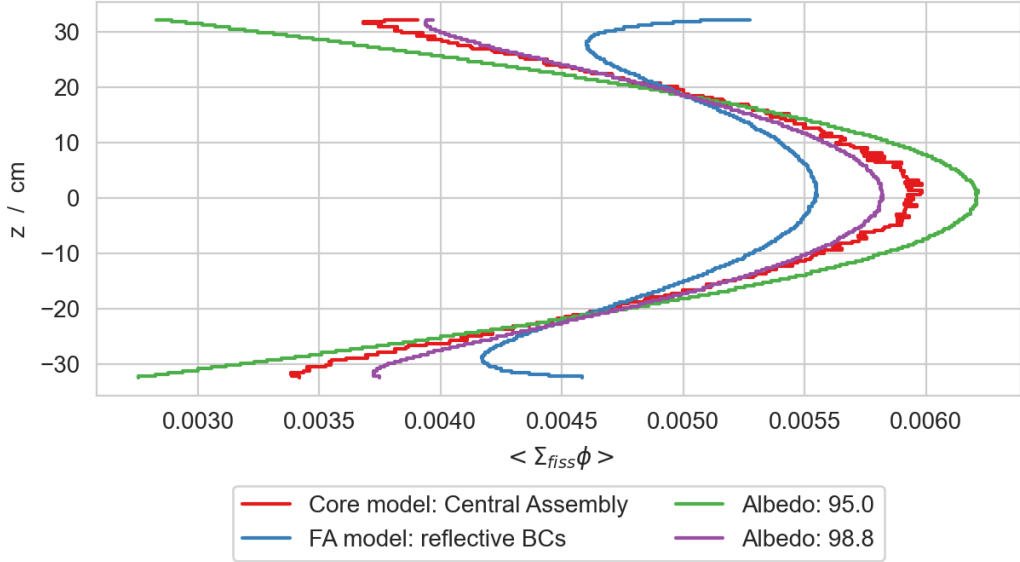


Figure 7.4: Axial profile of the normalized fission reaction rate. The result of the core model central assembly is compared with the one of FA model. Green and purple curves show the effect of albedo.

system is proportional to the power with a scaling factor equal to κ , the energy release per fission. The plot is normalized and the total number of fissions is set to one. The reduction of albedo affects the power (fission reaction rate) profile. The impact is evident passing from an albedo 98.9% to 95%. The power profile tends to be more peaked in the center and more depressed in the edge reducing albedo.

Partial reflectivity impact on nuclide vector

The impact of partial reflectivity boundary condition on the nuclide vector is assessed and the discrepancies for a subset of nuclides are presented; a similar analysis on a PWR system was carried out in [50] to estimate the sensitivity of SNF observables on the neutron leakage parameter itself. The neutron leakage rate have been chosen arbitrarily: it has been calculated in a reference fuel assembly criticality calculation imposing a target k_{eff} corresponding to the multiplication factor of the core at equilibrium. The albedo obtained is of 95.94 and 97.49% for the 2D and 3D model, respectively. It is used to run transport/depletion simulations to be compared with the results of models with pure reflective BCs, to investigate the impact of partial reflectivity and if it allows to target the core concentrations.

The comparison is carried out on a 2D model and the nuclide vectors at end of irradiation are compared. The deviations that arise are presented in Fig. 7.5. The concentration of most of volatile FP is not affected, with deviation up to

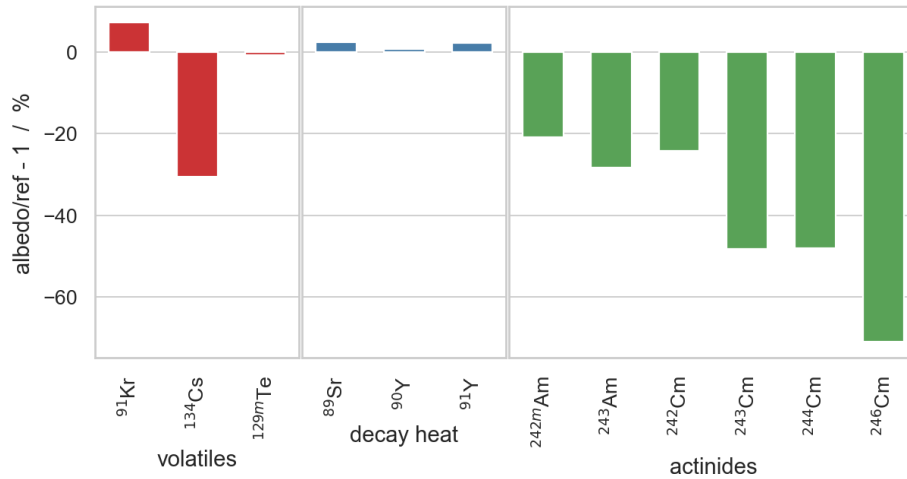


Figure 7.5: Deviation on the EoI nuclide inventory of the 2D FA with partial reflective boundary conditions (albedo=0.959) with respect to perfect reflective boundary conditions.

2%. An slight underproduction of xenon isotopes and overproduction of krypton is

observed. The most discrepant among volatiles is ^{134}Cs that is underproduced of 25% in case of albedo BCs. This is consistent with the hypothesis that reflective boundary conditions soften the spectrum because ^{134}Cs is produced by capture and the reaction rate increases if the spectrum gets softer. The same trend is observed on minor actinides, americium and curium isotopes.

The main conclusion from this preliminary study is that applying partial reflective boundary condition can modulate the spectrum to match the one of the core and attain more agreement with core result in term of nuclides inventory. The issue lies in the methodology employed to get the leakage fraction that should be more deeply investigated. Moreover the physical relationship between increase of the leakage rate and spectral hardening is not fully established.

7.4 Fuel assembly model output

This section aims to characterize the 2D and 3D fuel assembly model neutronic parameters. The evolution of k_{inf} and the neutron spectrum during irradiation are presented.

7.4.1 2D fuel assembly model output

k_{inf} and spectral plots are shown for the accurate 2D model, respectively in Fig. 7.6 and Fig. 7.7.

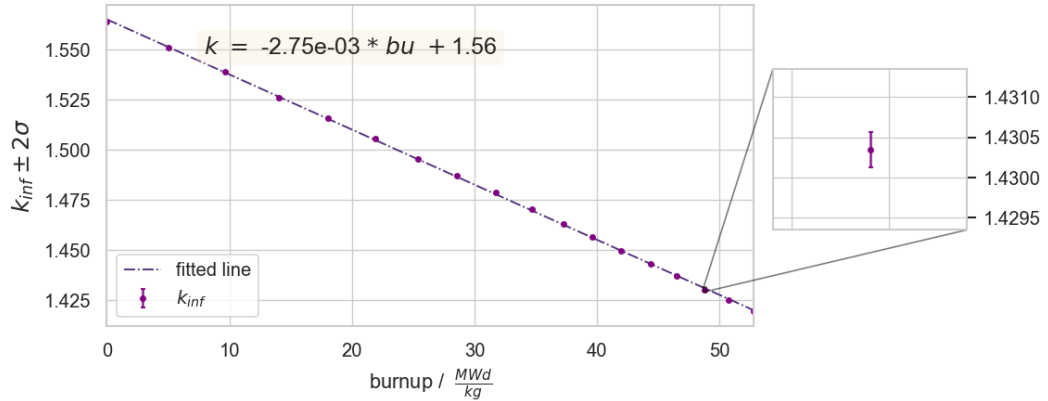


Figure 7.6: k_{inf} evolution in 2D fuel assembly with reflective BCs. Statistical uncertainty associated is shown in the zoom.

The multiplication factor reduces linearly with burnup and the uncertainty is

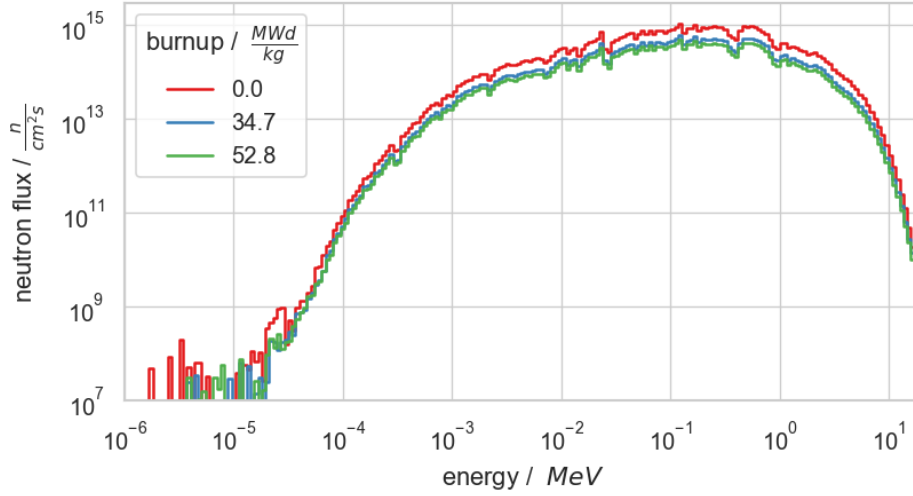


Figure 7.7: Neutron spectrum in the fuel assembly at different burnup level

on the order of 7 pcm. The curve has a slope:

$$\frac{dk}{dBU} = -2.75e - 3$$

The spectral variation as function of burnup is low. There is global reduction of the neutron flux due to the progressive reduction of the power but the shape stays constant during FA irradiation.

The main reason for FA model development is the possibility to perform uncertainty analysis. The 2D fuel assembly model is further simplified with the purpose of performing statistical sampling lowering the computational cost in term of time and resources. The simplifications do not concern the geometry but only the simulation parameters: the number of particles simulated is reduced of a factor 10 and the predictor-corrector was switched off. It is verified that the simplifications introduced have a very limited impact on the inventory of the nuclides analyzed. Largest deviation of around 3% occurs in ^{246}Cu , meaning that the simplified model is suitable to perform uncertainty analysis being representative of the accurate one.

The 2D fuel assembly model is suitable for uncertainty quantification of the nuclide vector. The preliminary analysis of the neutronic parameters shows that the k_{eff} reduces almost linearly with burnup and the shape of the neutron spectrum stays the same increasing the burnup of the assembly.

7.4.2 3D fuel assembly models output

The 3D fuel assembly simulation is performed introducing depletion zones uniformly distributed in axial direction. In this way each region is independently depleted and the local neutron spectrum is taken into account when estimating the reaction rates used to solve the burnup equations. The variation of the k_{inf} and the nuclide inventory as function of the number of depletion zones is assessed in this section.

Multiplication factor

k_{inf} evolution is presented in Fig. 7.8. The simulation without divisions is taken as a reference. The reduction of multiplication factor is linear with burnup as in 2D case and the value at specific burnup steps is shown in Tab. 7.3. The impact of

Table 7.3: k_{inf} in the homogeneous 3D fuel assembly model (without depletion zones) as function of burnup.

<i>burnup</i> MWd/kg	0	34.7	52.8
k_{inf}	1.36	1.28	1.24
<i>Statistical error</i> pcm	22	25	25

axial depletion zones on k_{inf} is investigated in Fig. 7.8 where the deviation with respect to homogeneous model is assessed.

The values match for all the models with depletion zones considered in the range of 2σ . A slight reduction of k_{inf} with respect to the homogeneous model is noticed at high burnup levels. This reduction is limited to 200 pcm in the last irradiation cycle, induced by a variation in the material composition.

Nuclide vector

The deviation in the nuclide vector introduced by the fuel material division is negligible for most of fission products, plutonium and americium isotopes. The most affected nuclides are shown in Fig. 7.12, where the EoI concentrations are compared in the model with depletion zones with respect to the homogeneous one. The largest discrepancies are observed for higher curium isotopes and they tend to grow increasing the number of zones. For all the nuclides analysed the deviations are lower than 1% except for ^{246}Cm ($t_{\frac{1}{2}} = 4.730\text{e}3$ y) that is underestimated up to 5% not considering axial depletion.

The axial fuel material sub-division in the 3D fuel assembly model has a limited effect on the neutronic parameters and the nuclide vector.

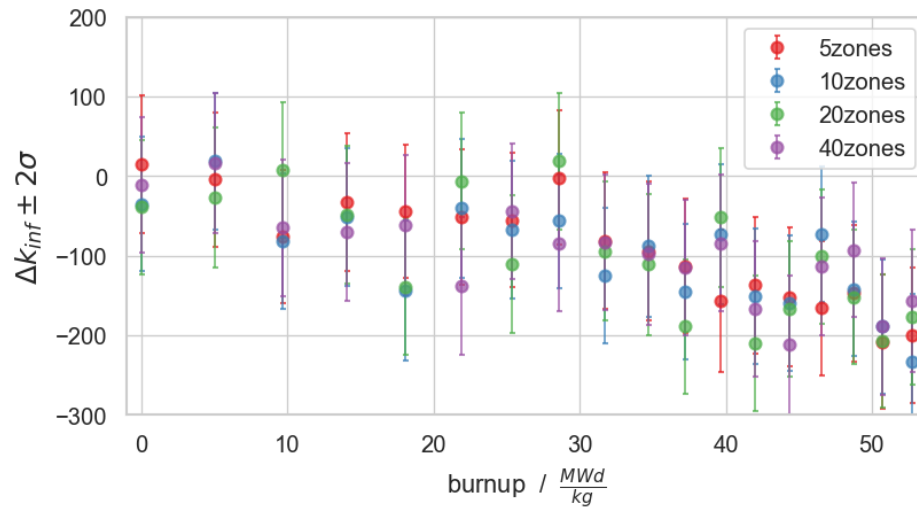


Figure 7.8: k_{inf} variation with respect to homogeneous 3D FA model introducing axial depletion zones.

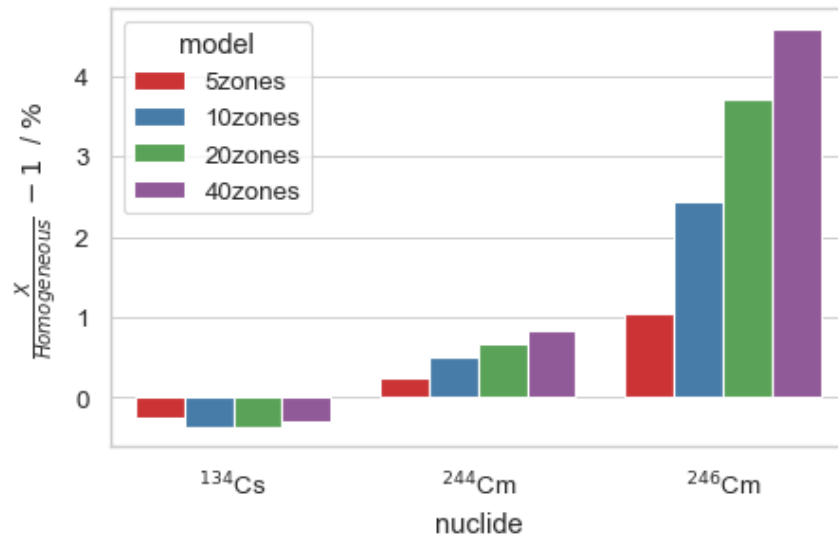


Figure 7.9: Deviation on EoI concentrations evaluated in 3D FA simulations: comparison of axial depletion zones with respect to the homogeneous model.

7.5 Comparison of fuel assembly model with respect to equilibrium core output

This section is devoted to compare the nuclide inventory obtained in the fuel assembly simulations with the output of the equilibrium core. The models investigated are those presented in this chapter, the comparison is carried out between the nuclide vector after the first irradiation cycle (at higher power) in the FA model and the fuel irradiated in position 101 (central position) in the core.

7.5.1 2D fuel assembly model

The deviations of the 2D fuel assembly with full reflective boundary conditions are presented in Fig. 7.10. The models show good agreement for most the fission

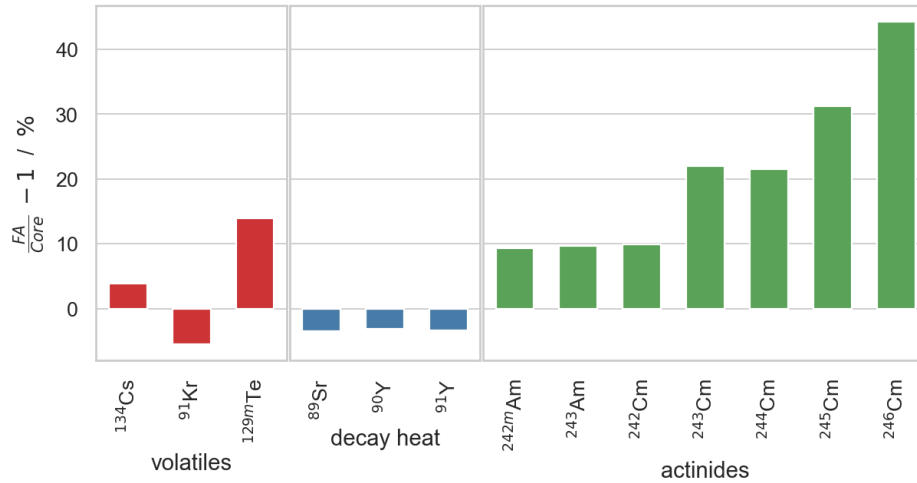


Figure 7.10: Comparison of the EoC concentration in a 2D fuel assembly model with full reflective boundaries to the results obtained from a core simulation.

products of interest and plutonium isotopes. Discrepancies arise in minor actinides and some specific FPs, such as ^{91}Kr ($t_{1/2} = 8.57$ s), ^{129m}Te ($t_{1/2} = 33.6$ d), ^{134}Cs . The production of all minor actinides is overestimated in the fuel assembly as a consequence of the spectral shift discussed in Sect. 7.3.1. They all comes from successive captures from plutonium and the capture reactions rate are enhanced as a consequence of softer spectrum. This phenomenon brings to an overestimation up to 40% in ^{246}Cm .

As indicated in the previous section, one of the main limitations resides in the difference of the neutron spectrum obtained in the FA model respect to the fuel assembly irradiated in the core. A possible solution was investigated, i.e. varying

the boundary conditions to modulate the spectrum. Fig. 7.11 shows the comparison among the FA model with partial reflective boundary conditions and the core on the nuclide inventory at EoC. An opposite behaviour is encountered with respect to the previous case, showing that the nuclide vector is strongly affected by the partially reflective boundary condition in this case study. The albedo parameter

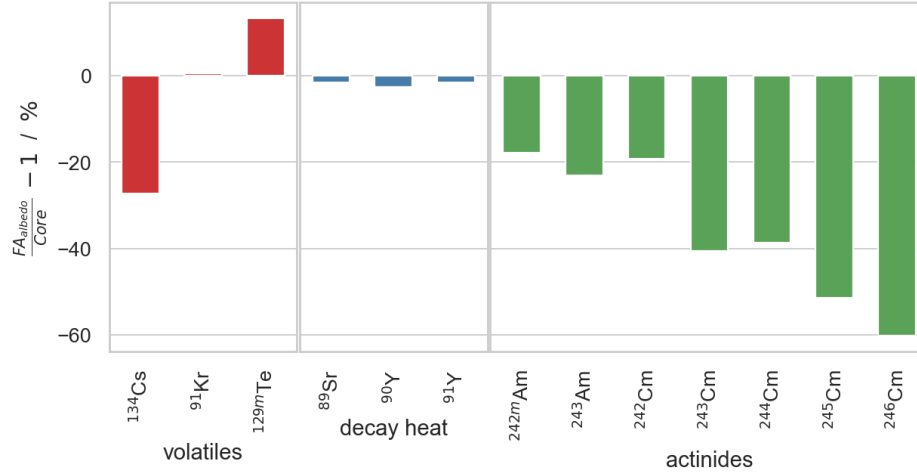


Figure 7.11: Comparison of the EoC concentration in a 2D fuel assembly model with partial reflective boundary conditions to the results obtained from a core simulation.

used for the simulation was the same discussed before, the one that guarantees to obtain the same k_{eff} of the equilibrium core. This choice is arbitrary and does not reflect the real neutron leakage from the fuel assembly analysed but it points out where the discrepancy comes from.

As previously stated, the purpose of the fuel assembly model is not to be fully representative of the fuel assembly irradiated in the core in the best estimate results but to provide a surrogate model to perform uncertainty quantification. The scope of this work in this regard is limited to assess and try to explain the discrepancies obtained.

7.5.2 3D fuel assembly model

The analysis of nuclide vector obtained in the 3D fuel assembly simulation is carried out in this section. The comparison with the results of the 2D model are presented in Fig. 7.12.

^{134}Cs shows the largest discrepancy around 6% among all the nuclides investigated. Other concerning fission products show discrepancies lower than 1%. Minor

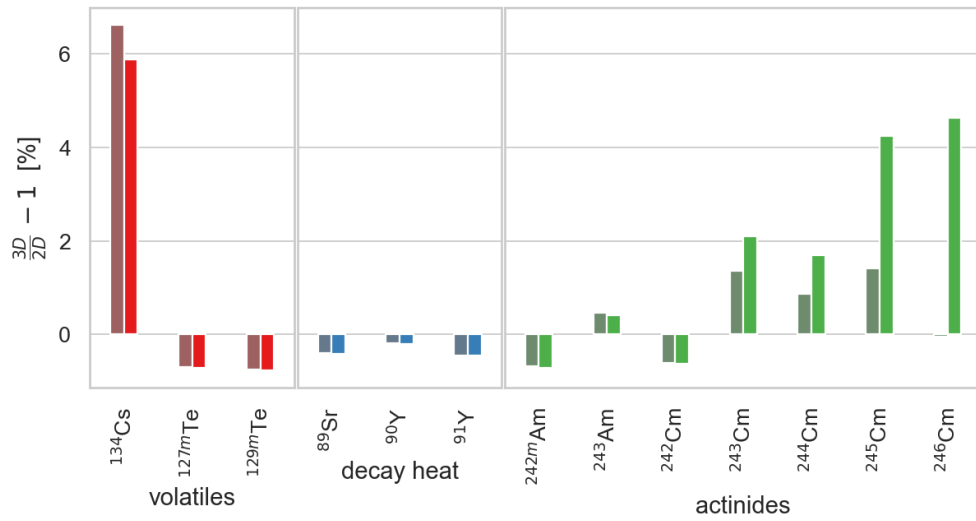


Figure 7.12: Comparison of EoC nuclides concentration in 3D FA model with respect to the results of the 2D fuel assembly model. Bright and dull bars are referred to the model with and without axial depletion respectively.

actinides are in agreement with 2D model if the axial division of the fuel material is not taken into account, as highlighted by the dull bars in the plot.

Chapter 8

Nuclear data uncertainty

This section covers the uncertainty analysis carried out on the nuclide vector and derived quantities such as the decay heat. The output uncertainty is determined by the uncertainties of modeling parameters as well as input data. Particular attention is paid on the uncertainty coming from nuclear data that has been proven to be one of the main contributors in many applications. In this work uncertainty coming from nuclear data is estimated by means of statistical sampling techniques.

Neutronic cross section data contained in JEFF-3.3, ENDF/B-VIII.0 and JENDL-4.0u nuclear data libraries and neutron fission product yields coming from JEFF-3.3 are propagated in separate runs following the methodology briefly described in Sect. 2.3.2.

8.1 Uncertainty on nuclide vector

The nuclide vector and its evolution as function of irradiation/decay time is the main output of the burnup calculations performed in this work.

8.1.1 Cross sections uncertainty propagation

The propagation of cross section uncertainty is performed considering all available nuclides which uncertainty is present in the three previously discussed libraries. A set of 200 samples is generated to perform statistical sampling. The determination of the sample size is based on observing the convergence of the inputs and of the outputs. The exhaustive list of the nuclides perturbed and the output convergence analysis are presented in appendix B, while the perturbation coefficients convergence is shown in 2.3.2. The output presented in this work is the uncertainty associated to the nuclide vector with main focus of the relevant nuclides already discussed.

Impact of cross section uncertainty on actinides concentrations

The first category of nuclides analysed comprises the actinides important for spent fuel management, and their concentration uncertainties at EoI are depicted in Fig. 8.1.

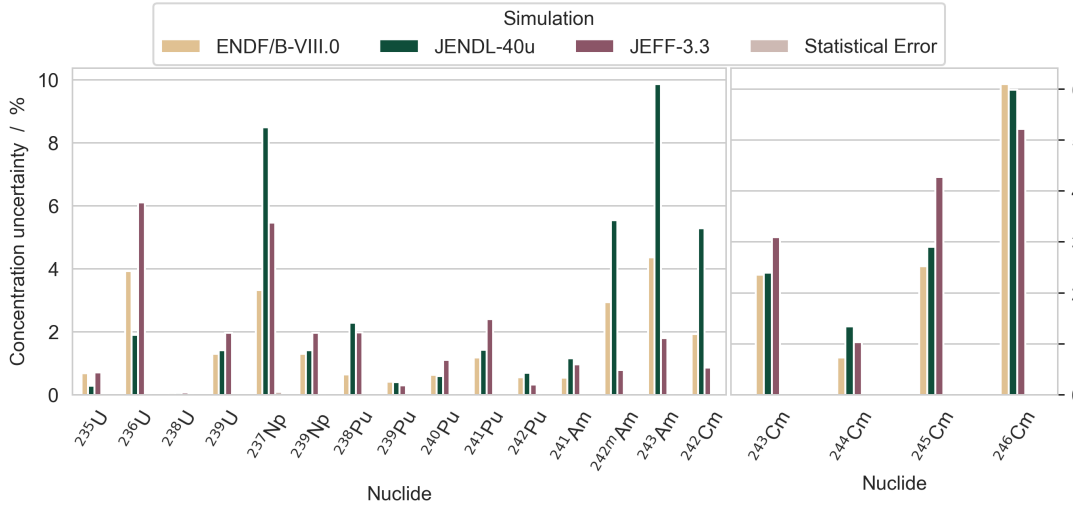


Figure 8.1: Actinides concentration uncertainty at EoI coming from cross section uncertainty propagation.

Uncertainty of uranium isotopes

²³⁵U ($t_{1/2} = 7.038e8$ y) and ²³⁸U ($t_{1/2} = 4.468e9$ y) show limited uncertainty. ²³⁵U neutron capture cross section uncertainty brings to a progressive increase of its uncertainty with burnup. On the other side, it constitutes the major source of uncertainty for ²³⁶U ($t_{1/2} = 7.370e7$ y), that constantly builds up in the system. The discrepancies of the libraries are explained looking at the relative standard deviation in the fast region where the uncertainty given by JENDL-4.0u NDL is lower with respect to the others. ²³⁸U shows negligible uncertainty. The sensitivity to any production/depletion mechanism is low because it is present in large amount in the fresh fuel and its concentration varies less than 1% during irradiation.

Uncertainty of plutonium isotopes

Pu isotopes are initially present in the fresh fuel and depleted by means of fission, neutron capture and decay. Their uncertainty is in the range 0.25 to 2.5% at EoI. The uncertainty evolution of plutonium isotopes is shown in Fig. 8.2, it tends to increase with burnup and it evolves in the opposite way respect to their buildup, displayed in Fig. 6.9.

²³⁸Pu production is mainly bonded to ²⁴²Cm that is ahead in the capture chain

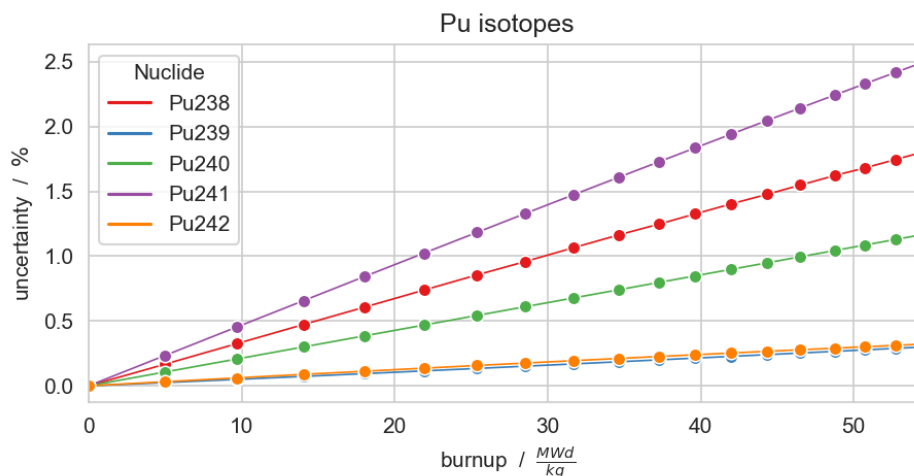


Figure 8.2: Plutonium isotopes uncertainty evolution as function of the FA burnup.

while its depletion happens by neutron capture; since its concentration varies of 15% during irradiation, the global effect of production/depletion has a limited impact. JEFF-3.3 and JENDL-40u give a similar evaluation of the relative standard deviation of ^{238}Pu total cross section, larger than ENDF/B-VIII.0 and this is consistent with the corresponding bars in Fig. 8.1. The uncertainty concentration of ^{242}Cm affects the ^{238}Pu uncertainty in lower amount being its depletion greater than the production.

^{239}Pu has very low uncertainty, coming from its own total cross section; ^{240}Pu is produced and depleted by neutron capture and the two mechanisms are of the same order of magnitude. So its uncertainty is both due to capture cross section of ^{239}Pu and its own cross section.

^{241}Pu has relatively low half-life and it decays into ^{241}Am other than undergoing fission. Its uncertainty is the highest amongst plutonium isotopes since its concentration has a largest variation during irradiation and it is more sensitive to the production/depletion during irradiation. ^{241}Pu mainly comes from neutron capture in ^{240}Pu . The uncertainty given by JEFF-3.3 for this XS is greater than the other libraries in the region from 0.01 to 1 MeV and this explains why the output uncertainty obtained with this NDL is higher.

^{242}Pu ($t_{1/2} = 3.735\text{e}5$ y) concentration undergoes a limited variation, its uncertainty comes from $\sigma_{(n,\gamma)}$ of ^{241}Pu and its own σ_t . Reduced uncertainty is observable with JEFF-3.3 since covariance matrices of ^{242}Pu are not available in this library.

Uncertainty of americium isotopes

The americium isotopes are produced by successive captures from ^{241}Am that in turn comes from β_- decay of ^{241}Pu ; the source of uncertainty for these nuclides is primarily attributed to the capture cross sections of their respective parent. JEFF-3.3 systematically underestimates their uncertainty since covariance matrices of ^{241}Am , ^{242}Am and ^{242m}Am are not available.

^{241}Am is initially present in the fresh fuel, which results in a lower uncertainty, primarily influenced by the uncertainty on the concentration of ^{241}Pu and its $\sigma_{(n,\gamma)}$ (neutron capture cross section). The uncertainty on the concentration of this nuclide has a strong impact on the decay heat rate at 70 years of decay since it is one of the main contributors. JENDL-4.0u NDL gives the largest estimate of ^{242m}Am and ^{243}Am uncertainty since it provides greater cross section uncertainties in the region from 0.01 to 1 MeV.

Uncertainty of curium isotopes

^{242}Cm is an important contributor to the decay heat of SNF in the first years of cooling and it shows very similar uncertainty of ^{242m}Am , which is its major production path. The uncertainty associated to ^{242}Cm capture cross section is of the order of 20 to 40% in the energy range of interest in JEFF-3.3 but it has negligible impact on its concentration uncertainty. On the other hand, this same source of uncertainty has a significant effect on the product of the reaction, ^{243}Cm . The uncertainty for ^{243}Cm is consistently around 25 to 30%, and it is primarily attributed to its production mechanism since it is less sensitive to its total cross section. The uncertainty associated to ^{243}Cm is not propagated to ^{244}Cm because the latter is only produced in limited amount through neutron capture reactions. The primary source of production of ^{244}Cm is the β_- decay of ^{244m}Am . Therefore, the uncertainty in ^{244}Cm arises from the uncertainties in the americium isotopes involved in this decay process.

The uncertainty on the concentrations of heavier curium isotopes increases up to 40% and 50% and is mainly driven by the uncertainties in their parents capture cross sections. ^{245}Cm concentration uncertainty is overestimated by JEFF-3.3 since it gives greater standard deviations with respect to the other libraries. ENDF/B-VII.0 and JENDL-4.0u have the same covariance matrix for the capture cross section of ^{244}Cm so the mismatch in the ^{245}Cu concentration uncertainty is due to the concentration uncertainty of the parent nuclide. The opposite happens when considering ^{246}Cu : even in this case JENDL-4.0u and ENDF/B-VIII.0 share the covariance matrix evaluations but they give much larger uncertainties than JEFF-3.3 and this translates in larger concentration uncertainties in ^{246}Cm as depicted in the plot.

Impact of cross section uncertainty on fission products concentrations: volatiles & decay heat contributors

The second category analyzed includes volatile fission products conveying the largest dose in case of release identified in Sect. 1.2 and the FPs contributing to decay heat. Almost all of them are direct fission products, so their production is proportional to the number of fissions in the system that is determined by the input power. The low uncertainty observed comes from the small fraction produced by neutron capture reactions and the statistical error inherent in Monte Carlo. The EoI uncertainty concentration of both categories is depicted in Fig. 8.3 and the only non-negligible contribution comes from ^{134}Cs and ^3H .

^{134}Cs is almost 100% produced by neutron capture in ^{133}Cs and its uncertainty

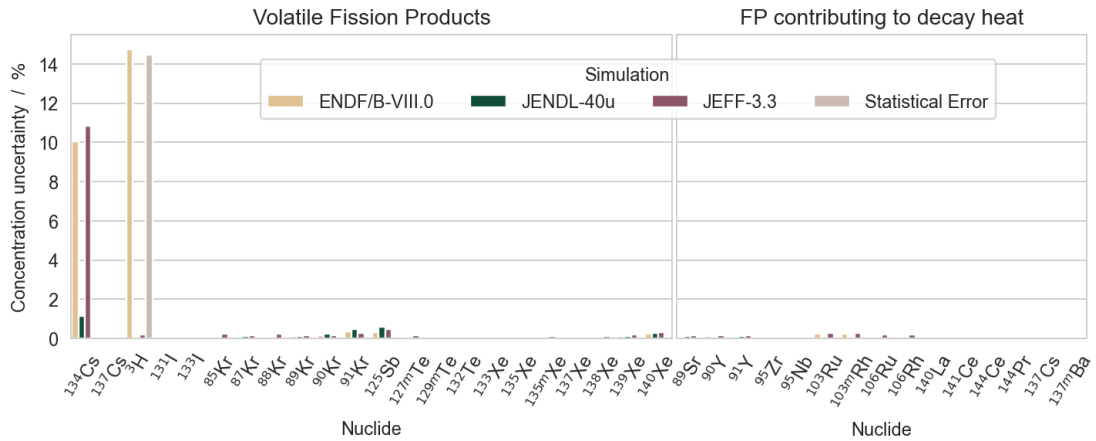


Figure 8.3: Fission products concentration uncertainty at EoI coming from cross section uncertainty propagation. Divided in volatiles and decay heat contributors.

directly comes from the capture cross section of the parent. The uncertainty obtained with JEFF-3.3 and ENDF/B-VIII.0 is around 10% in agreement with the relative standard deviation given on the (n, γ) cross section that ranges from 4% in the thermal up to 40% in the fast region in both libraries. Lower uncertainty is obtained with JENDL-4.0u NDL which does not provide uncertainty measures for ^{133}Cs and fission products in general.

The uncertainty associated with ^3H has a distinct source, which deserves further examination. In critical configurations, its primary production path is through ternary fission, a process in which three products are generated from a fission reaction. While this is a rare event with a low yield, it remains significant because it contributes to the accumulation of tritium within the fuel assembly. The uncertainty obtained from ENDF/B-VIII.0 library arises from the fact that the fission yield data provided in the library does not account for ternary processes, as

demonstrated in Fig. 8.4, with JEFF-3.3 used as a reference. If tritium production

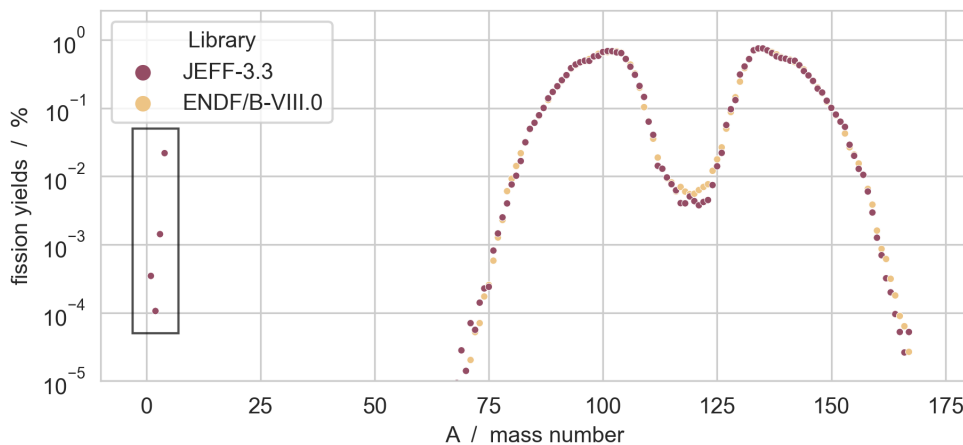


Figure 8.4: Independent fission yields as a function of product mass number for ^{239}Pu in the fast region ($E = 400 \text{ keV}$).

by fission is not taken into account its concentration is underestimated of five orders of magnitude and in this case the amount produced is so small that the uncertainty observed comes from statistical fluctuations as shown by the last bar in Fig. 8.3 and it is irrelevant as the tritium produced is negligible. The assumption of neglecting ternary fission gives a strong underestimation of the production of one of the most important nuclides in the analysis.

A second issue connected to tritium is that the production mechanism is not the same in sub-critical configuration, where its production is maximized, so part of its uncertainty is not considered in a critical system. A deeper analysis on this regard is carried out in appendix A.

The uncertainty of the other fission products coming from the XS uncertainty is almost negligible, therefore to give a more reliable estimation of the uncertainty of the other relevant FPs is necessary to broaden the analysis to the neutron fission product yields that are expected to be the main source of uncertainty for fission products.

The propagation of cross sections uncertainty by means of statistical sampling provides the uncertainty estimation of the nuclide concentrations. The impact on plutonium isotopes is limited to 2.5% and it increases for minor actinides up to 60% in ^{246}Cm . The uncertainty of fission products concentrations is negligible since their production is not affected by cross sections variation; ^{134}Cs is the exception, being produced by neutron capture in ^{133}Cs . The uncertainties vary depending on the NDL employed since each of them provides different covariance matrices.

8.1.2 Nuclear fission product yields uncertainty propagation

The need for uncertainty values of fission product concentrations drove to conduct the propagation of uncertainty for the Neutron Fission Product Yields (NFPY) alongside the neutron cross-section data. Covariance matrices are not provided for neutron fission product yields, the uncertainty measure is given in term of variance and therefore correlations among fission yields are not taken into account. This brings to quite large output uncertainties associated since σ^2 is of the order of 10% for most of Independent Fission Yields (IFY). Methods to reduce independent fission yields uncertainty were developed, such as introducing conservation equations and taking advantage of the uncertainty evaluations on the cumulative FY to generate covariance matrices from the available data as reported in [51]. These methods are not applied in this work and the raw uncertainty data of IFY are propagated. The only normalization procedure applied was on the sum of all the independent fission yields that must be equal to the fragments of the fission, that is slightly greater than two if ternary fission events are accounted.

The output uncertainties of the EoI nuclide concentrations are presented in Fig. 8.5 and the perturbed IFY comes from JEFF-3.3 NDL The uncertainties on actinides

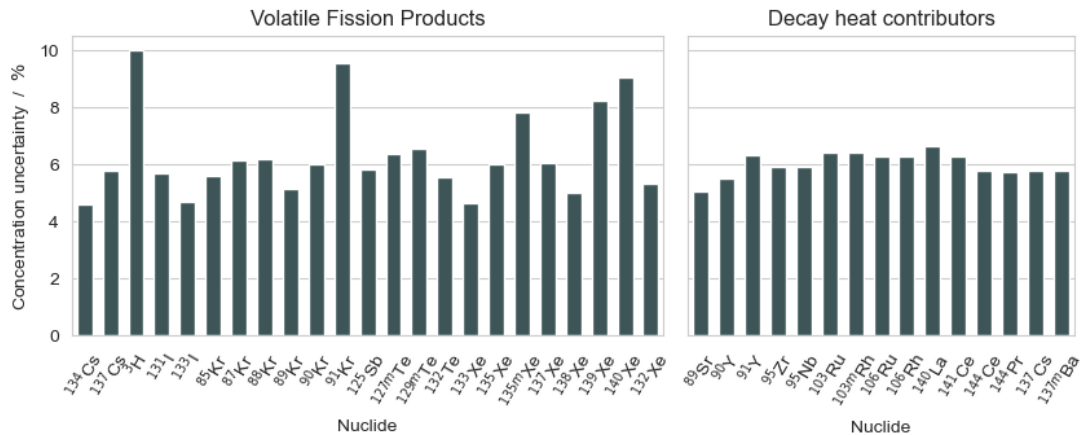


Figure 8.5: Fission products concentration uncertainty at EoI coming from neutron fission product yields uncertainty propagation. Divided in volatiles and decay heat contributors.

are negligible since NFPY data do not interact with their production/depletion, while they have a higher impact on the other observables. The production of a nuclide through fission is linearly dependent on its fission yield when there are no other production mechanisms involved, such as the decay of other fission products or neutron captures. On the contrary most of the nuclides investigated are both

produced by fission and decay of other short lived fission products, which implies the uncertainty of a target nuclide is sensitive to the uncertainty on its own fission yields and all the fission products decaying in it.

The uncertainty on ^{134}Cs , that is not a direct fission product, comes from the uncertainty of his parent ^{133}Cs . The latter has a very small independent fission yield but it is the stable end of chain of the $A=133$ β_- decay line so its uncertainty is determined by all the nuclides in the chain and it explains why ^{134}Cs , ^{133}Xe ($t_{1/2} = 5.247$ d) and ^{133}I ($t_{1/2} = 20.87$ h) show the same level of uncertainty. The interaction among the FP involved in the chain is clarified by Fig. 8.6, that shows the correlation among the fission products concentrations. The correlation matrix

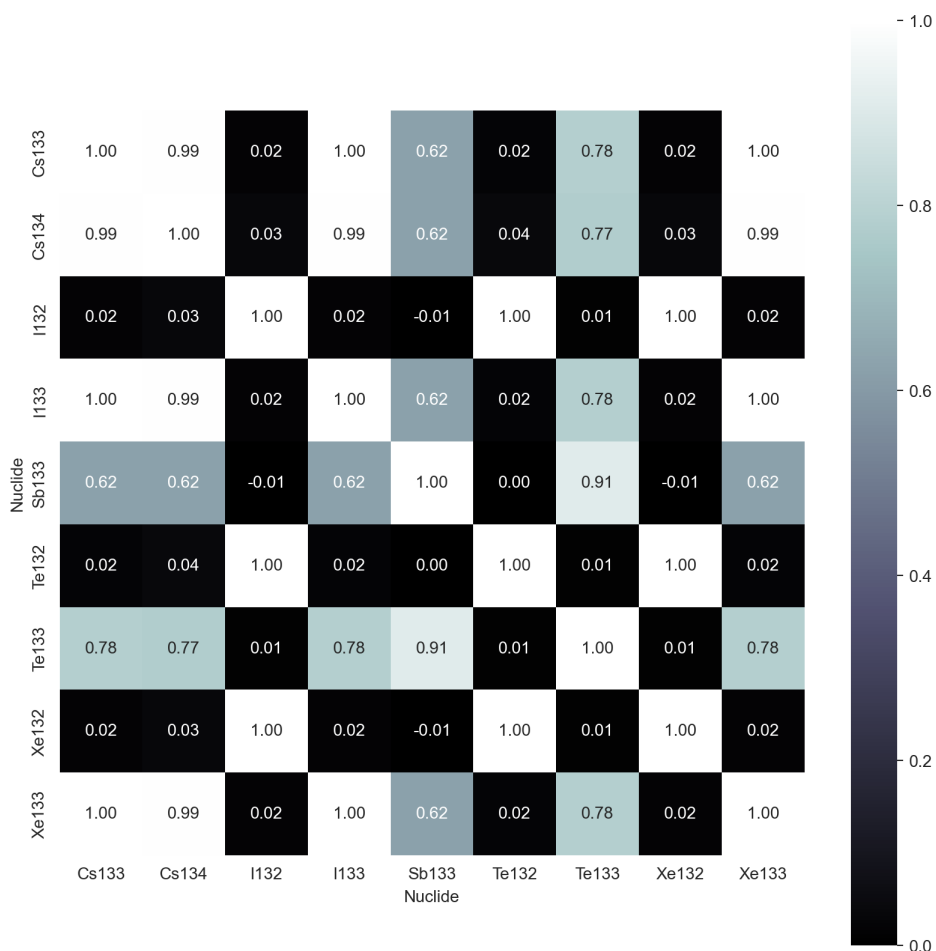
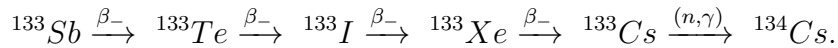


Figure 8.6: Correlation matrix among nuclides contributing to the uncertainty of ^{134}Cs

measures how much the population of an item is explained by another one in the

list. The reaction chain analyzed in the following:



${}^{132}\text{I}$ ($t_{\frac{1}{2}} = 2.295$ h) and ${}^{132}\text{Xe}$ (stable) are added to demonstrate they are not relevant in the production of ${}^{133}\text{I}$ and ${}^{133}\text{Xe}$ by capture and in fact they show null correlation. On the contrary there is full correlation in the chain between ${}^{134}\text{Cs}$ and ${}^{133}\text{I}$, i.e. all the uncertainty comes from this fission product. In turn ${}^{133}\text{I}$ is both directly produced by fission and partly comes from ${}^{133}\text{Te}$ ($t_{\frac{1}{2}} = 12.45$ min) decay as witnessed by their cross-correlation of 0.8. The same conclusion, in a qualitative way can be drawn looking at the mismatch between independent and cumulative fission yield of each couple of nuclides.

${}^{137}\text{Cs}$ is a concerning volatile nuclide and it is bonded to ${}^{137m}\text{Ba}$, contributing to decay heat at 3 y of decay; its uncertainty is due to its own fission yield and the one of ${}^{137}\text{Xe}$ ($t_{\frac{1}{2}} = 3.818$ min) and ${}^{137}\text{I}$ ($t_{\frac{1}{2}} = 24.51$ s), which contribute to its production. ${}^3\text{H}$ shows the largest uncertainty among the subset of fission products considered. It is around 10% and it is only induced by the uncertainty of its fission yield. Amongst krypton isotopes the one showing largest uncertainty is ${}^{91}\text{Kr}$ and it mainly comes from its NFPY uncertainty since there is a low mismatch between the independent and cumulative fission yield.

The uncertainty of ${}^{133}\text{Xe}$ and its origin was already discussed while commenting Fig. 8.6; it is the xenon isotope with lower standard deviation around 4% while ${}^{135m}\text{Xe}$ ($t_{\frac{1}{2}} = 15.3$ min), ${}^{139}\text{Xe}$ ($t_{\frac{1}{2}} = 39.69$ s) and ${}^{140}\text{Xe}$ ($t_{\frac{1}{2}} = 13.6$ s) have the largest uncertainty around 8%. The first mainly comes from β decay of other fission products while the last two have quite high yield and are direct fission product, so their uncertainty derives from their own NFPY data.

The NFPY uncertainties in form of standard deviation are propagated and they produce a non-negligible uncertainty on the concentrations of the fission products. The uncertainty associated to the volatile nuclides and decay heat contributors is between 5 and 10%.

Even though all the contributors to decay heat exhibit uncertainties of approximately 6%, their impact on the overall uncertainty of decay heat is explored in the subsequent section.

8.2 Uncertainty on decay heat

The envelope decay heat in the core model at equilibrium was discussed and estimated in Sect. 6.3. Fuel assemblies with different burnup convey the largest value

at different decay time and the contribution of the nuclide species more relevant for decay heat is established as function of time.

In this section the uncertainty on the decay heat as function of decay time is estimated. The sources of uncertainty considered in this analysis are those introduced in the previous section. The objective here is to comprehend how the uncertainties of individual nuclides combine to form the overall uncertainty of an integrated quantity like decay heat.

Uncertainty on decay heat evolution provided by most irradiated assembly

A first result presented in Fig. 8.7 shows the evolution of decay heat uncertainty

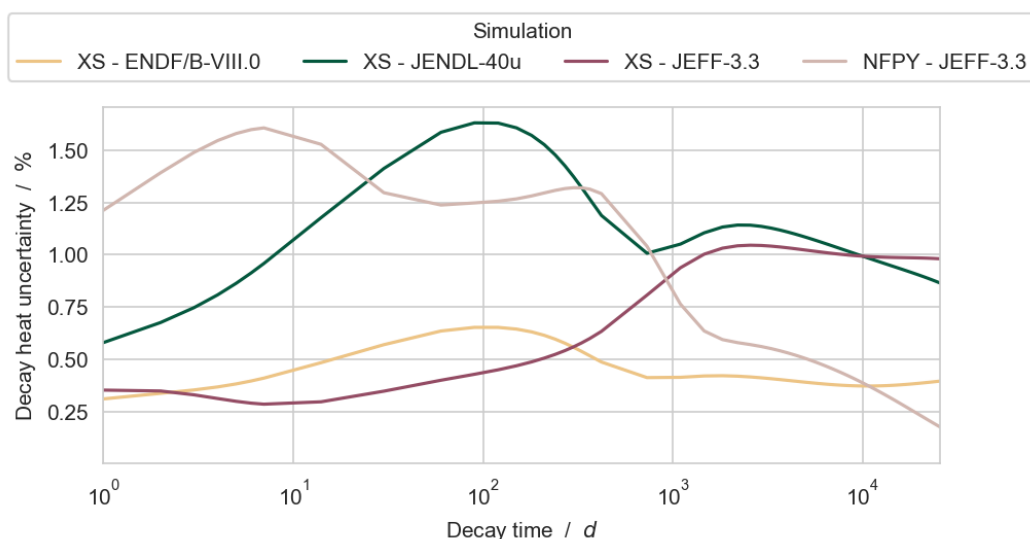


Figure 8.7: Decay heat uncertainty evolution from cross section and fission yield uncertainty propagation. A decay time up to 70 years is considered.

for a fuel assembly being irradiated for 18 cycles, that gives the largest contribution in the long term. The FPs relevant for decay heat are not affected by cross section uncertainties but they have large uncertainty coming from NFPY since they are produced directly by fission or by primary fission products decay. This phenomenon is demonstrated by the plot since the decay heat uncertainty is dominated by NFPY uncertainty in the short term, when fission products are relevant. For longer decay time, the major contributors are actinides, ^{242}Cm up to 2 years followed by ^{238}Pu and ^{241}Am . The cross section uncertainties of these nuclides explain the evolution of decay heat uncertainty determined by XS propagated from different NDL, that were already commented in the previous section. Conservative estimations are provided by JENDL-4.0u that gives larger uncertainty estimation of ^{242}Cm , ^{238}Pu and ^{241}Am concentrations. JEFF-3.3 gives the largest uncertainty in the last part

of the transient. The peak uncertainty estimated is around 1.75% between 5 and 200 days after discharge and it is provided propagating the cross sections from JENDL-4.0u.

The total decay heat uncertainty quantification is performed propagating cross section and NFPY at the same time and considering both the least and most irradiated assembly that convey the largest decay heat respectively for short and long decay periods. JEFF-3.3 sampled nuclear data are employed to generate perturbed input files.

The decay heat uncertainty of the most irradiated assembly is expected to be the quadratic sum of the two effects (cross section and NFPY) considered separately if the two mechanisms are independent; the mathematical formulation is written down in eq. (8.1).

$$u_{global} = \sqrt{u_{xs}^2 + u_{nfp}^2} \quad (8.1)$$

The two approaches do not provide a significant difference on the uncertainty evolution, therefore the methodologies are equivalent and there is negligible interaction between the uncertainties conveyed by cross sections and NFPY, so that the effects on the decay heat are independent.

The uncertainty quantification of the decay heat of the fuel assembly irradiated for one cycle is performed, since it provides the envelope decay heat in the short decay period after discharge. The uncertainty propagation is carried out propagating both cross sections and fission yields from JEFF-3.3 and the outcome is shown in Fig. 8.8. In the short term in the assembly irradiated one cycle shows the largest uncertainty as well as the largest decay heat. For longer time scales the uncertainty of the 18 cycles irradiated FA is larger. This phenomenon is related to the uncertainty of the main contributors that can vary with burnup, as for plutonium isotopes (Fig. 8.2) and to the different sensitivity of the decay heat to certain nuclides. The uncertainty will increase if a nuclide with large uncertainty is more relevant for the decay heat at a specific decay time. The correlation evolution, the dashed curve in Fig. 8.8, gives an indication on how much the decay heat uncertainty in the two cases comes from the same source. For example in the long term decay heat is given by ^{238}Pu and ^{241}Am : this takes place both in the fuel assembly irradiated for 1 and 18 cycle and this implies high correlation, although at the same time the resulting uncertainty is quite different since it increases with burnup for the two nuclides. Therefore the resulting uncertainty after 1 cycle is much lower.

Similar conclusions can be drawn on the high correlation from the beginning of the transient up to one day of decay. In this interval of time, decay heat is dominated by the short lived nuclides produced in the same way in the first and

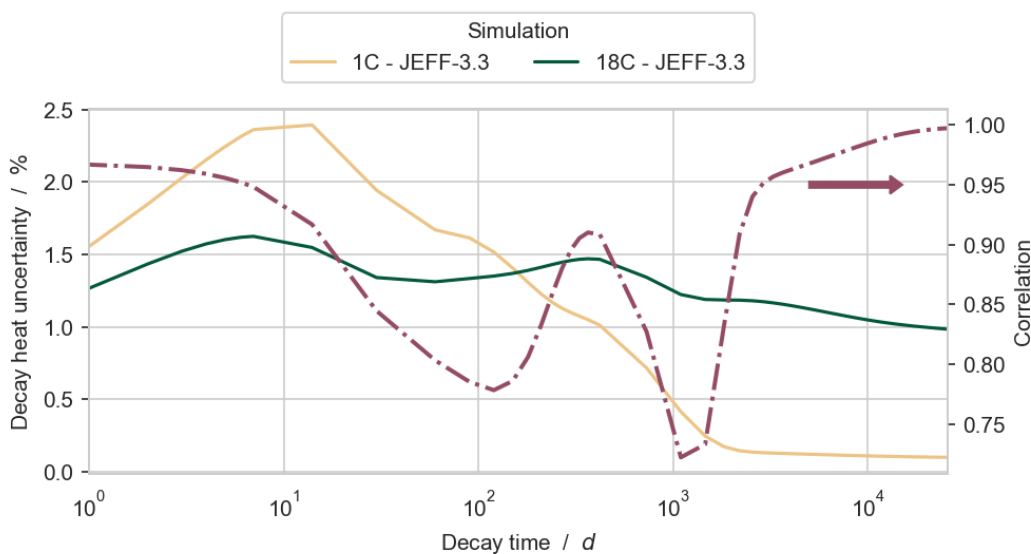


Figure 8.8: Decay heat uncertainty evolution of a fuel assembly irradiated for 1 and 18 cycles. Brown line shows the correlation between the two cases.

last irradiation cycle (even if in different amount). The phenomenon brings to high level of correlation in the time interval. Lower correlation is observed in the intermediate decay time and it suggests that uncertainty is associated to different nuclides. The analysis could be expanded to consider all fuel assembly batches with intermediate burnup level. Even though it's expected that they will exhibit intermediate behavior compared to the least and most irradiated fuel assemblies, a comprehensive analysis of these intermediate cases can provide valuable insights into the how the various factors affect the decay heat uncertainty.

The uncertainty on decay heat coming from nuclear data is established for a fuel assembly irradiated for one and 18 cycles, that provide the largest decay heat in the short and long cooling time, respectively. The uncertainty is larger, up to 2.5%, for the FA irradiated for one cycle in the short term and then it reduces to almost zero. The uncertainty in the most irradiated fuel assembly is between 1 and 1.5% for the entire transient considered.

Chapter 9

Conclusions

The work presented in this thesis has the purpose to provide updated values for MYRRHA source term in the fuel and LBE, that are of main importance for safety related studies in the framework of the pre-licensing phase of MYRRHA. Source term analysed comprises the nuclide vector (of volatile nuclides and actinides), activity and decay heat.

LBE source term

The activation and spallation products generated by irradiating lead-bismuth eutectic (LBE) starting from the reference composition have been determined. This study focuses on the spallation target assembly, which experiences harsh conditions in terms of particle fluence. The activity of the selected nuclides was of primary importance, and their evolution was tracked for the entire 40-year irradiation period, followed by a decay time of 70 years.

The main contributors to this activity are ^3H , ^{197}Hg , and ^{210}Po , with spallation target assembly (STA) activities of $2.8\text{e}15$, $1.1\text{e}15$, and $8\text{e}14$ Bq, respectively, out of a total activity of $6.3\text{e}16$ Bq. The decay heat is primarily dominated by ^{210}Po for the first year of decay and ^{207}Bi for the entire 70-year observation period. Further division of the irradiation zone reveals the impact of spectral homogenization on the nuclide inventory output. Deviations of up to 50% were observed for the selected nuclides. Most of them are underestimated in the homogeneous approach, except for ^{210}Po , which is exclusively produced by neutron-induced reactions.

Expanding the scope of this work beyond the spallation target assembly to consider the entire core and reactor would allow for a global assessment of the impact of homogenization and an evaluation of the overall production of specific nuclides during irradiation. Additionally, a thorough investigation should be conducted to validate the assumption of employing fixed fluxes in the procedure applied in this work.

Fuel source term

The output of the equilibrium core is analysed to take out the nuclide inventory in every fuel batch. The buildup of volatiles suggests they can be divided in two categories based on the half life:

- short lived nuclides that reach the peak concentration in the first irradiation cycle because of the higher fluxes, since the fuel assembly is irradiated in the core center (position 101);
- relatively long lived nuclides that build up during irradiation and reach the maximum concentration at EoI, before discharge.

Overall, the short lived production is maximized in the sub-critical configuration since the fluxes near to the spallation target are higher. The long lived reach a higher concentration in critical condition since FAs are reshuffled in more positions before being unloaded and the cumulative burnup is higher.

Derived quantities such as activity and decay heat are analysed. It is done assuming to unload all the FAs from the core at the same time and let them decay for a prescribed period. In this way the FA contributing the most to activity/decay heat at each decay time is defined. What is observed is that the assembly irradiated for only one cycle conveys the greatest activity/decay heat at the beginning of decay up to 14/30 days while the most irradiated assemblies are the most contributing after around 2 years of decay. This phenomenon is due to the fact that the short lived nuclides (conveying activity/decay heat in the short period) are overproduced in the fresh FA irradiated in the core center while the long lived fission products and actinides are proportional to the the cumulative burnup.

Fuel assembly models

The fuel assembly models are developed to carry out further analysis because they provide flexibility and lower the computational cost. The limits of the modeling approach are investigated and the comparison with the reference core model was carried out on the nuclide inventory, showing deviations up to 40% for minor actinides. On the contrary, good agreement is found between 2D and 3D fuel assembly models. The influence of axial burnup is limited and it amounts to maximum 4% discrepancy in ^{246}Cm inventory. The deviations are induced by the spectral differences between core and fuel assembly model and this phenomenon is relevant, in particular for fast spectrum reactors, therefore it should be more investigated and understood to improve the quality of the surrogate FA models of MYRRHA and other liquid metal cooled reactors.

Uncertainty analysis

The main goal of the FA model is to perform uncertainty analysis. The sources of uncertainty studied are nuclear data; cross section from JEFF-3.3, ENDF/B-VIII.0

and JENDL-4.0u and neutron fission product yields from JEFF-3.3 are propagated to assess the uncertainties of the outputs, such as nuclide inventory and decay heat. Actinides concentration uncertainty comes from cross sections. It is lower than 2.5% for plutonium isotopes and it tends to linearly increase with burnup. The uncertainty on americium isotopes and ^{242}Cm ranges between 1 and 10% and it is conservatively estimated by JENDL-4.0u while it is strongly underestimated by JEFF-3.3, since uncertainty data for ^{241}Am and ^{242m}Am are not propagated. Largest uncertainty of around 60% is found for ^{246}Cm .

Relevant fission products, divided in volatiles and decay heat contributors are not sensitive to cross sections variations. Their uncertainty is mainly due to NFPY and it ranges from 5 to 10% depending on the actual input uncertainty. ^{134}Cs is sensitive both to cross section and NFPY uncertainty since it is produced by neutron capture in ^{133}Cs that in turn is generated by the decay of fission products. The uncertainty in decay heat varies depending on the decay time, and it also differs when considering a fuel assembly irradiated for 1 cycle compared to one irradiated for 18 cycles. It is dependant on the uncertainty of the main contributors, that changes with the decay time. The correlation between the decay heat of the FA irradiated for 1 and 18 cycles shows, as function of decay time, how the uncertainty apportions to the two systems. It is almost 100% at the beginning of the transient since in both cases decay heat is provided by the same short lived nuclides and between 3 and 70 years when decay heat is dominated by ^{238}Pu and ^{241}Am .

Appendix A

Tritium production in the fuel

The production of ^3H in FA model, that mimics the critical configuration of MYRRHA core comes mainly from ternary fission reactions, a rare phenomenon as witnessed by tritium independent fission yield, that is around to $1.4e - 4$. Nevertheless this brings to a non-negligible production of ^3H building up in the core up to a concentration at discharge of $7.9e - 07 \text{ g/cm}^3$. A deeper investigation on its buildup, comparing critical and sub-critical configuration, Fig. A.1, shows an increase in the production during the first irradiation cycle, when the assembly is in position 101 (near to the spallation target). The sub-critical spectrum comprises a high energy region up to 600 MeV. There are threshold reactions becoming important above the fission energy (20 MeV) contributing to tritium buildup. However the mechanism is much more effective when the fuel assembly is in the central part of the core since high energy tail sharply reduces moving further from the spallation target.

The most relevant reaction happens in the oxygen contained in the MOX and it produces more than half of ^3H in the first cycle. In the following cycles the offset in the buildup among critical and sub-critical stays almost constant demonstrating that the relevance of the high energy tail progressively reduces. At discharge the concentration ratio sub-critical/critical is around 10% with respect to more than 100% when considering only the central position.

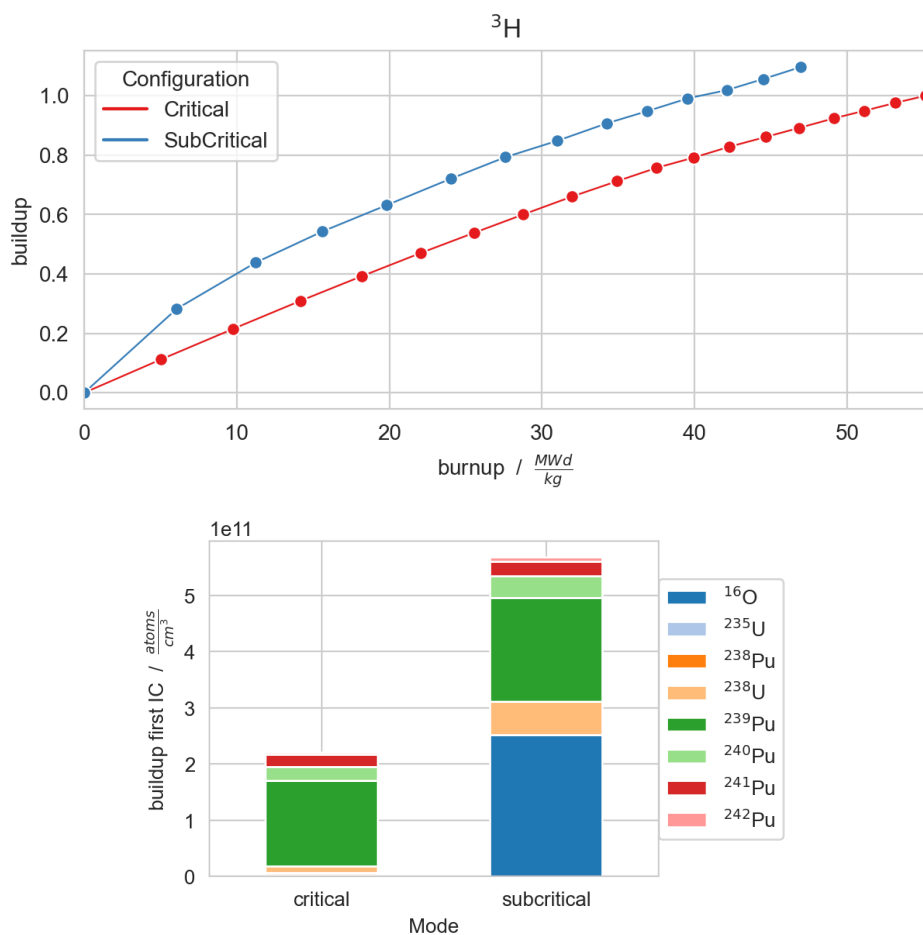


Figure A.1: Tritium production in critical/sub-critical configuration. Top: buildup during irradiation normalized to critical discharge concentration. Bottom: tritium production in the first cycle split by major contributors.

Appendix B

Nuclear data uncertainty

In this section additional information are given on the work carried out to produce perturbed nuclear data files.

B.1 Cross sections

Perturbation of cross section is carried out extracting the multi-group cross sections and covariance matrices from the ENDF-6 file by means of NJOY nuclear data processing code. The perturbations coefficients are generated accordingly and applied to the best estimate evaluations. SANDY code automatizes the procedure so that the user can obtain the required perturbed data in the form of ENDF-6 or ACE file just identifying the nuclide of interest and the additional option to customize the output.

The production of the samples used for the thesis is used as a test to check potential bugs in the pipeline. A complete set of samples is produced for JEFF-3.3 and ENDF/B-VIII.0 containing all the nuclides with available covariance matrix. Some nuclides, despite having uncertainty information, were not processed because of some issues in the pipeline. The nuclides perturbed are listed in Tab. B.1, B.2 for JEFF-3.3 and ENDF/B-VIII.0 respectively. The nuclides having covariance matrix in JEFF-3.3 but not perturbed are:

- ${}^9\text{Be}$, whose covariance matrix file is not processable by NJOY.
- ${}^{241}\text{Am}$, whose covariance data are available in JEFF-3.3 but they are stored in the wrong location that makes difficult the procedure to extract, process the covariance data and to generate the perturbation coefficients.

The nuclides having covariance matrix in ENDF/B-VIII.0 for which the perturbation coefficients were not generated for issues in the procedure are ${}^{40}\text{Ca}$, ${}^{54}\text{Fe}$, ${}^{182}\text{W}$, ${}^{183}\text{W}$, ${}^{184}\text{W}$, ${}^{186}\text{W}$. Most of the effort was devoted to fix the sampling procedure

for JEFF-3.3 library and the lack of these samples in ENDF/B-VIII.0 was not investigated. Moreover the nuclides not perturbed do not affect the outcome of this work and their lack is negligible for the purpose of our analysis.

As regard the perturbed data of JENDL-4.0u there are a lot of covariance matrices missing for fission products. In this case only a set of actinides cross section was perturbed while the effect of FPs was not taken into account. The actinides perturbed are listed in Tab. B.3.

B.2 Neutron fission product yields

The fission yields in evaluated nuclear data libraries are not given with the respective covariance data and the piece of information on their uncertainty resides in their variance. The possibility to generate covariance matrices for NFPY is investigated in [51], introducing physical constraints and applying the GLS method. The objective is to reduce the uncertainty associated to independent fission yields that is usually higher with respect to the variance of the cumulative since they are estimated through semi-empirical mode instead of direct measurements that are not possible for short lived FPs. In this work this methodology is not applied and the perturbed data are generated directly taking the best estimate value and the respective variance of the independent fission yield. From this piece of information the samples are created from a mono-dimensional normal distribution. The only constraint applied is on the normalization of the IFY. The fission yields represent the probability of generating a certain fission product during a fission event. Since in the majority of events two fission products are generated the probabilities sum up to two. The samples generated are normalized on the actual sum of the independent fission yields, that is slightly greater since it takes into account ternary reactions (in JEFF-3.3).

B.3 Convergence analysis

The choice of the number of sample to take to perform statistical sampling is not trivial and impact on how much the samples are representative of the distribution chosen, in this case the normal distribution. A set of the 200 samples of perturbed cross sections for JEFF-3.3, ENDF/B-VIII.0 and JENDL-4.0u and a set 200 samples of perturbed neutron fission product yields given by JEFF-3.3 were produced. A first analysis was carried out on the perturbation coefficients produced by means of statistical sampling to validate the approach and qualitatively assess the normality of the samples. The result of this analysis is shown in Fig. 2.1, Sect. 2.3.2

The convergence of the outputs is verified looking at the discharge concentration

of relevant nuclides slow to converge, such as ^{244}Cm when propagating cross section and ^{134}Cs when considering fission yields.

The convergence of both mean value and standard deviation as function of the

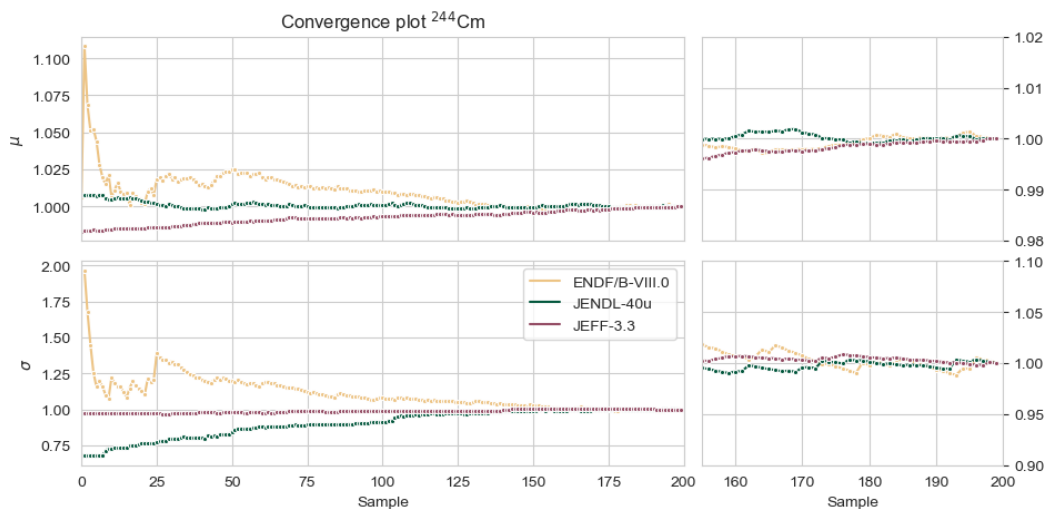


Figure B.1: Convergence of the mean and standard deviation of the discharge concentration of ^{244}Cm with the number of cross section samples.

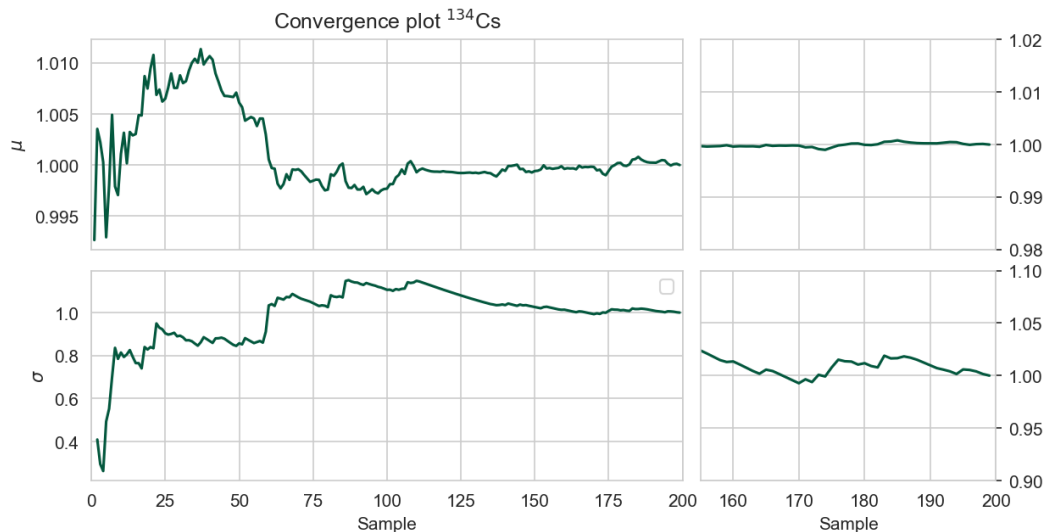


Figure B.2: Convergence of the mean and standard deviation of the discharge concentration of ^{134}Cs with the number of neutron fission product yields samples.

number of samples is verified and it qualitatively proves that 200 samples are

enough to converge to the actual best estimate produced in the non-perturbed simulation and to a certain output standard deviation. To show this trend the results are normalized on the best prediction of the mean and standard deviation, the one obtained with 200 samples.

Table B.1: Nuclides of which cross sections data are perturbed in JEFF-3.3

¹ H	³⁸ Ar	⁵⁵ Fe	⁷¹ As	⁸⁹ Y	¹⁰⁵ Pd	¹²⁷ Xe	¹⁵⁵ Eu	¹⁷⁵ Lu	¹⁹³ Ir	²³² Pa
² H	³⁹ Ar	⁵⁶ Fe	⁷² As	⁹⁰ Y	¹⁰⁶ Pd	¹³¹ Xe	¹⁴⁸ Gd	¹⁷⁶ Lu	¹⁹⁰ Pt	²³² U
⁶ Li	⁴¹ Ar	⁵⁷ Fe	⁷³ As	⁹¹ Y	¹⁰⁷ Pd	¹³² Xe	¹⁴⁹ Gd	¹⁷⁷ Lu	¹⁹¹ Pt	²³³ U
⁷ Li	³⁹ K	⁵⁸ Fe	⁷⁴ As	⁸⁸ Zr	¹⁰⁸ Pd	¹³⁴ Xe	¹⁵⁰ Gd	¹⁷⁴ Hf	¹⁹² Pt	²³⁴ U
¹⁰ B	⁴⁰ K	⁵⁹ Fe	⁷⁵ As	⁸⁹ Zr	¹¹⁰ Pd	^{135m} Xe	¹⁵¹ Gd	¹⁷⁵ Hf	¹⁹³ Pt	²³⁵ U
¹¹ B	⁴¹ K	⁶⁰ Fe	⁷⁶ As	⁹⁰ Zr	^{106m} Ag	¹³³ Cs	¹⁵² Gd	¹⁷⁶ Hf	¹⁹⁴ Pt	²³⁸ U
¹² C	⁴⁰ Ca	⁵⁶ Co	⁷⁷ As	⁹¹ Zr	¹⁰⁷ Ag	¹³⁴ Cs	¹⁵³ Gd	¹⁷⁷ Hf	¹⁹⁵ Pt	²³⁵ Np
¹³ C	⁴¹ Ca	⁵⁷ Co	⁷⁴ Se	⁹² Zr	¹⁰⁸ Ag	¹³⁶ Cs	¹⁵⁴ Gd	¹⁷⁸ Hf	¹⁹⁶ Pt	²³⁶ Np
¹⁵ N	⁴² Ca	⁵⁸ Co	⁷⁵ Se	⁹³ Zr	¹¹⁰ Ag	¹³⁷ Cs	¹⁶¹ Gd	¹⁷⁹ Hf	¹⁹⁸ Pt	²³⁷ Np
¹⁶ O	⁴³ Ca	^{58m} Co	⁷⁶ Se	⁹⁴ Zr	¹¹¹ Ag	¹³¹ Ba	¹⁵⁸ Tb	¹⁸⁰ Hf	¹⁹⁷ Au	²³⁹ Np
¹⁷ O	⁴⁴ Ca	⁵⁹ Co	⁷⁷ Se	⁹⁵ Zr	¹⁰⁹ Cd	¹³³ Ba	¹⁶⁰ Tb	¹⁸¹ Hf	¹⁹⁸ Hg	²³⁶ Pu
¹⁸ O	⁴⁵ Ca	⁶⁰ Co	⁷⁸ Se	⁹⁶ Zr	¹¹⁴ In	¹³⁹ Ba	¹⁵⁶ Dy	¹⁸² Hf	¹⁹⁹ Hg	²³⁸ Pu
¹⁹ F	⁴⁶ Ca	^{62m} Co	⁷⁹ Se	⁹¹ Nb	¹²¹ Sn	¹⁴⁰ Ba	¹⁵⁸ Dy	¹⁷⁹ Ta	²⁰⁰ Hg	²³⁹ Pu
²⁰ Ne	⁴⁷ Ca	⁵⁶ Ni	⁸⁰ Se	⁹² Nb	¹²² Sn	¹³⁷ La	¹⁵⁹ Dy	^{180m} Ta	²⁰¹ Hg	²⁴⁰ Pu
²¹ Ne	⁴⁸ Ca	⁵⁷ Ni	⁸² Se	⁹³ Nb	¹²³ Sn	¹³⁸ La	¹⁶⁰ Dy	¹⁸² Ta	²⁰² Hg	²⁴¹ Pu
²² Ne	⁴⁴ Sc	⁵⁸ Ni	⁷⁷ Br	^{94m} Nb	¹²⁴ Sn	¹³⁹ La	¹⁶⁴ Dy	¹⁸⁰ W	²⁰³ Hg	²⁴⁶ Pu
²² Na	⁴⁵ Sc	⁵⁹ Ni	⁷⁹ Br	⁹³ Mo	¹²⁵ Sn	¹⁴⁰ La	¹⁶⁵ Dy	¹⁸¹ W	²⁰² Tl	²⁴³ Am
²³ Na	⁴⁶ Sc	⁶⁰ Ni	⁸¹ Br	⁹⁵ Mo	¹²⁶ Sn	¹³⁶ Ce	¹⁶³ Ho	¹⁸² W	²⁰³ Tl	²⁴⁴ Am
²⁴ Mg	⁴⁷ Sc	⁶² Ni	⁸² Br	⁹⁹ Mo	¹²² Sb	¹³⁷ Ce	^{166m} Ho	¹⁸³ W	²⁰⁴ Tl	^{244m} Am
²⁵ Mg	⁴⁸ Sc	⁶³ Ni	⁷⁸ Kr	⁹⁶ Tc	¹²⁴ Sb	¹³⁸ Ce	¹⁶⁶ Er	¹⁸⁴ W	²⁰⁵ Tl	²⁴⁰ Cm
²⁶ Mg	⁴⁴ Ti	⁶⁶ Ni	⁸⁰ Kr	⁹⁷ Tc	¹²⁵ Sb	¹³⁹ Ce	¹⁶⁷ Er	¹⁸⁵ W	²⁰⁴ Pb	²⁴¹ Cm
²⁷ Mg	⁴⁶ Ti	⁶³ Cu	⁸² Kr	⁹⁸ Tc	¹²⁶ Sb	¹⁴⁰ Ce	¹⁶⁸ Er	¹⁸⁶ W	²⁰⁵ Pb	²⁴² Cm
²⁶ Al	⁴⁷ Ti	⁶⁴ Cu	⁸³ Kr	⁹⁶ Ru	¹²⁷ Sb	¹⁴¹ Ce	¹⁶⁹ Er	¹⁸⁸ W	²⁰⁶ Pb	²⁴³ Cm
²⁷ Al	⁴⁸ Ti	⁶⁵ Cu	⁸⁴ Kr	⁹⁷ Ru	¹²⁰ Te	¹⁴³ Ce	¹⁷⁰ Er	¹⁸⁵ Re	²⁰⁷ Pb	²⁴⁴ Cm
²⁸ Si	⁴⁹ Ti	⁶⁶ Cu	⁸⁵ Kr	⁹⁸ Ru	¹²¹ Te	¹⁴¹ Pr	¹⁷¹ Er	¹⁸⁶ Re	²⁰⁸ Pb	²⁴⁵ Cm
²⁹ Si	⁵⁰ Ti	⁶⁷ Cu	⁸⁶ Kr	⁹⁹ Ru	¹²² Te	¹⁴² Pr	¹⁷² Er	¹⁸⁷ Re	²⁰⁸ Bi	²⁴⁶ Cm
³⁰ Si	⁴⁸ V	⁶⁴ Zn	⁸⁵ Rb	¹⁰⁰ Ru	¹²³ Te	¹⁴² Nd	¹⁶⁹ Tm	¹⁸⁸ Re	²⁰⁹ Bi	²⁴⁷ Cm
³¹ Si	⁴⁹ V	⁶⁵ Zn	⁸⁶ Rb	¹⁰¹ Ru	¹²⁴ Te	¹⁴³ Nd	¹⁷⁰ Tm	¹⁸⁴ Os	²¹⁰ Bi	²⁴⁸ Cm
³² Si	⁵⁰ V	⁶⁶ Zn	⁸⁷ Rb	¹⁰² Ru	¹²⁵ Te	¹⁴⁵ Nd	¹⁷¹ Tm	¹⁸⁵ Os	²⁰⁸ Po	²⁴⁹ Cm
³¹ P	⁵¹ V	⁶⁷ Zn	⁸⁸ Rb	¹⁰³ Ru	¹²⁶ Te	¹⁴⁶ Nd	¹⁶⁸ Yb	¹⁸⁶ Os	²⁰⁹ Po	²⁵⁰ Cm
³² P	⁵⁰ Cr	⁶⁸ Zn	⁸³ Sr	¹⁰⁴ Ru	^{127m} Te	¹⁵⁰ Nd	¹⁶⁹ Yb	¹⁸⁷ Os	²²⁶ Ra	²⁴⁷ Bk
³³ P	⁵¹ Cr	⁷⁰ Zn	⁸⁴ Sr	¹⁰⁶ Ru	¹²⁸ Te	^{148m} Pm	¹⁷⁰ Yb	¹⁸⁸ Os	²²⁵ Ac	²⁴⁹ Bk
³² S	⁵² Cr	⁶⁷ Ga	⁸⁵ Sr	⁹⁹ Rh	^{129m} Te	¹⁴⁵ Sm	¹⁷¹ Yb	¹⁸⁹ Os	²²⁶ Ac	²⁵⁰ Bk
³³ S	⁵³ Cr	⁶⁹ Ga	⁸⁶ Sr	¹⁰¹ Rh	¹³⁰ Te	¹⁴⁶ Sm	¹⁷² Yb	¹⁹⁰ Os	²²⁷ Ac	²⁴⁹ Cf
³⁴ S	⁵⁴ Cr	⁷¹ Ga	⁸⁷ Sr	¹⁰² Rh	^{131m} Te	¹⁴⁷ Sm	¹⁷³ Yb	¹⁹¹ Os	²²⁷ Th	²⁵⁰ Cf
³⁵ S	⁵² Mn	⁷⁰ Ge	⁸⁸ Sr	¹⁰³ Rh	¹³² Te	¹⁴⁹ Sm	¹⁷⁴ Yb	¹⁹² Os	²²⁸ Th	²⁵³ Cf
³⁶ S	⁵³ Mn	⁷² Ge	⁸⁹ Sr	¹⁰⁴ Rh	¹²⁶ I	¹⁵⁰ Sm	¹⁷⁵ Yb	¹⁹³ Os	²²⁹ Th	²⁵⁴ Cf
³⁶ Cl	⁵⁴ Mn	⁷³ Ge	⁹⁰ Sr	¹⁰⁵ Rh	¹²⁸ I	¹⁵¹ Sm	¹⁷⁶ Yb	¹⁹⁰ Ir	²³² Th	²⁵³ Es
³⁶ Ar	⁵⁵ Mn	⁷⁴ Ge	⁸⁷ Y	¹⁰² Pd	¹²⁴ Xe	¹⁵² Sm	¹⁷³ Lu	¹⁹¹ Ir	²³³ Th	²⁵⁴ Es
³⁷ Ar	⁵⁴ Fe	⁷⁶ Ge	⁸⁸ Y	¹⁰³ Pd	¹²⁶ Xe	^{152m} Eu	¹⁷⁴ Lu	¹⁹² Ir	²³⁴ Th	²⁵⁵ Es

Table B.2: Nuclides of which cross sections data are perturbed in ENDF/B-VIII.0

¹ H	²⁶ Mg	⁵⁵ Mn	⁹⁶ Mo	¹²⁹ I	¹⁵² Sm	¹⁹³ Ir	²¹⁰ Po	²³⁵ U	^{242m} Am	²⁴⁸ Cf
² H	²⁷ Al	⁵⁵ Fe	⁹⁷ Mo	¹³¹ Xe	¹⁵³ Eu	¹⁹⁰ Pt	²²⁵ Ac	²³⁶ U	²⁴³ Am	²⁴⁹ Cf
⁴ He	²⁸ Si	⁵⁶ Fe	⁹⁸ Mo	¹³² Xe	¹⁵⁵ Eu	¹⁹¹ Pt	²²⁶ Ac	²³⁸ U	²⁴⁰ Cm	²⁵⁰ Cf
⁶ Li	²⁹ Si	⁵⁸ Ni	¹⁰⁰ Mo	¹³⁴ Xe	¹⁵² Gd	¹⁹² Pt	²²⁷ Ac	²³⁴ Np	²⁴¹ Cm	²⁵¹ Cf
⁷ Li	³⁰ Si	⁶⁰ Ni	⁹⁸ Tc	¹³³ Cs	¹⁵³ Gd	¹⁹³ Pt	²²⁷ Th	²³⁵ Np	²⁴² Cm	²⁵² Cf
⁷ Be	³⁷ Ar	⁷⁵ Se	⁹⁹ Tc	¹³⁵ Cs	¹⁵⁴ Gd	¹⁹⁴ Pt	²²⁸ Th	²³⁶ Np	²⁴³ Cm	²⁵³ Cf
⁹ Be	⁴¹ Ar	⁸¹ Kr	⁹⁷ Ru	¹³⁹ La	¹⁵⁵ Gd	¹⁹⁵ Pt	²²⁹ Th	²³⁷ Np	²⁴⁴ Cm	²⁵⁴ Cf
¹⁰ B	⁴¹ K	⁸⁹ Y	¹⁰¹ Ru	¹⁴¹ Ce	¹⁵⁶ Gd	¹⁹⁶ Pt	²³⁰ Th	²³⁸ Np	²⁴⁵ Cm	²⁵¹ Es
¹¹ B	⁴⁵ Ca	⁹⁰ Zr	¹⁰² Ru	¹⁴¹ Pr	¹⁵⁷ Gd	¹⁹⁷ Pt	²³¹ Th	²³⁹ Np	²⁴⁶ Cm	²⁵² Es
¹² C	⁴⁷ Ca	⁹¹ Zr	¹⁰³ Ru	¹⁴³ Nd	¹⁵⁸ Gd	¹⁹⁸ Pt	²³² Th	²³⁶ Pu	²⁴⁷ Cm	²⁵³ Es
¹³ C	⁴⁶ Ti	⁹² Zr	¹⁰⁴ Ru	¹⁴⁵ Nd	¹⁶⁰ Gd	¹⁹⁷ Au	²³³ Th	²³⁷ Pu	²⁴⁸ Cm	²⁵⁴ Es
¹⁵ N	⁴⁷ Ti	⁹³ Zr	¹⁰⁶ Ru	¹⁴⁶ Nd	¹⁶⁶ Er	²⁰³ Hg	²³⁴ Th	²³⁸ Pu	²⁴⁹ Cm	^{254m} Es
¹⁶ O	⁴⁸ Ti	⁹⁴ Zr	¹⁰³ Rh	¹⁴⁸ Nd	¹⁶⁷ Er	²⁰⁴ Tl	²²⁹ Pa	²³⁹ Pu	²⁵⁰ Cm	²⁵⁵ Es
¹⁹ F	⁴⁹ Ti	⁹⁵ Zr	¹⁰⁵ Pd	¹⁴³ Pm	¹⁶⁸ Er	²⁰⁴ Pb	²³⁰ Pa	²⁴⁰ Pu	²⁴⁵ Bk	²⁵⁵ Fm
²⁰ Ne	⁵⁰ Ti	⁹⁶ Zr	¹⁰⁶ Pd	¹⁴⁴ Pm	¹⁷⁰ Er	²⁰⁵ Pb	²³² Pa	²⁴¹ Pu	²⁴⁶ Bk	
²¹ Ne	⁵⁰ Cr	⁹⁵ Nb	¹⁰⁷ Pd	¹⁴⁵ Pm	¹⁶⁹ Tm	²⁰⁶ Pb	²³⁰ U	²⁴² Pu	²⁴⁷ Bk	
²² Ne	⁵¹ Cr	⁹² Mo	¹⁰⁸ Pd	¹⁴⁷ Pm	¹⁸⁰ W	²⁰⁷ Pb	²³¹ U	²⁴⁴ Pu	²⁴⁸ Bk	
²³ Na	⁵² Cr	⁹³ Mo	¹⁰⁹ Ag	¹⁴⁵ Sm	¹⁹¹ Os	²⁰⁸ Pb	²³² U	²⁴⁶ Pu	²⁴⁹ Bk	
²⁴ Mg	⁵³ Cr	⁹⁴ Mo	¹⁰⁹ Cd	¹⁴⁹ Sm	¹⁹¹ Ir	²⁰⁹ Bi	²³³ U	²⁴⁰ Am	²⁵⁰ Bk	
²⁵ Mg	⁵⁴ Mn	⁹⁵ Mo	¹²⁷ I	¹⁵¹ Sm	¹⁹² Ir	²⁰⁸ Po	²³⁴ U	²⁴¹ Am	²⁴⁶ Cf	

Table B.3: Actinides of which cross section data are perturbed in JENDL-4.0u

²³⁴ U	²³⁷ U	²³⁸ Np	²³⁹ Pu	²⁴² Pu	²⁴² Am	²⁴⁴ Am	²⁴³ Cm	²⁴⁶ Cm
²³⁵ U	²³⁸ U	²³⁹ Np	²⁴⁰ Pu	²⁴⁴ Pu	^{242m} Am	^{244m} Am	²⁴⁴ Cm	
²³⁶ U	²³⁷ Np	²³⁸ Pu	²⁴¹ Pu	²⁴¹ Am	²⁴³ Am	²⁴² Cm	²⁴⁵ Cm	

Bibliography

- [1] INTERNATIONAL ENERGY AGENCY. *World Energy Outlook 2022*. Tech. rep. URL: www.iea.org/t&c/ (cit. on p. 1).
- [2] Rafael Mariano Grossi. *IAEA ANNUAL REPORT 2021*. Tech. rep. (cit. on p. 1).
- [3] C. F. Smith and L. Cinotti. «Lead-cooled fast reactor». In: *Handbook of Generation IV Nuclear Reactors* (Jan. 2016), pp. 119–155. DOI: 10.1016/B978-0-08-100149-3.00006-9 (cit. on p. 1).
- [4] Hamid Aït Abderrahim, Peter Baeten, Didier De Bruyn, Jan Heyse, Paul Schuurmans, and Jan Wagemans. «MYRRHA, a Multipurpose hYbrid Research Reactor for High-end Applications». In: *Nuclear Physics News* 20.1 (July 2010), pp. 24–28. ISSN: 1061-9127. DOI: 10.1080/10506890903178913 (cit. on p. 2).
- [5] Hamid Aït Abderrahim. «Realization of a new large research infrastructure in Belgium: MYRRHA contribution for closing the nuclear fuel cycle making nuclear energy sustainable». In: *EPJ Web of Conferences* 246 (Dec. 2020), p. 00012. ISSN: 2100-014X. DOI: 10.1051/epjconf/202024600012 (cit. on p. 2).
- [6] A. Stankovskiy and G. Van den Eynde. *Source term calculation for MYRRHA fast spectrum facility*. SCK CEN-I-324, 2012 (cit. on pp. 4, 24).
- [7] A. Stankovskiy and G. Van den Eynde. *Source term calculation for MYRRHA - Design 1.6*. Report SCK CEN/4501955, 2016 (cit. on pp. 4, 24, 38, 39).
- [8] D. Bisogni. *Safety Analysis of Cover Gas Release Scenarios*. SCK CEN/20110496 (cit. on p. 4).
- [9] D. Bisogni. *LBE release into the Primary Containment due to LBECS failure – A Safety Analysis*. SCK CEN/20012887 (cit. on p. 5).
- [10] D. Bisogni. *Ex-vessel Mechanical Failure of a Fuel Assembly – A Safety Analysis*. SCK CEN/20004480, 2017 (cit. on p. 5).
- [11] Stefaan Tavernier. *Interactions of Particles in Matter*. 2009. DOI: 10.1007/978-3-642-00829-0_2 (cit. on p. 6).

- [12] J. Seeman et al. «Design and Principles of Linear Accelerators and Colliders». In: *Particle Physics Reference Library: Volume 3: Accelerators and Colliders*. Vol. 3. Springer International Publishing, Jan. 2020, pp. 295–336. ISBN: 9783030342456. DOI: 10.1007/978-3-030-34245-6_{ }7 (cit. on p. 6).
- [13] Syed Naeem Ahmed. «Properties and sources of radiation». In: *Physics and Engineering of Radiation Detection* (Jan. 2015), pp. 1–64. DOI: 10.1016/B978-0-12-801363-2.00001-2 (cit. on p. 6).
- [14] Phillip M. Rinard. «Neutron Interactions with Matter». In: 1997. URL: <https://api.semanticscholar.org/CorpusID:44224507> (cit. on p. 7).
- [15] George I Bell and Samuel Glasstone. *Nuclear Reactor Theory*. Tech. rep. 1970 (cit. on p. 8).
- [16] John R. Lamarsh. *Introduction to NUCLEAR REACTOR THEORY*. ADDISON-WESLEY PUBLISHING COMPANY (cit. on p. 9).
- [17] Bateman and H. «Solution of a system of differential equations occurring in the theory of radioactive transformations». In: 2011 (cit. on p. 9).
- [18] Maria N. Avramova and Kostadin N. Ivanov. «Verification, validation and uncertainty quantification in multi-physics modeling for nuclear reactor design and safety analysis». In: *Progress in Nuclear Energy* 52 (7 Sept. 2010), pp. 601–614. ISSN: 01491970. DOI: 10.1016/j.pnucene.2010.03.009 (cit. on p. 11).
- [19] D. Rochman, A. J. Koning, and S. C. van der Marck. «Uncertainties for criticality-safety benchmarks and keff distributions». In: *Annals of Nuclear Energy* 36.6 (June 2009), pp. 810–831. ISSN: 0306-4549. DOI: 10.1016/J.ANUCENE.2009.01.018. URL: <https://www.sciencedirect.com/science/article/pii/S0306454909000255#aep-section-id24> (cit. on p. 11).
- [20] D Rochman and C M Sciolla. «Nuclear data uncertainty propagation for a typical PWR fuel assembly with burnup». In: *Nuclear Engineering and Technology* 46.3 (2014), pp. 353–362. ISSN: 2234358X. DOI: 10.5516/NET.01.2014.712 (cit. on p. 11).
- [21] D Rochman, A J Koning, S C Van Der Marck, A Hogenbirk, and C M Sciolla. «Nuclear data uncertainty propagation: Perturbation vs. Monte Carlo». In: *Annals of Nuclear Energy* 38 (5 July 2011), pp. 942–952. ISSN: 03064549. DOI: 10.1016/j.anucene.2011.01.026 (cit. on p. 12).
- [22] Dan G Cacuci, Mihaela Ionescu-Bujor, and Ionel Michael Navon. *Sensitivity and uncertainty analysis, volume II: applications to large-scale systems*. Vol. 2. CRC press, 2005 (cit. on p. 12).

- [23] L Fiorito, G Žerovnik, A Stankovskiy, G Van den Eynde, and P E Labeau. «Nuclear data uncertainty propagation to integral responses using SANDY». In: *Annals of Nuclear Energy* 101 (July 2017), pp. 359–366. ISSN: 0306-4549. DOI: 10.1016/J.ANUCENE.2016.11.026 (cit. on pp. 12, 16).
- [24] Alireza Haghghat. *Monte Carlo Methods for Particle Transport*. CRC Press, Aug. 2020. ISBN: 9780429198397. DOI: 10.1201/9780429198397 (cit. on p. 14).
- [25] C J Werner et al. *MCNP User's Manual Code Version 6.2*. URL: https://mcnp.lanl.gov/pdf_files/la-ur-17-29981.pdf (cit. on p. 14).
- [26] P Baeten, A Stankovskiy, G Van Den Eynde, C Trakas, P.-M Demy, and L Villatte. *ALEPH2-A general purpose Monte Carlo depletion code*. Tech. rep. URL: <https://www.researchgate.net/publication/286740932> (cit. on p. 14).
- [27] Jaakko Leppänen. *Serpent-a Continuous-energy Monte Carlo Reactor Physics Burnup Calculation Code User's Manual*. 2015. URL: <http://ttuki.vtt.fi/serpent>. (cit. on pp. 15, 57).
- [28] A. G. Croff. *A User's Manual for the ORIGEN2 Computer Code*. 1980 (cit. on p. 15).
- [29] M Herman and A Trkov. *ENDF-6 Formats Manual*. 2010. URL: www.nndc.bnl.gov (cit. on p. 16).
- [30] R E Macfarlane, Contributing Authors, D W Muir, R M Boicourt, A C Kahler, J L Conlin, and W Haecck. *The NJOY Nuclear Data Processing System, Version 2016*. 2019 (cit. on p. 16).
- [31] D. G. Cacuci, Mihaela. Ionescu-Bujor, and Ionel Michael. Navon. *Sensitivity and uncertainty analysis*. Chapman Hall/CRC Press, 2003. ISBN: 1584881151 (cit. on p. 16).
- [32] A. J. Koning et al. «Status of the JEFF nuclear data library». In: *Journal of the Korean Physical Society* 59.23 (Aug. 2011), pp. 1057–1062. ISSN: 03744884. DOI: 10.3938/JKPS.59.1057 (cit. on p. 17).
- [33] D. A. Brown et al. «ENDF/B-VIII.0 - The 8th Major Release of the Nuclear Reaction Data Library with CIELO-project Cross Sections, New Standards and Thermal Scattering Data». In: *Nuclear Data Sheets* 148 (Feb. 2018), pp. 1–142. ISSN: 0090-3752. DOI: 10.1016/J.NDS.2018.02.001 (cit. on p. 17).
- [34] Keiichi SHIBATA et al. «JENDL-4.0: A New Library for Nuclear Science and Engineering». In: *Journal of Nuclear Science and Technology* 48.1 (Jan. 2011), pp. 1–30. ISSN: 0022-3131. DOI: 10.1080/18811248.2011.9711675 (cit. on p. 17).

- [35] Organisation for Economic Co-Operation OECD/NEA and Development - Nuclear Energy Agency -. *JEFF 3.1.2 - Joint evaluated nuclear data library for fission and fusion applications - February 2012 (DVD)*. Feb. 2012. URL: https://inis.iaea.org/search/search.aspx?orig_q=RN:43056224 (cit. on p. 17).
- [36] A. J. Koning, D. Rochman, J. Ch Sublet, N. Dzysiuk, M. Fleming, and S. van der Marck. «TENDL: Complete Nuclear Data Library for Innovative Nuclear Science and Technology». In: *Nuclear Data Sheets* 155 (Jan. 2019), pp. 1–55. ISSN: 0090-3752. DOI: 10.1016/J.NDS.2019.01.002 (cit. on p. 18).
- [37] Yu A. Korovin, A. A. Natalenko, A. Yu Stankovskiy, S. G. Mashnik, and A. Yu Konobeyev. «High energy activation data library (HEAD-2009)». In: *Nuclear Instruments and Methods in Physics Research, Section A: Accelerators, Spectrometers, Detectors and Associated Equipment* 624.1 (Dec. 2010), pp. 20–26. ISSN: 01689002. DOI: 10.1016/j.nima.2010.08.110 (cit. on p. 18).
- [38] Luca Fiorito and et al. «Novel neutronics design of the MYRRHA core». In: *International Conference on Fast Reactors and Related Fuel Cycles FR22*. Ed. by International Conference on Fast Reactors and Related Fuel Cycles FR22. 2022 (cit. on p. 19).
- [39] Akio YAMAMOTO and Keiji KANDA. «Comparison between Equilibrium Cycle and Successive Multicycle Optimization Methods for In-Core Fuel Management of Pressurized Water Reactors». In: *Journal of Nuclear Science and Technology* 34.9 (1997), pp. 882–892. DOI: 10.1080/18811248.1997.9733760. eprint: <https://doi.org/10.1080/18811248.1997.9733760>. URL: <https://doi.org/10.1080/18811248.1997.9733760> (cit. on p. 22).
- [40] Alexander Aerts, Borja Gonzalez Prieto, and Jörg Neuhausen. «Behavior of Spallation, Activation and Fission Products in LBE». In: *Comprehensive Nuclear Materials: Second Edition* (Jan. 2020), pp. 735–765. DOI: 10.1016/B978-0-12-803581-8.11612-1 (cit. on p. 24).
- [41] S Keijers, R Fernandez, A Stankovskiy, G Kennedy, and K Van Tichelen. *Design of the MYRRHA Spallation Target Assembly*. Tech. rep. (cit. on p. 26).
- [42] A. Stankovskiy and K. Rosseel. *Formation of spallation products and neutron activation products in a MYRRHA type reactor*. Report SCK CEN-R-5431, 2012 (cit. on p. 38).
- [43] E. Malambu Mbala and A. Stankovskiy. *Revised Core Design for MYRRHA-Rev1 .6*. SCK CEN, 2016 (cit. on p. 38).
- [44] L. Fiorito. *Neutronics core design of MYRRHA - version 1.8*. SCK CEN, 2019 (cit. on p. 38).

-
- [45] Luca Fiorito, Alexey Stankovskiy, Augusto Hernandez-Solis, Gert Van den Eynde, and Gasper Žerovnik. «Nuclear data uncertainty analysis for the Po-210 production in MYRRHA». In: *EPJ Nuclear Sciences Technologies* 4 (Nov. 2018), p. 48. ISSN: 2491-9292. DOI: 10.1051/epjn/2018044 (cit. on p. 40).
- [46] L. Fiorito. *MYRRHA fuel irradiation neutronics analysis*. SCK CEN/43088897|2023 (cit. on p. 42).
- [47] *Secular Equilibrium – Radioactive Equilibrium*. URL: <https://www.nuclear-power.com/nuclear-power/reactor-physics/atomic-nuclear-physics/radioactive-decay/radioactive-equilibrium/secular-equilibrium/> (cit. on p. 49).
- [48] Augusto Hernandez Solis, Alexey Stankovskiy, Luca Fiorito, and Gert Van den Eynde. «Depletion uncertainty analysis to the MYRRHA fuel assembly model». In: *EPJ Web of Conferences* 239 (2020), p. 12001. DOI: 10.1051/epjconf/202023912001 (cit. on p. 56).
- [49] Federico Grimaldi. *Nuclear data uncertainty quantification in fuel depletion calculations*. Master’s thesis. Oct. 2022 (cit. on p. 56).
- [50] Augusto Hernandez-Solis, Klemen Ambrožič, Dušan Čalič, Luca Fiorito, Bor Kos, Marjan Kromar, Peter Schillebeeckx, Alexey Stankovskiy, and Gašper Žerovnik. «BOUNDARY CONDITION MODELING EFFECT ON THE SPENT FUEL CHARACTERIZATION AND FINAL DECAY HEAT PREDICTION FROM A PWR ASSEMBLY». In: *EPJ Web of Conferences* 247 (Feb. 2021), p. 12008. ISSN: 2100-014X. DOI: 10.1051/epjconf/202124712008 (cit. on p. 63).
- [51] L Fiorito, A Stankovskiy, G Van Den Eynde, C J Diez, O Cabellos, and P E Labeau. «Generation of fission yield covariances to correct discrepancies in the nuclear data libraries». In: *Annals of Nuclear Energy* 88 (July 2016), pp. 12–23. ISSN: 18732100. DOI: 10.1016/j.anucene.2015.10.027 (cit. on pp. 77, 89).